

学位論文

**Controlling factors on hydrothermal fluid ascent
in a volcanic edifice revealed by diffuse CO₂ flux
measurements: A case study of Asama volcano, Japan**
(土壤拡散の CO₂ 放出量測定にもとづく
火山体内部での熱水流体上昇を支配する要因の解明
—浅間火山での事例研究—)

平成 28 年 12 月 博士 (理学) 申請

東京大学大学院理学系研究科

地球惑星科学専攻

森田 雅明

**Controlling factors on hydrothermal fluid ascent
in a volcanic edifice revealed by
diffuse CO₂ flux measurements:
A case study of Asama volcano, Japan**

Masaaki Morita

Dissertation submitted for the degree of Doctor of Philosophy in Sciences
Department of Earth and Planetary Science, Graduate School of Science,
The University of Tokyo
December 2016

Dissertation committee:

Professor Shun'ichi Nakai, Chair

Professor Setsuya Nakada

Professor Minoru Takeo

Associate Professor Makoto Uyeshima

Associate Professor Toshiya Mori, Supervisor

© 2016–2017 Masaaki Morita

All rights are reserved by the author, whether the right of divulgation of the work, the right of communication to the public, and the right of reproduction are permitted to exercise for The University of Tokyo, for publishing the electronic version of this dissertation through the repository of The University of Tokyo (<http://repository.dl.itc.u-tokyo.ac.jp>).

Some figures and tables in this dissertation are reused with modifications from a journal published by Springer-Verlag GmbH under the permissions from RightsLink® of Copyright Clearance Center Inc. The journal has already been published: Morita, M., T. Mori, R. Kazahaya, and H. Tsuji (2016), Diffuse carbon dioxide emissions from hidden subsurface structures at Asama volcano, Japan, *Bulletin of Volcanology*, **78**, 17, doi:10.1007/s00445-016-1008-5.

In loving memory of
my father, Masanori Morita (1957–2016)
and
my friend, Kota Nakano (1988–2016)

Abstract

Magmatic volatiles are considered as driving force of eruptions and have impact on the environment when emitted to the atmosphere. Thus, evaluations of volatile emissions from the volcanoes are important to monitor the volcanic activity changes and to assess their impact on the environment. Among the major magmatic volatiles, CO₂ is the first volatile to exsolve from the melt due to its low solubility in the melt, thus measurements of the CO₂ emission are considered important for monitoring volcanic activities, especially to detect the early activation of the volcano. Volcanic CO₂ are emitted into the atmosphere not only as high temperature volcanic plume from active craters but also as invisible emission from the volcano flanks called diffuse CO₂ emission. Recent compiled data of volcanic CO₂ emissions [e.g., *Burton et al.*, 2013, *Rev. Min. Geochem.*] indicated that the diffuse CO₂ emissions are an important source of emissions comparable to the plume CO₂ emissions.

The diffuse CO₂ degassing can be treated as consequences of the hydrothermal fluid ascent in the volcano flanks. The area of the anomalous diffuse CO₂ emission is called diffuse degassing structures (DDS). Numerous previous works found the relation between the DDS and regional tectonic or volcano-tectonic structures. Additionally, a recent study on the distribution of fumarolic areas by *Schöpa et al.* [2011, *J. Volcanol. Geotherm. Res.*] clarified that the topography and lithology controls as well as the structure control are effective controlling factors of the hydrothermal fluid ascent. However, little is known about the topography control on the DDS distribution.

The objectives of this study are to reveal the controlling factors on the diffuse CO₂ degassing, especially the influence of the topography control, and to examine the possibilities of other controlling factors on the diffuse CO₂ degassing. For the objectives of this study, summit area of Asama volcano, Japan, was selected as the study area, which was mainly set in Maekake crater (the outer crater), the summit area of Asama volcano.

The surveys of diffuse CO₂ flux at the summit area of Asama volcano were conducted six times during 2012–2016. Four surveys with total of 211 measurements were conducted in the inactive period. Two surveys with total of 80 measurements were conducted in October 2015 and August 2016 during the active period after the minor eruptions in June 2015. In the 2016 survey, soil gas samples were also collected and analyzed for chemical and isotopic compositions at selected measurement sites.

Statistical analysis based on the graphical statistical approach (GSA) was applied to the observed soil CO₂ flux values of the summit area in the inactive period, and spatial distributions of

the soil CO₂ flux values were constructed using sequential Gaussian simulation (sGs). The soil CO₂ flux distribution of the inactive period showed an E–W heterogeneous distribution at the summit area and a N–S elongated elliptical-ring shape DDS was found only in the eastern side of the study area. In the northern, southern, and western parts of the study area, the soil CO₂ flux values were basically negligible except for a small area on western Maekake crater wall.

The ring shape of the DDS is likely explained both 1) by the volcano-tectonic structures corresponding to hidden fractures of the two collapsed craters, which formed present Maekake crater, and 2) by the topography control as revealed by spatial comparisons between the DDS distribution and the topographic position index (TPI) map, which was introduced to extract the local crests of the summit area.

The E–W heterogeneity of the CO₂ flux distribution and the $\delta^{13}\text{C}$ values of soil CO₂ indicated that other controlling factors except for the structure, lithology, and topography controls should also be considered for the summit area of Asama volcano. A comparison between the electrical resistivity structure of Asama volcano and the results of this study showed that the low-resistive body at shallower depth under the eastern side of Maekake volcano corresponds to hydrothermal fluids as the source of the diffuse CO₂. The comparison also suggested that the negligible or very small diffuse CO₂ emission in the western part may be explained by the very weak connection of the hydrothermal source to the ascending pathways of the fluids due to larger depth of the hydrothermal source and/or sealing clay-rich mineral layers, or by the low amount of the hydrothermal fluids in the western side. The presence of both the hydrothermal source and the connection from the hydrothermal source to the ascending pathways are probably an important factor to form the observed E–W heterogeneous diffuse CO₂ distribution at the summit area of Asama volcano, which may also be important for other volcanoes.

Based on previous studies and this study, a schematic model of the degassing system of Asama volcano in inactive periods was suggested. This study revealed that a total emission rate of diffuse CO₂ from the summit area of Asama volcano was 12.6 t day⁻¹ in the inactive period, and that such significant amount (about 12 % of total CO₂ emission) is emitted as diffuse CO₂ from the eastern part of the summit area. The diffuse CO₂ emission observed only in the eastern side of the summit area is important for understanding the structural framework of Asama volcano. Thus, further repetitive surveys of diffuse CO₂ emissions in this area would be important to understand the development of the hydrothermal system of the volcano. Moreover, the diffuse CO₂ flux values of the active period in the eastern part of Maekake crater rim showed significant increase from those of the inactive period. Hence, the eastern Maekake crater rim may be an effective site for monitoring the volcanic activity by the continuous diffuse CO₂ flux measurement in the future.

Acknowledgements

First of all, I would like to show my deepest gratitude to my supervisor, Dr. Toshiya Mori, for giving me the opportunity to work in volcanology and a lot of advices to my study. His shrewd advices and ingenious ideas always improved my study to the better place and his attitude to the science always encouraged me. I am deeply grateful to Drs. Minoru Takeo, Setsuya Nakada, Takao Ohminato, Mie Ichihara, Yosuke Aoki, Jun Oikawa, Fukashi Maeno, Yujiro Suzuki, Atsushi Watanabe, Hiroshi Shinohara, Ryunosuke Kazahaya, Akiko Tanaka, Hiroshi A. Takahashi, Hirochika Sumino, Akihiko Terada, Wataru Kanda, Akihiko Yokoo, Keigo Yamamoto, Takeshi Hashimoto, Shun'ichi Nakai, Yuji Sano, Urumu Tsunogai, Makoto Uyeshima, Koki Aizawa, Takao Koyama, Yasuo Ogawa, Masaki Takahashi, Maya Yasui, Kenji Nogami, Patrick Allard, Eleazar Padrón, Pedro A. Hernández, Gladys Melián, Nemesio M. Pérez, Taku Urabe, and Kenji Notsu and Messrs. Hiroshi Tsuji, Yoshiya Usui, and Takato Ono for valuable discussions and supports of the observations and the analyses. I would like to express my gratitude to Drs. Fumiaki Tsunomori, Keisuke Nagao, Hiroyuki Kagi, Kazuki Komatsu, Takehiko Yagi, Katsutoshi Aoki, Riko Iizuka, and the other researchers and students of Geochemical Research Center (GCRC) for giving me a lot of advices in seminars. I would like to offer my special thanks to Mss. Yukiko Torizuka, Tomoko Tsuchiya, Yuri Shitara, Kaoru Yoshida, Minako Kamakura, and Sumiko Ohsato, the staffs of GCRC, for supporting the study. Special thanks to the people who met at conferences and workshops: Drs. Kenta Ueki, Kenta Yoshida, Rina Noguchi, and Koji Kiyosugi and other researchers and students. Last but certainly not least, I would like to show my great appreciation to my family and friends, especially to my late father Masanori, who encouraged me a lot of time during my Ph. D. course and perhaps wanted to read this dissertation.

This study was partly supported by the Ministry of Education, Culture, Sports, Science and Technology (MEXT) of Japan, under its Observation and Research Program for Prediction of Earthquakes and Volcanic Eruptions and its Earthquake and Volcano Hazards Observation and Research Program. Soil CO₂ flux meters were provided by Shizuoka University and Kyushu University. Map data of Asama volcano were provided by Geospatial Information Authority of Japan. Map data of Vesuvio and Vulcano volcanoes were respectively provided by Dr. Arianna Pesci (Istituto Nazionale di Geofisica e Vulcanologia) and Dr. Paolo Baldi (Università di Bologna). Figures in this thesis were prepared with QGIS 2.18 [*QGIS Development Team*, 2016], SAGA GIS 2.2.3 [*Conrad et al.*, 2015], GMT 5.3.0 [*Wessel et al.*, 2013], Microsoft Excel® 2016, and Adobe Photoshop® CC 2017.

Table of contents

Chapter 1 Introduction	1
1.1 Volcanic gas emissions and CO ₂ in the volcanic gas	1
1.2 Diffuse soil emanations of CO ₂ from volcano flanks	2
1.3 Diffuse degassing structures and controlling factors of hydrothermal fluid ascent	8
1.3.1 <i>Controlling factors on the formation of diffuse degassing structures</i>	8
1.3.2 <i>Controlling factors on hydrothermal fluid ascent revealed from distributions of fumaroles and heat anomalies</i>	10
1.4 Objectives of this study	12
Chapter 2 Geological and volcanological background of Asama volcano	15
2.1 Geology of Asama volcano	15
2.2 Geophysical and geochemical observations of Asama volcano	17
2.3 Magma plumbing system and degassing system of Asama volcano	19
2.4 Recent volcanic activities of Asama volcano	21
2.4.1 <i>The 2004 eruption</i>	22
2.4.2 <i>The 2008–2009 eruption</i>	22
2.4.3 <i>Volcanic activities and characteristics of Asama volcano as the field of this study</i>	23
Chapter 3 Observations and methods	27
3.1 An outline of the observations	27
3.2 Soil CO ₂ flux and soil temperature measurements	30
3.3 Statistical treatment of soil CO ₂ flux and soil temperature	31
3.4 Soil gas sampling and laboratory analysis	35
Chapter 4 Results	37
4.1 Soil CO ₂ flux and soil temperature at the summit area in 2012–2014	37
4.2 Soil CO ₂ flux and soil temperature at the summit area in 2015 and 2016	45
4.3 Soil CO ₂ flux at the flanks of Maekake volcano	49
4.4 Soil CO ₂ flux and soil temperature at Jigokudani fumarolic field	49
4.5 Chemical and isotopic compositions of soil gas and bubbling gas	51
Chapter 5 Discussion	57
5.1 Controlling factors and the source of diffuse CO ₂ degassing	57
5.1.1 <i>Structure control by regional and volcano-tectonic structures</i>	57
5.1.2 <i>Lithology control</i>	58

5.1.3	<i>Topography control</i>	59
5.1.4	<i>Other controlling factors and the source of diffuse CO₂ degassing</i>	64
5.2	Degassing system of Asama volcano	66
Chapter 6 Conclusions		71
References		75
Appendix A Observed data of soil CO₂ flux and soil temperature		101
A.1	Soil CO ₂ flux and soil temperature in 2012–2014 at the summit area and the eastern flank of Asama volcano	101
A.2	Soil CO ₂ flux and soil temperature in 2015 and 2016 at the summit area and the western flank of Asama volcano	105
A.3	Soil CO ₂ flux and soil temperature in 2016 at jigokudani fumarolic field	106
Appendix B Compilation of $\delta^{13}\text{C}(\text{CO}_2)$ data for volcanoes and geothermal fields		109

Chapter 1

Introduction

1.1 Volcanic gas emissions and CO₂ in the volcanic gas

Volcanic gas is a high temperature gas of magmatic volatiles exsolved from silicate melt and emitted to the atmosphere. It mainly consists of water (H₂O), carbon-bearing species such as carbon dioxide, carbon monoxide, and methane (CO₂, CO, CH₄), sulfur-bearing species such as sulfur dioxide, hydrogen sulfide, elemental sulfur, and carbonyl sulfide (SO₂, H₂S, S₂, COS), halogens such as hydrogen chloride and hydrogen fluoride (HCl, HF), and other components such as hydrogen, nitrogen, ammonia, helium, argon (H₂, N₂, NH₃, He, Ar) [Giggenbach, 1996; Fischer, 2008; Oppenheimer et al., 2011]. The most abundant species is H₂O that typically accounts for more than 90 mol % in the volcanic gas from arc setting volcanoes. The second and the third abundant species for high temperature volcanic gases are respectively CO₂ and SO₂ those together account for 5–10 mol %. Volcanic gas is emitted during various volcanic activities from explosive eruptions to non-eruptive gas emissions known as persistent or passive degassing. These volcanic gas emissions are from main active vents or high temperature fumaroles (>500 °C). They form volcanic plumes mixing with atmospheric air, ash, and aerosols.

Magmatic volatiles control the physical properties of magmas and are the driving force of the eruptions. The exsolution and segregation of magmatic volatiles influence on magma overpressure, viscosity, and density, hence they control the storage and transport of magma and the style, magnitude, and duration of eruptions [Sparks, 2003; Oppenheimer et al., 2014]. To interpret the behavior of magma under the volcano and, consequently, to monitor and predict the volcanic activity, measurements of volcanic gas composition and flux are important and have been conducted by many researchers [Aiuppa et al., 2007; Oppenheimer et al., 2014].

Magmatic volatiles are also important with respect to their impact on the terrestrial environment. Volcanic volatile emissions from the Earth's interior to the atmosphere can affect the terrestrial environment and climate both in space and time at wide scales [Oppenheimer et al., 2014]. They play an important role in geochemical cycles of volatiles among the lithosphere, hydrosphere, atmosphere, and biosphere as huge natural contributors on volatile emissions from the lithosphere [Wallace, 2005; Oppenheimer et al., 2014]. The volatile emissions from volcanoes have been estimated using various methods [Sano and Williams, 1996; Marty and Tolstikhin, 1998;

Wallace, 2005; Burton *et al.*, 2013; Shinohara *et al.*, 2013; Kagoshima *et al.*, 2015]. For the estimation of global volatile emissions from subaerial volcanoes, observed data from individual volcanoes are compiled and extrapolated to non-measured volcanoes [e.g., Burton *et al.*, 2013]. Thus, the estimated global emissions from volcanoes have potential uncertainties and the more accurate estimation is only achievable by compiling newly measured emissions from the non-measured volcanoes.

Among the major magmatic volatiles in ascending magma, CO₂ is the first volatile exsolved from the melt [e.g., Allard, 2010] because of its low solubility in magma [Stolper and Holloway, 1988]. When magmas at depth ascends to the surface, emission rates and compositions of volcanic CO₂ are expected to change [Aiuppa *et al.*, 2007, 2010]. For example, at Etna volcano (Italy), pre-eruptive increases of the CO₂/SO₂ ratio have been reported and are related to the refilling of shallow conduits with CO₂-rich deep magmas [Aiuppa *et al.*, 2007]. At Stromboli volcano (Italy), enormous emissions of plume CO₂ sourced from a deeply stored magma have been reported before intensive eruptions [Aiuppa *et al.*, 2010]. From this perspective, volcanic CO₂ can be a good indicator for intensive volcanic activities.

Volcanic CO₂ are emitted into the atmosphere not only as high temperature volcanic gases from active craters but also as low temperature gases from fumaroles, hot springs, or mofette, or as invisible diffuse soil emissions from the volcano flanks (**Fig. 1.1**). Among these low temperature gases partly or completely affected by a hydrothermal system, the main components except for water are CO₂, H₂S, CH₄, and NH₃ [Giggenbach, 1980, 1987; Chiodini and Marini, 1998]. Especially, CO₂ is the most abundant species in diffuse degassing from volcanic areas.

Among the low temperature gases above, measurements of the diffuse CO₂ degassing are important for monitoring volcanic activities because anomalous changes of the diffuse CO₂ emission preceding the eruptive activities have been reported [e.g., Hernández *et al.*, 2001a; Carapezza *et al.*, 2004]. Furthermore, recent studies revealed that both the plume and diffuse CO₂ emissions are huge contributors as volcanic CO₂ emissions and that the diffuse CO₂ emission is comparable to the plume CO₂ emission [e.g., Burton *et al.*, 2013]. For this point, the measurements of the diffuse CO₂ emissions are of the same importance as the measurements of the plume CO₂ emissions for understanding degassing from volcanoes.

1.2 Diffuse soil emanations of CO₂ from volcano flanks

In volcanic areas, visible output of steam or gas emitting from the ground are often observed. These volatile emissions from vents are called fumaroles that usually accompany fumes or plumes and are usually considered as emitting center of volatiles from the volcanoes. The fuma-

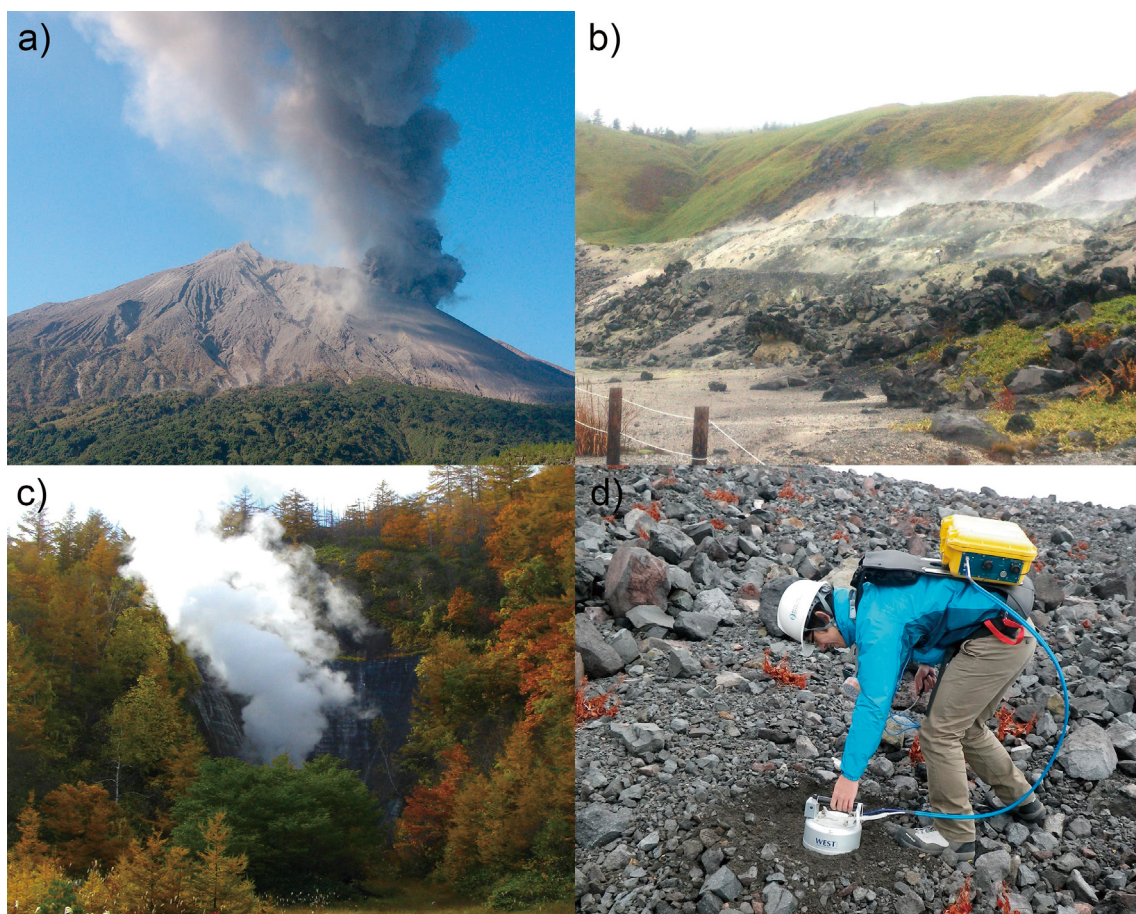


Fig. 1.1 Various types of volcanic gas emissions. **a** Volcanic plume (a mixture of gas, ash, and pyroclastic materials) by a vulcanian eruption at Sakurajima volcano (Japan). **b** Low temperature fumaroles at Kusatsu-Shirane volcano (Japan). **c** Hot spring gases from a former sulfur mine at Kusatsu-Shirane volcano. **d** Diffuse CO_2 degassing at the summit area of Asama volcano (Japan).

roles are often thermally active and are also significant sources of heat from the ground. In contrast, there is a different type of a volcanic volatile emission called diffuse degassing. The diffuse degassing is an invisible volatile emission from a ground surface percolating through the soils of volcanic flanks. Unlike fumaroles, this emission is not discharged from a point source and sometimes lacks thermal anomalies like the case of diffuse gas emission from flanks of Etna volcano [Giammanco *et al.*, 2016]. The diffuse CO_2 is thought to be supplied from a hydrothermal system in the volcanic edifice where magmatic CO_2 from the magma plumbing system contacts hydrothermal and meteoric water [Williams-Jones *et al.*, 2000; Padrón *et al.*, 2012b]. If the hydrothermal fluid does not lose much heat during the ascent, it can form the fumarolic areas at the surface. The diffuse CO_2 is derived from a gas phase of condensed hydrothermal fluid [Fronzini *et al.*, 2004] and emitted from the ground surface without forming fumarolic vents. As well as the hydrothermal fluid source, it is sometimes fed by a shallow biogenic source [e.g., Chiodini *et al.*, 2008]. The diffuse CO_2 ascends to the surface by advection and diffusion mechanisms [Natale *et al.*, 2000; Hernández

et al., 2001a; *Camarda et al.*, 2007]

The diffuse degassing first drew attention by the results of airborne gas profiling of CO₂ at Etna volcano, which implied huge amount of CO₂ emission from flanks of the volcano [*Allard et al.*, 1991]. After this detection of an enormous CO₂ emission from Etna, numerous studies on diffuse CO₂ degassing have been made on the flanks of active and inactive volcanoes all over the world. Reported emissions of the diffuse CO₂ are compiled by a recent review by *Burton et al.* [2013]. Even after this compilation, new diffuse CO₂ flux data have been reported by many researchers. The reported diffuse CO₂ flux data for active and inactive volcanoes, geothermal areas, and tectonic active regions are summarized in **Table 1.1**. Plume CO₂ emissions are also listed to be compared to the diffuse CO₂ emissions and the diffuse/total ratios in CO₂ emissions defined by diffuse/(diffuse + plume) are calculated for the volcanoes with the plume emission (**Table 1.1**). At volcanoes without plume or significant fumarolic emissions, of course, the diffuse degassing is considered to be the main contributor of CO₂ emissions to the atmosphere and as high as about 45,000 t day⁻¹ at Yellowstone volcano (USA) is observed [*Werner and Brantley*, 2003]. The diffuse CO₂ emissions from volcanoes with plume emissions vary from non-detectable to more than a few tens of thousand tons per day (**Table 1.1**). At one of the highest plume degassing volcano, Popocatepetl (México), the diffuse CO₂ emission has not been detected on the volcano flanks [*Varley and Armienta*, 2001]. However, some plume degassing volcanoes such as Etna and Merapi show relatively high diffuse CO₂ emissions compared to the total emissions with ratios over 30 % [*Toutain et al.*, 2009; *Hernández et al.*, 2015]. These data indicate that, even at significant plume degassing volcanoes, diffuse CO₂ degassing cannot be neglected to understand the degassing systems of the volcanoes. As illustrated in **Table 1.1**, a number of investigated volcanoes having both the plume and diffuse emissions is still small. Especially, data of the plume or fumarolic CO₂ emissions from volcanoes with low temperature fumarolic activities are still rare [*Allard et al.*, 2014]. Conversely, data of the diffuse CO₂ emission from many plume degassing volcanoes have not been investigated well, yet. Therefore, it is required to measure both diffuse and plume emissions from plume degassing volcanoes.

Diffuse CO₂ emission is an important tool for monitoring the volcanic activities. *Hernández et al.* [2001a] observed an increase of diffuse CO₂ emission rate and spatially enlarged diffuse CO₂ emission area before the 2000 eruption of Usu volcano (Japan). At Stromboli volcano, *Carapezza et al.* [2004] reported that continuous records of soil CO₂ flux showed anomalously high CO₂ flux a week before the onset of the December 2002 eruption at Stromboli volcano (Italy). *Pérez et al.* [2012] found a precursory increase of diffuse CO₂ flux from continuous measurements before the 2011–2012 submarine eruption at El Hierro (Canary Islands). In the same event, total CO₂ emis-

Table 1.1 Plume/fumarole and diffuse CO₂ emissions from active and inactive volcanoes, geothermal areas, and tectonic active regions following Viveiros et al. [2010], Burton et al. [2013], Hernández et al. [2015], and Morita et al. [2016]

Volcano or area	Country or area	Tectonic setting ^a	Plume or fumarole emission [t day ⁻¹]	Diffuse emission [t day ⁻¹]	Diffuse/total ratio [%]	Reference
<i>Active volcanoes</i>						
Popocatepetl	México	S	32,000	n.d.	0	Goff et al., 2001; Varley and Armienta, 2001
Aso	Japan	S	600	0.12	0.02	Saito et al., 2007
Longonot	Kenya	R	—	<0.3	—	Robertson et al., 2016
Kusatsu-Shirane	Japan	S	—	1.4	—	Saito et al., 2004
Raykjanes	Iceland	R	0.23	13.5	98	Fridriksson et al., 2006
Showa Shinzan	Japan	S	—	14.8 ^b	—	Hernández et al., 2006
Satsuma-Iwojima	Japan	S	100	20	17	Shimoike et al., 2002
Masaya	Nicaragua	S	930	20	2.1	Lewicki et al., 2003; Aiuppa et al., 2014
Liu-Huang-Ku, Tatun	Taiwan	S	—	21.1 ^b	—	Lan et al., 2007
Santorini	Greece	S	—	28 ^b	—	Parks et al., 2013
Ukinrek Marrs	USA	S	187	33 ^b	15	Doukas and McGee, 2007; Evans et al., 2009
El Chichón (soil only)	México	S	—	35	—	Mazot et al., 2011
Erebus	Antarctica	I	1,930 ^b	40	2.0	Wardell et al., 2003, 2004
Hekla	Iceland	R	—	44	—	Ilyinskaya et al., 2015
Stromboli	Italy	S	370	46	11	Inguaggiato et al., 2013
Brava	Cape Verde	I	—	50	—	Dionis et al., 2015a
Aluto	Ethiopia	R	—	57	—	Hutchison et al., 2015
Nisyros	Greece	S	—	70 ^b	—	Brombach et al., 2001; Cardellini et al., 2003b; Caliro et al., 2005; Chiodini et al., 2005
Tatun	Taiwan	S	—	82	—	Wen et al., 2016
Vulcano Island	Italy	S	360	91	20	Inguaggiato et al., 2012
White Island	New Zealand	S	890 ^b	124	12	Werner et al., 2008; Bloomberg et al., 2014
Ol Doimyo Lengai	Tanzania	R	6,600 ^b	ca. 100	ca. 1	Koepenick et al., 1996
Vesuvio	Italy	S	—	137 ^b	—	Fronzoni et al., 2004; Granieri et al., 2013
Miyakejima (before 2000)	Japan	S	—	122 ^b	—	Hernández et al., 2001b
Usu	Japan	S	—	166 ^b	—	Hernández et al., 2001a
Copahue-Caviahue	Argentina, Chile	S	—	165	—	Chiodini et al., 2015
Merapi	Indonesia	S	240	215 ^b	47	Toutain et al., 2009
Pululahua	Ecuador	S	—	270	—	Padrón et al., 2008

Volcano or area	Country or area	Tectonic setting ^a	Plume or fumarole emission [t day ⁻¹]	Diffuse emission [t day ⁻¹]	Diffuse/total ratio [%]	Reference
Teide	Canary Islands	I	—	380	—	Hernández et al., 1998
Iwojima	Japan	S	—	450	—	Notsu et al., 2005
Santa Ana–Izalco–Coatepeque	El Salvador	S	—	ca. 600	—	Salazar et al., 2004
Sierra Negra	Galápagos	R	394	605	61	Padrón et al., 2012a
Fogo	Cape Verde	I	—	828	—	Dionis et al., 2015a
El Hierro	Canary Islands	I	—	863 ^b	—	Melián et al., 2014
Pantelleria Island	Italy	R	77	880	92	Favara et al., 2001
Furnas	Azores	R	—	968 ^b	—	Cruz et al., 1999; Viveiros et al., 2010
La Palma	Canary Islands	I	—	1,147 ^b	—	Padrón et al., 2015
Ischia	Italy	S	3	1,282	100	Pecoraino et al., 2005
Solfatara of Pozzuoli	Italy	S	—	1,480	—	Chiodini et al., 2005
Rabaul	Papua New Guinea	S	—	ca. 2,400	—	Pérez et al., 1998
Cerro Negro	Nicaragua	S	—	2,800	—	Salazar et al., 2001
Etna	Italy	S	35,000	20,000	36	Hernández et al., 2015
<i>Inactive volcanoes, geothermal areas, and tectonic active regions</i>						
Basin-and-Range Province	USA	R	—	0.27	—	Jolie et al., 2015
Hartoušov	Czech	R	—	1.6	—	Kämpf et al., 2013
Nyos Valley	Cameroon	R	—	2.13	—	Issa et al., 2014
Palma Campana	Italy	S	—	2.7	—	Cardellini et al., 2003a
Selvina	Italy	S	—	8	—	Rogjie et al., 2000
Long Valley caldera	USA	R	—	8.7	—	Bergfeld et al., 2006
Pienza	Italy	S	—	11	—	Rogjie et al., 2000
Umbertide	Italy	S	—	16	—	Rogjie et al., 2000
Cava dei Selci	Italy	S	—	20	—	Rogjie et al., 2000
Acocalco caldera	México	S	—	25	—	Peiffer et al., 2014
Manenguba caldera	Cameroon	R	—	26.9	—	Issa et al., 2014
Rapalano Cecilia	Italy	S	—	48	—	Rogjie et al., 2000
Solforata	Italy	S	—	50	—	Rogjie et al., 2000
Linosa Island	Italy	R	—	55	—	Cellura et al., 2014
Auckland volcanic field	New Zealand	S	—	61.8	—	Mazot et al., 2013
Albani Hills	Italy	S	—	74	—	Chiodini and Frondini, 2001

Volcano or area	Country or area	Tectonic setting ^a	Plume or fumarole emission [t day ⁻¹]	Diffuse emission [t day ⁻¹]	Diffuse/total ratio [%]	Reference
Hakkoda	Japan	S	—	74	—	Hernández Perez et al., 2003
Rapalano Mofete Diambra	Italy	S	—	96	—	Rogie et al., 2000
Torre Alfina	Italy	S	—	101.6	—	Carapezza et al., 2015
Yangbajian	China	R	—	138	—	Chiodini et al., 1998
Manziana	Italy	S	—	>200	—	Chiodini et al., 1999
São Vicente	Cape Verde	I	—	226	—	Dionis et al., 2015a
Mammoth Mountain	USA	R	—	228 ^b	—	Werner et al., 2014
Poggio dell'Olivo	Italy	S	—	233.5	—	Cardellini et al., 2003b
Latera	Italy	S	—	350	—	Chiodini et al., 2007a
Las Cañadas caldera	Canary Islands	I	—	437	—	Marrero et al., 2008
Rotokawa	New Zealand	S	—	441	—	Bloomberg et al., 2014
Hengill	Iceland	R	—	453	—	Hernández et al., 2012
Mefite d'Ansanto	Italy	S	—	ca. 2,000	—	Chiodini et al., 2010
Magadi	Kenya	R	—	4,327	—	Lee et al., 2016
Natron	Tanzania, Kenya	R	—	6,746	—	Lee et al., 2016
Yellowstone	USA	R	—	ca. 45,000	—	Werner and Brantley, 2003

^aI: Intraplate; R: Rift; S: Subduction

^bAn average value of multiple measurements or references

n.d. not detected, — not measured or absence of measurable plume

sion rate from the island also increased with relation to the volcanic activity increase [Melián *et al.*, 2014]. These observations showed precursory diffuse CO₂ emission change before the eruptive activities or activations of volcanoes. Thus, the repetitive and continuous monitoring of diffuse CO₂ emission are considered important for monitoring volcanic activities, especially to detect the early activation of the volcano.

1.3 Diffuse degassing structures and controlling factors of hydrothermal fluid ascent

As mentioned in the previous section, the diffuse CO₂ is thought to be derived from a gas phase of condensed hydrothermal fluids [Williams-Jones *et al.*, 2000; Frondini *et al.*, 2004] and emitted from the ground surface without forming fumarolic vents. If the ascending hydrothermal fluids do not lose the heat, they can form the fumarolic areas at the ground surface. Therefore, the diffuse degassing and the fumaroles are often considered to have the same source of the hydrothermal fluids at depth [Giammanco *et al.*, 2016]. From this point of view, both the diffuse CO₂ degassing and the fumarolic activity can be treated as consequences of the hydrothermal fluid ascent in the volcano flanks.

The diffuse CO₂ flux at volcanoes shows large spatial variations because the diffuse CO₂ degassing commonly occurs in limited area rather than homogeneously across the entire volcanic system [Chiodini *et al.*, 1998, 2001, 2008]. This limited area with the anomalous diffuse CO₂ emission is called as diffuse degassing structures (DDS) [Chiodini *et al.*, 2001] and is usually located within or near fumarolic fields of the volcano [Chiodini *et al.*, 2005].

The fumarolic activity also occurs at limited areas of the volcano and the thermal anomalies related to the fumaroles have been investigated by soil temperature surveys and remote sensing with thermal infrared (TIR) cameras [e.g., Spampinato *et al.*, 2011]. The location of fumarolic activity is important to understand the volcano structure and the fumarolic activity itself. It is also important for exploitations of geothermal resources and ore deposits. Thus, the controlling factors of hydrothermal fluid ascent are also discussed in the studies of the hydrothermal systems [Schöpa *et al.*, 2011].

1.3.1 Controlling factors on the formation of diffuse degassing structures

Numerous previous works found the relation between the DDS and regional tectonic or volcano-tectonic structures. At the Fossa cone of Vulcano Island (Italy), the DDS was found around fumarolic vents on the inner slope of the cone and along a NW–SE line at the northeast area of the crater rim, which reflects the main directions of the active faults [Chiodini *et al.*, 1996]. At 1 km west of Fossa crater, a narrow NNE–SSW line of the DDS related to the active tectonic trend was

also reported [Chiodini *et al.*, 1998]. At Solfatara of Pozzuoli, Campi Flegrei (Italy), the DDS covered a larger area inside and outside the crater showing a spatial correlation with fractures caused by local stress field [Chiodini *et al.*, 2001, 2008]. At Stromboli volcano (Italy), the main DDS was associated with the main volcano-tectonic axis of the island and narrow areas parallel to the traces of sector collapse [Carapezza *et al.*, 2009]. At Merapi volcano (Indonesia), the soil CO₂ concentration anomalies were related to major volcano-tectonic structures such as fractures around the summit and buried crater rims of historical eruptions on the flank [Toutain *et al.*, 2009]. At Nisyros volcano (Greece), the diffuse CO₂ flux anomalies were found along the main faults of the region and inside Stefanos crater [Caliro *et al.*, 2005]. In the studies above, faults, fractures, and ring-faults corresponding to the crater rims have been considered as possible pathways of ascending diffuse CO₂ because of their high-permeability [e.g., Werner and Cardellini, 2006].

To reveal the fluid ascent along the volcano-tectonic structures and to detect hidden structures under the volcano, some diffuse CO₂ flux surveys were carried out with a dense electric resistivity survey called electric resistivity tomography (ERT) [Finizola *et al.*, 2006, 2009, 2010; Revil *et al.*, 2008, 2011; Barde-Cabusson *et al.*, 2009; Siniscalchi *et al.*, 2010; Byrdina *et al.*, 2013, 2014; Brothelande *et al.*, 2014; Isaia *et al.*, 2015]. Comparing the structure of ERT with profiles of self-potential, diffuse CO₂ flux, and soil temperature, the previous studies above showed that fractures such as tectonic and regional faults and hidden ring-faults of the crater can be pathways of ascending hydrothermal fluids and that the locations of diffuse CO₂ anomalies reflect areas of the ascending fluids [e.g., Finizola *et al.*, 2010]. The previous studies listed above focused only on the regional tectonic or volcano-tectonic structures as possible pathways of the ascending hydrothermal fluids.

As mentioned above, most previous studies of the diffuse CO₂ degassing have related the DDS to the fractures in the volcanoes. However, looking at the previous studies carefully, some DDS is not related with the fractures. Conversely, some diffuse degassing surveys do not show the diffuse CO₂ anomalies for locations with expected fractures. For instance, at Solfatara of Pozzuoli, the DDS was not observed in NW corner of the study area where a possible pathway corresponding to a crater rim was present [Chiodini *et al.*, 2008, fig. 6]. In their survey, the DDS without a relation to the mapped fractures was also found in the SE sector of the study area, which was just explained by a possible presence of the hidden tectonic structure [Chiodini *et al.*, 2008, fig. 6]. At the summit area of Vesuvio volcano (Italy), CO₂ flux anomalies were found on the inner slopes of the crater and along the crater rims but not found on the northern edge of the crater [Fronzoni *et al.*, 2004, fig. 6]. The latter area seemed to have similar structures with the area of diffuse CO₂ anomalies, but the absence of the diffuse degassing in this area was not explained with details. In these

previous studies, cause for these examples that showed the inconsistency between the diffuse CO₂ distributions and the tectonic structures was seldom considered. To understand the controlling factors of diffuse CO₂ flux distributions, it is probably important to consider other factors together with the regional and volcano-tectonic structures.

1.3.2 *Controlling factors on hydrothermal fluid ascent revealed from distributions of fumaroles and heat anomalies*

As a primary control of the hydrothermal ascent, the tectonic control including regional and volcano-tectonic structures has often been considered. The tectonic structures are usually formed by regional and local stress field. *Arnórsson* [1995] reported that the high-temperature geothermal areas were located along the active volcanic belts and the margin to them in Iceland. In his study, the geothermal fluids had a root in rift-related intrusive magma revealed from the studies at polygenetic volcanoes, and the main orientation of the dikes under the volcanic edifice corresponded to the maximum compressive stress of the regional stress field. This study showed that the regional tectonic structure control was effective on the locations of the fumaroles. The volcano-tectonic structure control is also obvious in fluid ascent. For example, *Geshi* [2009] showed at Miyakejima volcano (Japan) that the locations of the eruption sites and fumaroles in the summit caldera were limited in the southern-half part of the caldera, where ascending pathway of magma along the tilted ring faults was concentrated.

Although the structure control is highly effective on the locations of fumaroles, alternative possibilities have been proposed. One is the control of stress field induced by load of the volcanic edifices, and the other is control of lithology that can form contrasts of permeability in the volcanic edifices. *Fiske and Jackson* [1972] studied the relation of the dike orientation of Hawaiian volcanoes to the regional structure and the topography-induced stress field. They showed that the radial patterns of the dikes were strongly influenced by the gravitational stresses accompanying the influence of the rift structure. *McGuire and Pullen* [1989] examined the fissure locations and orientations at Etna volcano (Italy) and compared the results to ground deformation measurements and laboratory experiments. They proposed that the regional tectonic stress was displaced by the gravitational stress that was generated by the gross morphology of the volcano and was modified by local topography. In their studies, the dike orientation near a truncated edge of the volcanic edifice at Valle del Bove was parallel to topographic contours of the edge [*McGuire and Pullen*, 1989].

On the relation of the topography-induced stress field and the vent locations in the volcanic edifice, a recent study by *Schöpa et al.* [2011] clarified the topography control on the case of the Fossa cone of Vulcano Island. They conducted soil temperature measurements to obtain the lo-

cation of thermal anomalies. The results of TIR images and thermocouple measurements showed that fumarolic areas and high temperature anomalies made by ascending fluids were distributed along the upper part of the crater rims corresponding to the crests (high-topography areas) and were not observed at the crater floor or at the lower part of the inner slopes of the crater. To understand the observed thermal anomaly distributions at Vulcano, they conducted a numerical modelling using a finite element method. In the numerical modelling, they prepared a linear elastic and isotropic body of the Fossa cone with a size of $2250 \text{ m} \times 2250 \text{ m} \times (4000 \text{ m} + \text{elevation})$ and with rigid boundaries. The load of gravity was only included as a force subjecting the body. The results of the model calculation [Schöpa *et al.*, 2011, figs. 4, 5, and 6] showed that, at depth, the maximum compressive stress (σ_1) was vertical and the minimum compressive stress (σ_3) was horizontal and normal to the vertical transection, which meant that σ_3 was parallel to the crater rims. Near the surface, σ_1 became parallel to the surface and σ_3 reoriented perpendicular to the surface at the flanks and near vertical at the crater floor and the crater rims. These results suggested that pathways consisting of hydrofractures were formed along the crater rims and hydrothermal fluids from depth ascended to the crests of the craters where low horizontal compression occurred. Based on these results, they concluded that the overall distribution of the fumaroles at the Fossa cone was controlled by topography [Schöpa *et al.*, 2011].

The other possible control on the fluid ascent is lithology. Based on field observations at extinct geothermal fields in Iceland and model calculations, Gudmundsson *et al.* [2002] showed that over-pressurized hydrofractures could form permeable pathways in horizontal and vertical discontinuities. Schöpa *et al.* [2011] also reported that high temperature anomalies reflected boundaries of lithology due to the difference of permeability of each layer.

Concluding the previous studies presented in this section, the locations of the fumaroles and heat anomalies are influenced by regional tectonic and volcano-tectonic structure control, topography control, and lithology control. Particularly, the importance of topography control is clearly represented by Schöpa *et al.* [2011]. More examples on the topography control should be accumulated in order to ascertain the importance of the topography control on distributions of the fumarolic activities and heat anomalies.

After the study of Schöpa *et al.* [2011], the idea that the combination of structure, topography, and lithology controls influences the hydrothermal fluid ascent is gradually applied to the studies of soil temperature measurements and diffuse CO_2 flux measurements. At Yasur–Yenkahe volcanic complex (Vanuatu), Peltier *et al.* [2012] revealed that, based on the TIR images and soil temperature measurements, high temperature anomalies were related to planar stratification leading to lateral spreading of hydrothermal fluids and structures such as active faults and

paleo-crater rims. From TIR survey and grain-size analysis of soils at Stefanos crater of Nisyros Island, *Pantaleo and Walter* [2014] showed that warmer areas were localized near the edge of the crater floor within permeable soil, which indicated the lithology control influenced as well as regional tectonic and volcano-tectonic structures. Based on diffuse CO₂ flux measurements and terrain analysis from lidar surveys, *Hutchison et al.* [2015] presented that, at Aluto volcanic complex (Ethiopia), the diffuse CO₂ pathways were controlled not only by regional pre-/post-caldera structures but also by local topography and lithology. *Morita et al.* [2016] recently revealed, by a simple comparison of profiles of diffuse CO₂ flux and elevation, that the diffuse CO₂ flux anomalies at Asama volcano (Japan) were related to local fractures and topography. The influence of the topography and/or lithology controls on the diffuse CO₂ degassing has just started to be considered. For the topography control on the diffuse CO₂ flux distributions, it has been revealed only by a simple comparison of CO₂ flux values and an elevation profile along a limited number of survey lines [e.g., *Hutchison et al.*, 2015; *Morita et al.*, 2016]. To make the topography control clearly visible, it is more adequate to compare the spatial distributions of diffuse CO₂ flux with topography of the observed area.

1.4 Objectives of this study

On the fluid migration in the volcanic edifice based on the heat anomaly studies, the regional tectonic and volcano-tectonic structures, lithology, and topography are proposed to be considered as the controlling factors [e.g., *Schöpa et al.*, 2011]. This idea should be considered also for the ascent process of the diffuse CO₂. However, the topography and lithology controls on the diffuse CO₂ degassing have not been considered sufficiently, yet. Particularly, the topography control on the diffuse CO₂ flux distributions has been only revealed by the simple comparison of profiles of the CO₂ flux and elevation [e.g., *Hutchison et al.*, 2015; *Morita et al.*, 2016].

As noted in the last part of **Section 1.3.1**, the diffuse CO₂ flux distributions sometimes show the inconsistency with the tectonic structures [e.g., *Fron dini et al.*, 2004; *Chiodini et al.*, 2008]. This point is not explained well in the previous studies. Even applying the topography and lithology controls to these examples, the absence of the DDS near the tectonic structures cannot be fully explained. This probably indicates possibilities of other controlling factors on the DDS.

Soil temperature measurements sometimes miss weak temperature anomalies where the vapor is totally condensed before reaching to the surface [*Aubert and Baubron*, 1988]. In contrast, the diffuse CO₂ flux measurements may be more effective to detect areas of ascending hydrothermal fluids without heat anomalies [e.g., *Giammanco et al.*, 2016]. Therefore, to elucidate the controlling factors on the hydrothermal fluid ascent, the diffuse CO₂ flux measurements are probably

more promising.

The first objective of this study is to reveal the controlling factors on the diffuse CO₂ degassing, especially influence of the topography control, using spatial distributions of diffuse CO₂ flux anomalies and topography. The second objective is to examine the possibilities of other controlling factors on the diffuse CO₂ degassing.

For the objectives of this study, summit area of Asama volcano is probably suitable. Asama volcano is one of the most active volcanoes and is one of the six major degassing volcanoes in Japan [Mori *et al.*, 2013]. Persistent plume emissions occur at the summit vent both in active and quiescent periods of the volcanic activity. A presence of diffuse CO₂ emission at the summit area has been recognized by measurements in a very limited area of the summit [Mori *et al.*, 2002, unpublished data]. The surface of the summit area is almost covered with pyroclastic deposits and there is hardly any vegetation in the summit area. Especially, the lack of vegetation in the summit area has an advantage of avoiding unnecessary influence by biogenic CO₂ discharge and of detecting even weak volcano-hydrothermal CO₂ signals. The summit area of the volcano consists of an outer collapsed crater and a pyroclastic cone inside the crater, and the morphological shape of the summit area is relatively simple and is suitable for studying the topography control and/or other controlling factors. More details of Asama volcano are written in **Section 2.4.3**. Although Asama volcano has the high degassing activities, the diffuse CO₂ degassing of Asama volcano has not been studied well and little is known about the distribution and the magnitude of the diffuse CO₂ degassing. Thus, the objectives of this study also include revealing the characteristics of the degassing system of Asama volcano including the diffuse degassing.

Chapter 2

Geological and volcanological background of Asama volcano

2.1 Geology of Asama volcano

Asama volcano is a volcanic complex located in the central part of Japan (an inset of **Fig. 2.1**). It stands in the eastern part of Eboshi–Asama volcano group and consists of Kurofu, Maekake, and Hotokeiwa volcanoes from the west (**Fig. 2.1**). The oldest edifice is Kurofu stratovolcano (2,404 m a. s. l.) that mainly consists of andesite lava and pyroclastic materials [Aramaki, 1963, 1993]. The volcanic activity of Kurofu volcano started about 100,000 years ago and ended with a sector collapse at 24 ka, forming a horse-shoe shape caldera open to the east side [Aramaki, 1993; Takahashi and Yasui, 2013] (**Fig. 2.1**). From 20 ka to 11 ka, Hotokeiwa volcano was formed in the most eastern part of Asama volcanic complex (**Fig. 2.1**) with dacite–rhyolite lavas and pyroclastic flow deposits [Aramaki, 1993; Takahashi and Yasui, 2013]. Volcano body of Hotokeiwa is now almost covered with Maekake volcano. Ko-Asama dacite lava dome located about 4 km east of the summit of Maekake volcano (**Fig. 2.1**) was also formed in this period.

The present activity of Asama volcano is focused on Maekake volcano (2,568 m a. s. l.) that stands 2 km east of Kurofu volcano (**Fig. 2.1**). It has a conical body elongated in E–W. After two active periods in 9.2–8.6 ka and 6.3–5.2 ka, the present active period of Maekake volcano began with a plinian eruption about 1,650 years ago [Takahashi and Yasui, 2013]. After this eruption, three plinian eruptions occurred in 1108, 1128, and 1783, and many vulcanian eruptions occurred intermittently [Takahashi and Yasui, 2013]. During the 1108 eruption, Maekake crater with a diameter of 1.3 and 0.9 km in E–W and N–S, respectively (**Fig. 2.1**), was formed by a collapse of the summit [Takahashi and Yasui, 2013; Yasui and Takahashi, 2015]. Recently, Yasui and Takahashi [2015] proposed, based on geological studies at the summit area, that the elliptical shape of Maekake crater elongated in E–W resulted from the collapse after a fissure eruption with the E–W trend or from sequential collapses of at least two rounded craters from west to east. These fissures or collapsed craters that presumably exist inside Maekake crater have not been observed directly by the researchers because Kamayama cone almost covers the inside of Maekake crater. In the 1783 eruption, Kamayama cone grew by spatter or fountain-fed lava deposited in Maekake crater [Yasui and Koyaguchi, 1998, 2004; Yasui and Takahashi, 2015], and the top of Kamayama

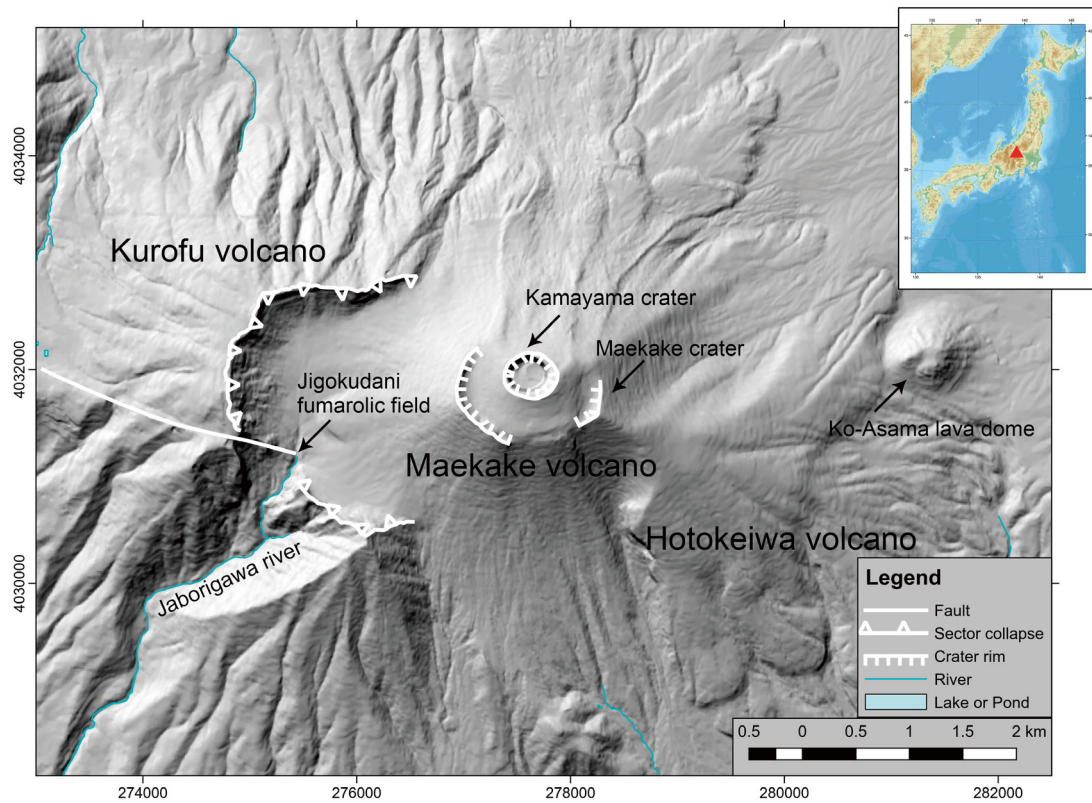


Fig. 2.1 A map of Asama volcano [modified from *Morita et al., 2016*]. The location of Asama volcano is shown as a red triangle in the inset. A digital elevation model used in the inset is from GMRT 3.2 [*Ryan et al., 2009*]. Names of main sites of Asama volcano are shown. Coordinates are shown in meter of easting and northing (WGS84, UTM Zone 54 North). A digital elevation model (10-m grid) is provided by the Geospatial Information Authority of Japan.

cone consequently became higher than Maekake crater rims. Kamayama cone has a crater with a diameter of 500 and 440 m in E–W and N–S, respectively, and a depth of 200 m (**Fig. 2.2a**), and the surface of the cone is now almost covered with pyroclastic deposits by the vulcanian eruptions after the 1783 eruption (**Fig. 2.2b**). Deposits around Maekake crater from the 1108 eruption to the 1783 eruption can be seen in crater walls of western Maekake crater and of Kamayama crater [*Yasui and Koyaguchi, 1998, 2004; Yasui and Takahashi, 2015*].

The recent volcanic activity was high from 1900s to 1960s with many explosive eruptions [*Japan Meteorological Agency, 2013*]. The Volcanic Explosivity Index (VEI) [*Newhall and Self, 1982*] of these eruptions were up to 3. The most recent activity over the last 50 years has been characterized by vulcanian eruptions at intervals of about 5–15 years and by persistent degassing from the main vent of Kamayama crater. Recent explosive events occurred in 1973, 1982–1983, 1990, 2003, 2004, 2008–2009, and 2015. The VEIs of 1973, 1982–1983, and 2004 eruptions were 1 or 2 and those of the other eruptions were less than 1 [*Japan Meteorological Agency, 2013*].



Fig. 2.2 **a** A composite panoramic view of Kamayama crater from the east side (taken on 26 October 2012). The location of the main vent of Kamayama crater is shown with a red circle. Low to moderate temperature fumaroles are also located around the main vent and on the inner wall of the crater. **b** A composite panoramic view of Kamayama pyroclastic cone from the southwest side of the summit area (taken on 26 October 2014). The western Maekake crater wall is partly seen on the left.

2.2 Geophysical and geochemical observations of Asama volcano

Seismological observation at Asama volcano first started in 1910 [Omori, 1912], which was one of the earliest seismic studies at active volcanoes in Japan. Based on waveforms from the seismic observations, Minakami [1960] classified the observed seismograms into four types: A-type (volcano-tectonic earthquakes), B-type (long-period earthquakes), explosive earthquakes, and tremors.

A modern monitoring network of geophysical observation has been maintained by Japan Meteorological Agency (JMA), Earthquake Research Institute of The University of Tokyo (ERI), and National Research Institute for Earth Science and Disaster Resilience (NIED) since the beginning of the twenty-first century [Aoki *et al.*, 2013]. Now, the monitoring network of Asama volcano is one of the most developed monitoring networks in the world. There are 30 seismometers around Asama and Eboshi volcanoes, 16 of which are broadband sensors [Aoki *et al.*, 2013]. Continuous global navigation satellite system (GNSS) observations started in the mid-1990s, and currently there are 15 stations within 20 km of the summit, four within 4 km and two on the rim of Kamayama crater [Aoki *et al.*, 2013]. There are also 10 tiltmeters, nine microphones, one laser

range-finder system and two cosmic ray muon detectors at present [Aoki *et al.*, 2013]. Insights obtained from the geophysical observations are shown in the following section.

Geochemical observation of volcanic gas from Asama volcano started in 1934 by analyzing chemical compositions of bubbling gas from Jigokudani fumarolic field (located about 2.3 km southwest down the flank of Maekake volcano from the summit crater, **Fig. 2.1**), spring water around Asama volcano, and ash leachates [Noguchi, 1935, 1936, 1938a, 1938b]. He used selective absorbing solutions for sampling of the bubbling gas, and found that CO₂ and H₂S in the bubbling gases accounted for about 79 % and 1 % in volume, respectively [Noguchi, 1935, 1938b]. This is one of the earliest volcanic gas data in Japan [Notsu, 2016]. Chemical composition and deuterium content of the spring water were also reported by the same group [Shibata *et al.*, 1937].

The chemical compositions of volcanic gas emitted from the fumaroles in Kamayama crater has been studied only by measuring the volcanic plumes or ash leachates because the fumaroles are inaccessible due to the steepness of Kamayama crater wall [Shinohara *et al.*, 2015]. Noguchi and Kamiya [1963] placed KOH solutions in small boxes around Kamayama crater and Jigokudani fumarolic field to monitor contents of S, Cl, and CO₂ in the solutions. They concluded that the S/Cl ratio of the volcanic gas from Kamayama crater increased one month before a huge eruption in 1958 and that the volcanic gas composition of Jigokudani fumarolic field did not correlate to the changes of volcanic activity [Noguchi and Kamiya, 1963]. Mori and Notsu [2005] conducted open-path Fourier transform infrared spectroscopy (OP-FTIR) measurements for the volcanic plumes and Nogami *et al.* [2008] measured compositions of the ash leachates during the 2004 eruptions. Their data were limited for S, Cl, and F contents because of the limitations of the methods. Volcanic gas composition including the major species such as H₂O and CO₂ was measured after the introduction of a portable multicomponent gas analyzer system (Multi-GAS) in 2004 [Shinohara *et al.*, 2015]. Results from the repetitive measurements using Multi-GAS and alkaline-filter pack techniques and an automated measurement of Multi-GAS showed that CO₂/SO₂ and H₂O/SO₂ ratios were apparently stable both in active and inactive periods [Shinohara *et al.*, 2015] (**Fig. 2.3a**). The average molar ratios during 2004–2014 were estimated to be CO₂/SO₂ = 0.8, H₂O/SO₂ = 30, H₂/SO₂ = 0.06, SO₂/H₂S = 6, SO₂/Cl = 5, and Cl/F = 10 [Shinohara *et al.*, 2015].

Monitoring of SO₂ emission rates at Asama volcano began in 1970s using the correlation spectrometer (COSPEC) [Moffat *et al.*, 1972; Okita and Shimozuru, 1974]. Since 2003, measurements using a miniature ultraviolet (UV) spectrometer named COMPUSS [Mori *et al.*, 2007] have been conducted by JMA, Geological Survey of Japan (GSJ), Volcanic Fluid Research Center of Tokyo Institute of Technology (TITECH), and Geochemical Research Center of The University of Tokyo (GCRC), and the SO₂ flux data for 1972–2012 were summarized in Ohwada *et*

al. [2013]. The average SO₂ flux value during inactive periods was about 200 t day⁻¹, but the flux values during the unrest and eruptive periods increased over 500 t day⁻¹ up to 5,600 t day⁻¹ [Ohwada *et al.*, 2013; Japan Meteorological Agency, 2016] (Fig. 2.3a).

2.3 Magma plumbing system and degassing system of Asama volcano

Recent geophysical studies revealed the magma pathway from depth to the surface [Aoki *et al.*, 2005, 2009, 2013; Takeo *et al.*, 2006; Aizawa *et al.*, 2008; Nagaoka *et al.*, 2012]. A deep magma chamber observed by seismic interferometry is thought to exist at 5–10 km b. s. l. about 8 km WNW of Kamayama crater [Nagaoka *et al.*, 2012]. Above the chamber, the intruded dike of the recent eruptions estimated by GNSS surveys resides at 1–3 km b. s. l. [Aoki *et al.*, 2005, 2013; Takeo *et al.*, 2006]. A deep spherical pressure source obtained by levelling surveys since 1902 is located at 5–6 km b. s. l. and 5 km WNW of the summit [Murase *et al.*, 2007]. Based on magnetotelluric survey in 2005 and 2006, Aizawa *et al.* [2008] found electrically high-resistive bodies above the intruded dike under Kurofu volcano, and concluded that these resistive bodies corresponded to old solidified magma with low porosity. High P-wave velocity structure found by an active seismic source experiment corresponded to the locations of the intruded dike and the resistive bodies, which also indicates old solidified magma resides under Kurofu volcano [Aoki *et al.*, 2009]. This old solidified magma interrupts the present magma to ascend to the upper level under Kurofu volcano, thus the magma moves horizontally from the dike to the area under Kamayama crater and then vertically ascends to the vent [Takeo *et al.*, 2006; Aoki *et al.*, 2013]. Using GNSS and laser rangefinder measurements, Takagi *et al.* [2005] estimated the location of two pressure sources in the 2004 eruption: one is just under Kamayama crater at 2,200 m a. s. l. and the other is about 1.5 km east of the summit at the sea level depth. The latter pressure source is not recognized in other measurement to date. At a shallow depth under the summit area of Maekake volcano, an electrically low-resistive body (<10 Ω m) was revealed to exist by the magnetotelluric survey [Aizawa *et al.*, 2008]. They interpreted this low-resistive zone as a hydrothermal system in which the fracture network was well developed [Aizawa *et al.*, 2008]. However, fumarolic areas indicating the hydrothermal emission are not known except for the main active crater of Kamayama cone. In recent studies using electrical and electromagnetic measurements, a low-resistivity structure in volcanic edifices could be interpreted not only as hydrothermal fluids but also as layers of clay (smectite) minerals [Nurhasan *et al.*, 2006]. Hence, the main cause of the low-resistive body under the summit area of Maekake volcano remains question whether it consists of hydrothermal fluids and/or layers of clay minerals.

Degassing activity of Asama volcano persistently occurs both in active and inactive periods

[Ohwada *et al.*, 2013; Kazahaya *et al.*, 2015a; Shinohara *et al.*, 2015]. This volcano is considered one of the six major degassing volcanoes in Japan [Mori *et al.*, 2013]. SO₂ flux, plume CO₂/SO₂ ratio, and daily number of B-type (long-period) earthquakes from 2004 to the present are shown in **Fig. 2.3**. SO₂ flux values seem to have correlation with the number of B-type earthquake (**Fig. 2.3**), as reported by Ohwada *et al.* [2013]. They also have a correlation with baseline lengths of continuous GNSS measurements [Kazahaya *et al.*, 2015a]. Although SO₂ flux values in inactive periods are much lower than those in active periods, the daily average flux values in inactive periods ranged from 50 to 400 t day⁻¹. From this persistent degassing activity, Ohwada *et al.* [2013] suggested that the degassing system was supported by magma convection in the conduit [Kazahaya *et al.*, 1994; Shinohara, 2008]. While SO₂ flux values have large variations, volcanic gas compositions do not show significant variation in active and inactive periods (**Fig. 2.3a**). Based on minor changes of the SO₂/Cl ratio after the eruptions, the degassing both in active and inactive periods is estimated to be occurred at a pressure near atmospheric level [Shinohara *et al.*, 2015]. This corresponds to the facts that petrological characteristics of glasses in the ash of the 2004 eruption suggest that the magma was degassed and crystallized at lower pressures [Shimano *et al.*, 2005], and that the magma head during the 2004 eruption estimated by absolute gravity measurements was located at the shallow level [Kazama *et al.*, 2015]. Model study of Kazahaya *et al.* [2015a] indicates that the degassing magma is supplied by the conduit magma convection and the degassing system is connected from the deep magma chamber through the dike-like conduit to the main vent.

Another type of degassing, a gas burst (ash-free eruption), sometimes occurs both in active and inactive periods following very-long-period (VLP) seismic pulses with durations of 5–30 s [Kazahaya *et al.*, 2011; Maeda and Takeo, 2011]. The source of the VLP pulses are located at 100–150 m below the crater bottom beneath the northern rim of the crater [Maeda and Takeo, 2011]. This location corresponds to a fracture zone beneath the crater bottom obtained by three-dimensional density tomography of cosmic ray muon radiography [Tanaka *et al.*, 2010]. The amount of SO₂ emitted by these events have a linear correlation with the VLP seismic moment [Kazahaya *et al.*, 2011]. The volcanic gases discharged after the VLP events show chemical compositions similar to those of gases continuously emitted without VLP events [Kazahaya *et al.*, 2015b; Shinohara *et al.*, 2015]. This similarity indicates that both gases from persistent degassing and gas-burst event have the same source, which is the gas from the shallow degassing magma [Kazahaya *et al.*, 2015b; Shinohara *et al.*, 2015]. The amount of SO₂ emitted by these gas-burst events in active and inactive periods accounts respectively 10–50 % and 5–10 % of total SO₂ emission from the volcano [Kazahaya *et al.*, 2015b].

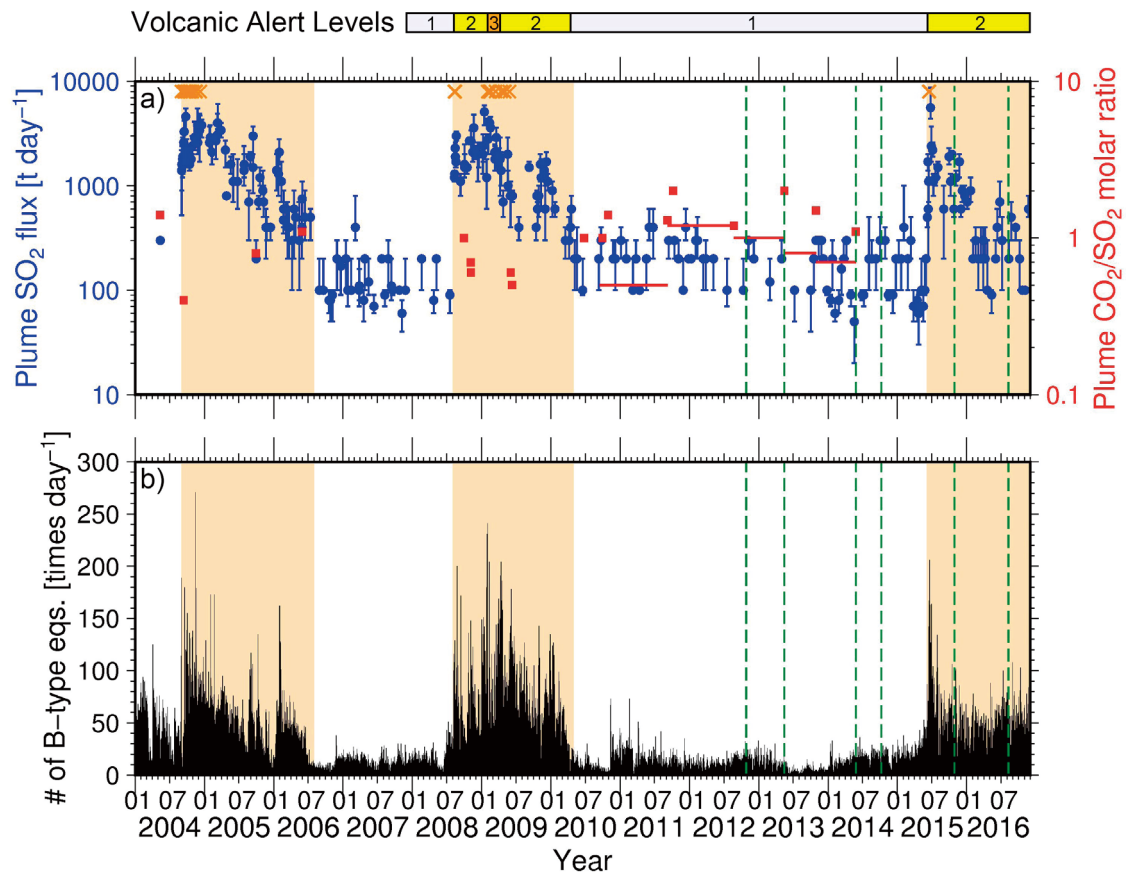


Fig. 2.3 a Daily average plume SO₂ flux (blue circle) and plume CO₂/SO₂ ratio (red square and line), and b daily number of B-type earthquakes (black histogram) at Asama volcano during 2004–2016 [modified from *Morita et al.*, 2016]. The SO₂ flux data are from *Ohwada et al.* [2013] and *Japan Meteorological Agency* [2016]. The CO₂/SO₂ ratios are from *Shinohara et al.* [2015]. Red squares and lines correspond to data from repetitive and automated Multi-GAS measurements, respectively. The seismic data are from *Japan Meteorological Agency* [2015b] and the monthly reports of JMA (available on the website at http://www.data.jma.go.jp/svd/vois/data/tokyo/STOCK/monthly_v-act_doc/monthly_vact_306.html). Orange crosses in 2004, 2008–2009, and 2015 indicate eruptions. Volcanic alert levels issued by JMA are also shown in the upper part of the figure. Shaded areas correspond to the active periods of plume degassing. Green dashed lines show dates of the observations of this study (**Section 3.1**).

2.4 Recent volcanic activities of Asama volcano

The diffuse degassing surveys of this study were conducted during 2012–2016. This section focuses on the recent volcanic activities before and during the surveys and on the characteristics of Asama volcano as the field of this study. During the survey period, very small eruptions occurred in June 2015 and the volcanic activity after the 2015 eruption was considered as high (**Section 2.4.3**). JMA has been issuing the volcanic alert level for Asama volcano since December 2007 (shown in the uppermost part of **Fig. 2.3**). When the volcanic activity is calm, it is set at Level 1 (“Potential for increased activity”) and the summit area within 500 m of Kamayama crater is restricted. Even at Level 1, the summit area inside the most part of Maekake crater (the study area of this study, **Section 3.1**) is restricted for climbers and visitors. When the volcanic activity

increases, the volcanic alert level becomes Level 2 (“Do not approach the crater”) or Level 3 (“Do not approach the volcano”), and the restricted area enlarges within 2 or 4 km of Kamayama crater, respectively. The higher levels (Level 4, “Prepare to evacuate”, and Level 5, “Evacuate”) have not issued for Asama volcano since the introduction of the volcanic alert levels.

2.4.1 The 2004 eruption

The 2004 eruptive activity that started with a vulcanian explosion on 1 September 2004 was characterized by five vulcanian explosions, intermittent strombolian eruptions, and many small-scale eruptions [Nakada *et al.*, 2005; Yoshimoto *et al.*, 2005]. The eruptive activity continued until December 2004. The volume of erupted magma (DRE) was estimated to be $2 \times 10^6 \text{ m}^3$, most of which filled the floor of Kamayama crater [Nakada *et al.*, 2005]. The total amount of ash that fell during the 2004 eruption was more than $1.6 \times 10^8 \text{ kg}$, which was about 2 % of the erupted magma in the crater floor [Yoshimoto *et al.*, 2005]. SO_2 flux values (**Fig. 2.3a**) increased with the eruption and were higher than those of inactive periods until August 2006 [Ohwada *et al.*, 2013; Japan Meteorological Agency, 2016]. The daily average values between September 2004 and August 2006 ranged from 200 to $4,600 \text{ t day}^{-1}$ [Ohwada *et al.*, 2013; Japan Meteorological Agency, 2016].

From the continuous GNSS observations, Aoki *et al.* [2005] and Murakami [2005] reported that dike intrusion events occurred between July 2004 and March 2005. The size of the dike was estimated to be $4 \text{ km} \times 2 \text{ km}$ at 4 km WNW of the summit [Aoki *et al.*, 2005; Takeo *et al.*, 2006]. The depth of the top of the dike was estimated to be 1 km b. s. l. [Aoki *et al.*, 2005; Takeo *et al.*, 2006]. The total intruded volume was estimated to be $6.8 \times 10^6 \text{ m}^3$, which was much larger than the volume of the erupted magma [Aoki *et al.*, 2005; Nakada *et al.*, 2005]. Precise distribution of hypocenters between January 2004 and October 2005 obtained by double-difference algorithm showed that magma was supplied horizontally from the dike to the area immediately under Kamayama crater and vertically from this area to the main vent of Kamayama crater [Takeo *et al.*, 2006].

2.4.2 The 2008–2009 eruption

In July 2008, the seismic activity started to elevate and further increased in 8 August. The volcanic alert level raised to Level 2 on the same day (**Fig. 2.3**). This led to minor eruptions on 10, 11, and 14 August [Aoki *et al.*, 2013]. On 1 February 2009, the volcanic alert level raised to Level 3 (**Fig. 2.3**). In the midnight of the next day (2 February 2009), a vulcanian eruption occurred with the ejection of ash and ballistics. The total amount of ash was estimated to be $2.7\text{--}3.1 \times 10^7 \text{ kg}$ [Maeno *et al.*, 2010]. Juvenile glasses of the ash accounted less than 1 wt. % of the sample [Maeno

et al., 2010], suggesting that the erupted materials were from the near surface. This is consistent with insignificant mass loss in the crater observed by cosmic ray muon radiography [Tanaka *et al.*, 2009; Aoki *et al.*, 2013]. The volcanic alert level degraded to Level 2 on 7 April 2009. After this eruption, minor eruptions continued until the end of May 2009 and the volcanic alert level had been set at Level 2 until 15 April 2010 (**Fig. 2.3**). SO₂ flux values increased with the 2008 eruption and were high until May 2010 [Ohwada *et al.*, 2013; Japan Meteorological Agency, 2016]. The daily average values between August 2008 and April 2010 ranged from 300 to 5,100 t day⁻¹ (**Fig 2.3a**) [Ohwada *et al.*, 2013; Japan Meteorological Agency, 2016].

2.4.3 Volcanic activities and characteristics of Asama volcano as the field of this study

Since the end of the eruptive activities in 2009, the volcanic activities represented by seismicity and SO₂ flux remained low and the volcanic alert level had been set at Level 1 (**Fig. 2.3**). In April 2015, seismic activity began to elevate and continuous GNSS observations indicated inflation trend since the beginning of June [Japan Meteorological Agency, 2015a]. The seismic activity further increased on 7 June and daily average SO₂ flux value also increased to 1,700 t day⁻¹ on 11 June [Japan Meteorological Agency, 2016] (**Fig. 2.3**). The volcanic alert level raised to Level 2 on 11 June. After these leading unrest signals, tiny eruptions occurred on 16 and 19 June and trace amount of ash was ejected by the eruptions. Seismic activity and SO₂ flux values are still heightened at present (December 2016) and the volcanic alert level has continued to be Level 2 (**Fig. 2.3**). The daily average SO₂ flux values from June 2015 to November 2016 ranged from 90 to 5,600 t day⁻¹ [Japan Meteorological Agency, 2016].

Fumarolic activity of the summit area is mainly located inside Kamayama crater. The main active vent is on the bottom inside Kamayama crater (“Main vent” in **Fig. 2.2a**). Surrounding the main vent low to moderate temperature fumaroles are visible on the crater bottom and on the inner wall of Kamayama crater, but they are inaccessible because the crater wall is very steep (**Fig. 2.2a**) [Shinohara *et al.*, 2015]. Excluding these fumarolic activities inside Kamayama crater, there are basically no fumarolic activities inside and on the flank of Maekake volcano. The only exceptions are the northern edge of the inner wall of western Maekake crater. At the northern edge of the western Maekake crater wall, very weak steaming from cracks on the crater wall without sulfur odor are rarely visible. The temperatures of the steam ranged from 36 to 53 °C [Noguchi, 1938b]. This fumarole in the western Maekake crater wall is thermally weak [Suto, 1998] and it is very different from normal fumarolic areas with visible fumaroles and heat anomalies.

Temperatures of the ground surface of the summit area of Maekake volcano have been reported with thermal-infrared (TIR) cameras of JMA or airborne hyperspectral scanners of NIED

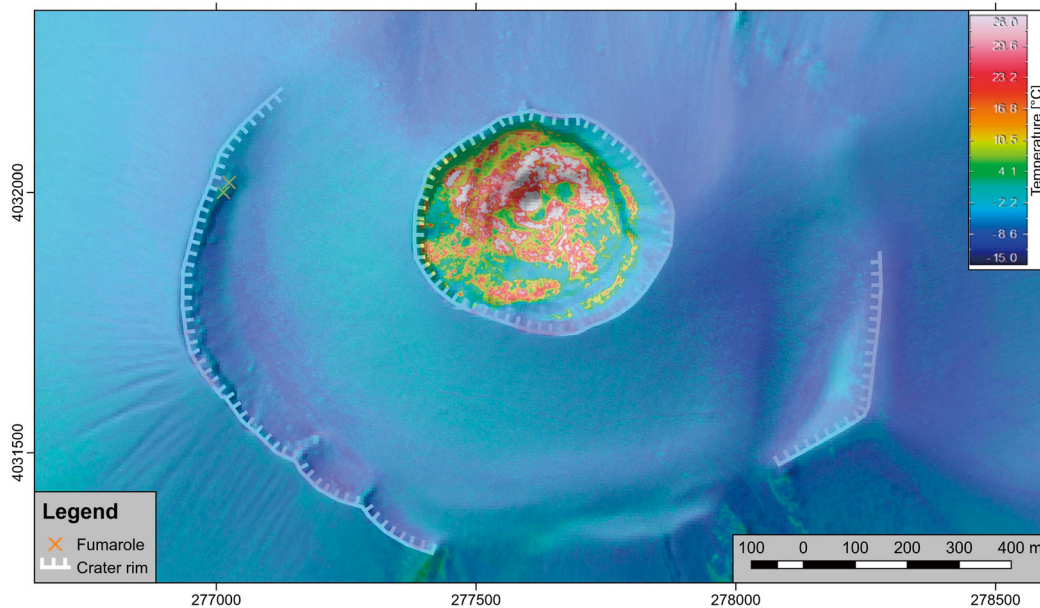


Fig. 2.4 An aerial TIR image of the surface temperature measured on 4 November 2015 [Terada *et al.*, unpublished data, 2015]. Coordinates are shown in meter of easting and northing (WGS84, UTM Zone 54 North). A digital elevation model (5-m grid) is provided by the Geospatial Information Authority of Japan.

[Jitsufuchi, 2011], and high-temperature anomalies are found only inside Kamayama crater and not in the other areas of the summit. The measurement temperature range of the cameras and the scanners in these reports was set in high-temperature range (at least a few hundred degrees Celsius) to measure high-temperature anomalies inside Kamayama crater. This may be one of the reasons that the temperature anomalies were not detected outside Kamayama crater. Recently, the aerial TIR images of the surface temperature focusing on low-temperature range were obtained on 4 November 2015 in cooperation with Dr. Akihiko Terada, Volcanic Fluid Research Center, Tokyo Institute of Technology. The images were captured using a TIR camera H2630 (a view angle of $21.7^{\circ} \times 16.4^{\circ}$, Nippon Avionics Co., Ltd.) from 4,000 m altitude at about 19:00 of local time after the sunset. The range of measurement temperature was set between -40 and 120 °C to detect low temperature anomalies. The orthoimage of the obtained temperature (about 1.4 m grid) is shown in **Fig. 2.4**. To show more detailed temperature distributions, the temperature scale shown in **Fig. 2.4** is set between -15 to 36 °C. The high temperature anomalies were obtained inside Kamayama crater around the main vent and fumaroles showing the temperature higher than the upper limit of the showing scale (36 °C). Outside Kamayama crater, the surface temperatures were lower than 4 °C with variations probably arising from local differences of solar radiations before the sunset. This data also indicates that the heat anomalies are absent on the surface of the summit area even though the TIR camera used the low temperature range.

As mentioned in **Section 2.1**, the summit area of Asama volcano consists of Kamayama

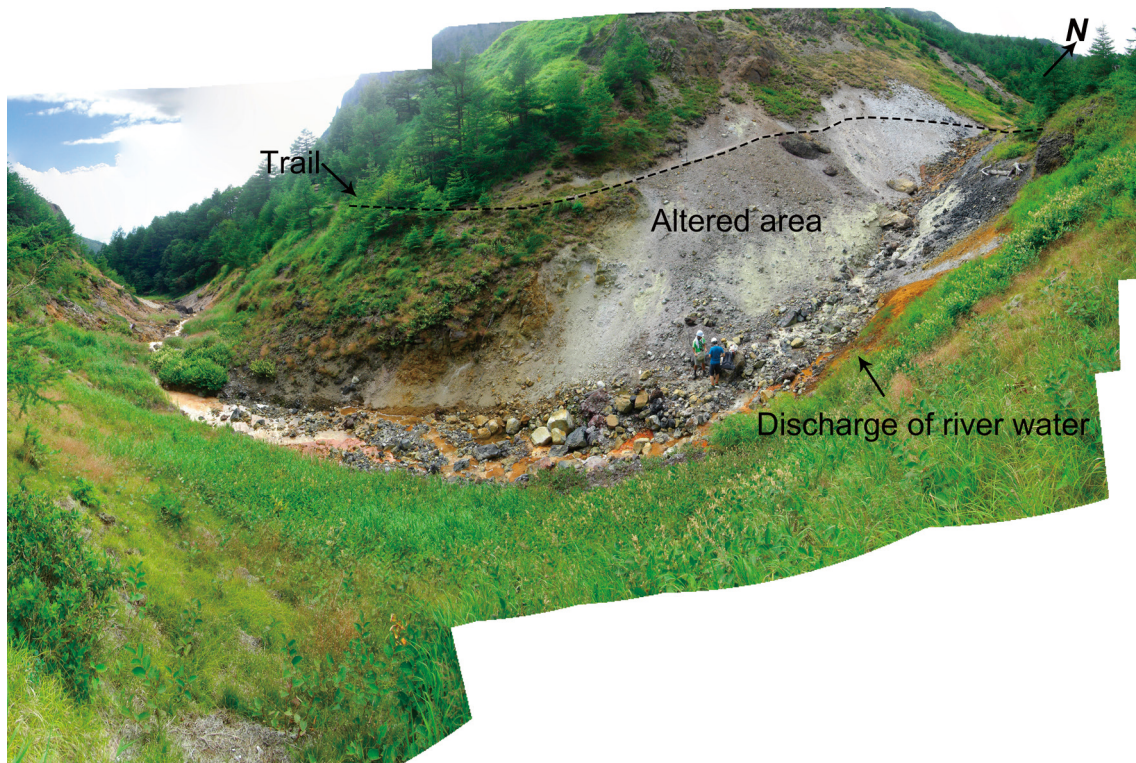


Fig. 2.5 A composite panoramic view of Jigokudani fumarolic field (taken on 9 August 2016). A yellowish altered area is located around the discharge point of Jaborigawa river. The river bottom is colored with iron oxide. There are no visible fumarolic activities nor heat anomalies in the area.

pyroclastic cone and the outer crater, Maekake crater, surrounding Kamayama cone (**Fig. 2.2b**). Due to these geological features, the summit area has a relatively simple morphology. The surface of the summit area is mainly covered with recent vulcanian deposits and the lithology of the summit area does not vary considerably with location (**Fig. 2.2b**). Moreover, the locations of crater rims and the fractures under the summit area are well studied by the previous geological studies. These characteristics are suitable for studying the controlling factors of hydrothermal fluid ascent, especially the topography control. The summit area does not have significant heat anomalies as mentioned above and there are no trees and hardly any vegetation. A background level of diffuse CO₂ flux values from the vegetated area is usually much higher than that from the non-vegetated area [e.g., *Cardellini et al.*, 2003b]. Thus, in the vegetated area, the influence of the biogenic CO₂ source is considered equally important as that of the volcano-hydrothermal source. The lack of these disturbing factors (significant fumarolic activities and vegetation) on the summit area also gives advantages on the study of diffuse CO₂ degassing.

Jigokudani fumarolic field is the only fumarolic area existing in the flanks of Asama volcano. In Jigokudani fumarolic field, although clear fumarolic activity with fumes or significant heat anomalies are currently absent, smell of H₂S often observed around the area. This smell is probably related to a yellowish altered area (20 m × 50 m) around the discharge point of

Jaborigawa river (**Fig. 2.5**). The yellow color is from sulfur precipitations. This area is thermally weak [*Suto*, 1998] and is very different from normal fumarolic areas with fumaroles and heat anomalies. Jigokudani fumarolic field was also surveyed for the objective of understanding the degassing system of Asama volcano.

Chapter 3

Observations and methods

3.1 An outline of the observations

As introduced in **Section 2.4.3**, the summit area of Asama volcano (a rectangle with “Summit” in **Fig. 3.1**) is suitable to elucidate the controlling factors of diffuse CO₂ degassing. For the purpose of this study, the study area was set inside Maekake crater (a region surrounded by a broken line in **Fig. 3.2**) excluding the interior of Kamayama crater because of inaccessibility. As shown in **Fig. 3.2**, the study area mainly consists of Kamayama pyroclastic cone and Maekake crater rims. The southern part of the western Maekake crater wall was a steep cliff and this area was excluded from the study area (the southern part of crater rims with “W. Maekake” in **Fig. 3.2**). The size of the study area was about 1 km in N–S and 1.5 km in E–W (**Fig. 3.2**).

The diffuse degassing surveys for this study at the summit area started in October 2012 and were conducted six times until August 2016 (green broken lines in **Fig. 2.3**, **Table 3.1**). As mentioned earlier, the volcanic alert level issued by JMA has been either Level 1 (“Potential for increased activity”) or Level 2 (“Do not approach the crater”) during the period (**Fig. 2.3**), and the summit area has been restricted for climbers and visitors (details of the restricted area are written in **Section 2.4**). The surveys in this study at the summit area were conducted by applying permission to the local government. During the surveys, emergency contact system was maintained for the safety of the observers in case of unexpected seismic and activity changes.

Four surveys of soil CO₂ flux were conducted separately on 26 October 2012, 15 May 2013, 27 May, and 8 October 2014 (green broken lines in **Fig. 2.3**, **Table 3.1**, **Fig. 3.2**) during the inactive period. The number of the measurement sites in a single survey was about 30–70 (**Table 3.1**), and the whole study area was too large to cover with only one or two sets of the CO₂ flux surveys. Thus, the whole study area was covered by the four surveys. May and October are suitable for the observations because the weather is generally calm at the summit area and the ground surface is not covered with snow. In the first observation in 2012, measurement sites were selected to cover the entire study area to understand the rough distributions of DDS as shown by black circles in **Fig. 3.2**. Based on the observed data of the first survey that showed diffuse CO₂ degassing anomalies only in the eastern side of the study area, denser measurements were performed on the eastern side of Maekake crater in the second survey (blue squares in **Fig. 3.2**) to clarify details and borders of the DDS. The third observation in May 2014 (orange triangles in **Fig. 3.2**) was especially

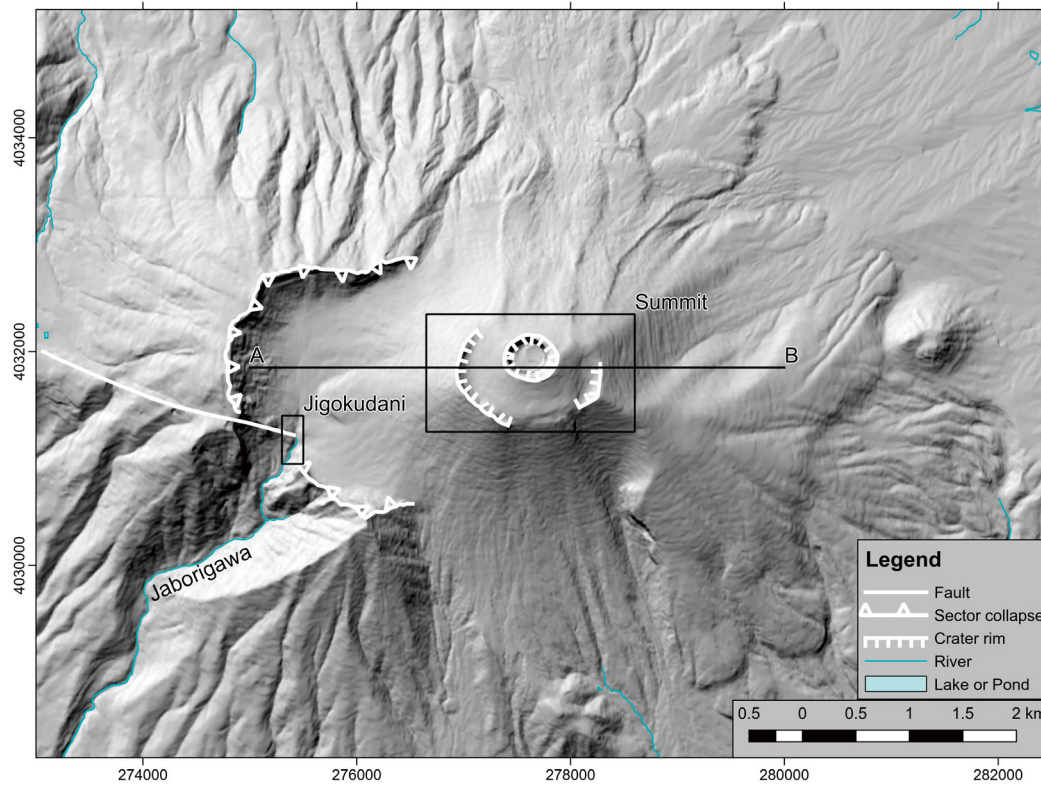


Fig. 3.1 A map of the study area [modified from *Morita et al., 2016*]. Rectangles with “Summit” and “Jigokudani” correspond to the study areas shown in the figures of **Chapters 4** and **5**. A line with “A” and “B” corresponds to the transection shown in **Fig. 5.6**. Coordinates are shown in meter of easting and northing (WGS84, UTM Zone 54 North). A digital elevation model (10-m grid) is provided by the Geospatial Information Authority of Japan.

intended to clarify borders of the DDS. The fourth observation (red inverted triangles in **Fig. 3.2**) was conducted on the western side of Maekake crater to bridge the sparse measurement sites on the south-western slope of the cone and to confirm that no degassing anomalies are recognized on the western side of Maekake crater. Dense measurements were also conducted around the very weak steaming vents at the northern edge of the western Maekake crater wall (mentioned in **Section 2.4**, orange crosses in **Fig. 3.2**) to reveal diffuse degassing condition of the area. The number of the measurement sites at the summit area was 211 in total with the four observations during the inactive period (**Table 3.1**).

Since the minor eruptions in June 2015, the volcanic activity has been active until present (December 2016) (**Fig. 2.3**). Therefore, the data in 2012–2014 surveys represent inactive periods and those in 2015 and 2016 surveys (green broken lines in **Fig. 2.3**) can be treated as data of active periods. Since it was difficult to cover the study area with the two surveys of 2015 and 2016, they were focused on detecting possible changes of the diffuse degassing activity due to the volcanic activity changes. Therefore, the measurement sites (green diamonds and pink crosses in **Fig. 3.2** for 2015 and 2016 surveys, respectively) were mainly set around diffuse CO₂ flux anomalies in the

► **Table 3.1** Numbers of the measurement sites and gas samples in each survey

Date	Survey area		
	Summit	Flanks of Maekake	Jigokudani
<i>Soil CO₂ flux and soil temperature measurements</i>			
26 Oct. 2012	40	—	—
15 May 2013	64	—	—
27 May 2014	75	—	—
8 Oct. 2014	32	7	—
Total in inactive period	211	7	—
29 Oct. 2015	54	—	—
1 Aug. 2016	—	—	31
8 Aug. 2016	26	5	—
9 Aug. 2016	—	—	13
Total in active period	80	5	44
Total	291	12	44
<i>Soil gas sampling</i>			
1 Aug. 2016	—	—	15 ^a
8 Aug. 2016	21	1	—
9 Aug. 2016	—	—	3 ^a

^aOne of the samples is a bubbling gas sample collected in Jaborigawa river.

— not measured

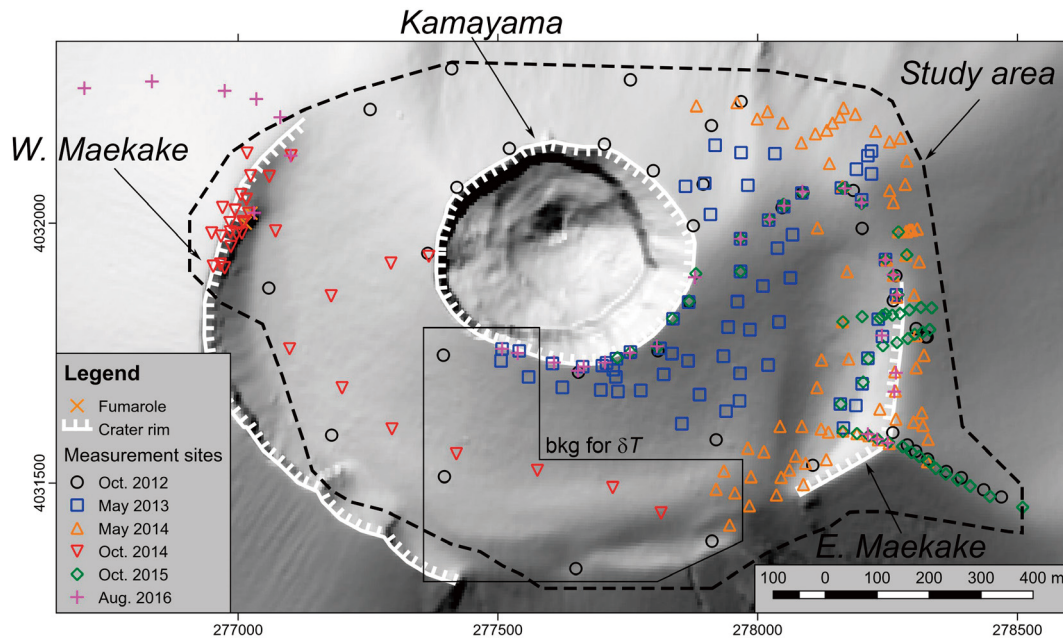


Fig. 3.2 Measurement sites in the summit area in all surveys [modified from Morita *et al.*, 2016]. The study area was set in the broken line with "Study area". Names of the crater rims ("Kamayama", "W. Maekake", and "E. Maekake") are also shown. A region in the lines with "bkg for δT " corresponds to the area for the calculation of the background temperature in 2012–2014 (see text). Coordinates are shown in meter of easting and northing (WGS84, UTM Zone 54 North). A digital elevation model (5-m grid) is provided by the Geospatial Information Authority of Japan.

eastern side of the study area found by the 2012–2014 surveys (**Fig. 3.2**). Total of 80 measurements were made with the 2015 and 2016 surveys (**Table 3.1**), corresponding to the active period. In the 2016 survey, soil gas sampling for analysis of chemical and isotopic compositions was also conducted. A method of the sampling is explained in **Section 3.4**.

To check presence or absence of diffuse degassing activity outside the study area on the flanks of Maekake volcano, sets of measurements were made along mountain trails on the eastern and western flanks of Maekake volcano in October 2014 and August 2016, respectively. The number of the measurement sites in the flanks of Maekake volcano were 12 (**Table 3.1**). Two surveys were also made at Jigokudani fumarolic field, the only known fumarolic field in the peripheral areas of Asama volcano, to evaluate the diffuse CO₂ emission. Around Jigokudani fumarolic field, soil CO₂ flux and soil temperature measurements were conducted in August 2016 (**Table 3.1**, a rectangle with “Jigokudani” in **Fig. 3.1**). The number of the measurement sites was 44 (**Table 3.1**). Soil gas and bubbling gas sampling for analysis of chemical and isotopic compositions was also conducted.

3.2 Soil CO₂ flux and soil temperature measurements

Soil CO₂ flux was measured using accumulation chamber method [*Parkinson, 1981; Baubron et al., 1990; Chiodini et al., 1998*] with a portable diffuse flux meter (Westsystems Srl.). A chamber with a volume V and a surface A of $2.76 \times 10^{-3} \text{ m}^3$ and $3.14 \times 10^{-2} \text{ m}^2$, respectively, was set on the ground properly to avoid a contamination of atmospheric air from gaps between the chamber and the ground. Gas in the chamber was mixed with a fan and it was extracted continuously by a pump to a non-dispersive infrared analyzer (LI-820, LI-COR Inc.). Then, the gas in the analyzer was circulated back to the chamber. A CO₂ concentration detected by the analyzer was displayed against time in a PDA (personal digital assistant). An initial slope of the CO₂-time plot (S_{CO_2} in ppm s⁻¹) was evaluated in the field, and soil CO₂ flux (F_{CO_2} in g m⁻² day⁻¹) was calculated from the slope following an equation below [*Chiodini et al., 1998*]:

$$F_{\text{CO}_2} = \frac{86400 \times 44P}{10^6 RT} \frac{V}{A} S_{\text{CO}_2} \quad (3.1)$$

where P is an air pressure in hPa, T is an air temperature in K, and R is a gas constant ($8.31451 \text{ J K}^{-1} \text{ mol}^{-1}$). A measuring range of the analyzer was 0–20,000 ppm. Accuracy of concentration reading is 3 % and RMS noise for 1 s is less than 1 ppm at 370 ppm according to the manual of the flux meter by Westsystems Srl (available on the website at http://www.westsystems.com/doc/Brochure_Fluxmeter_2010.pdf). The reported accuracy of soil CO₂ flux was $\pm 25 \%$ for 0–22 g m⁻² day⁻¹, $\pm 15 \%$ for 22–44 g m⁻² day⁻¹, $\pm 10 \%$ for 44–6,600 g m⁻² day⁻¹, $\pm 10 \%$ for 6,600–13,200 g m⁻² day⁻¹, and $\pm 20 \%$ for 13,200–26,400 g m⁻² day⁻¹, respectively.

A typical effective measurement time in this study was about a minute at high flux sites ($>100 \text{ g m}^{-2} \text{ day}^{-1}$) and was about 90–120 s at low flux sites ($<10 \text{ g m}^{-2} \text{ day}^{-1}$). By investigating all the low flux data measured at the summit area, a typical detection limit of the CO₂ flux in this study was

evaluated to be $0.24 \text{ g m}^{-2} \text{ day}^{-1}$ corresponding to increase of 2 ppm in typical measurement time of 90 seconds. The detection limit of CO_2 flux using the same instrumentation usually ranges $0.05\text{--}0.5 \text{ g m}^{-2} \text{ day}^{-1}$ [e.g., *Chiodini et al.*, 2015; *Dionis et al.*, 2015a] and the value used in this study is within the range.

To confirm a presence of thermal anomalies corresponding to the diffuse CO_2 emission, soil temperatures at 15–30 cm depth were measured using a K-type thermocouple. The depth was 15–20 cm at many measurement sites. At each measurement site, the thermocouple was inserted into the ground before a start of the soil CO_2 flux measurement and the soil temperature was recorded at the end of the CO_2 flux measurement. A typical duration time for soil temperature measurement was about 3–5 minutes. The accuracy of soil temperature was $\pm 0.5 \text{ }^\circ\text{C}$ for the 2012 survey and $\pm 0.1 \text{ }^\circ\text{C}$ for the other surveys.

The observed soil temperature values were strongly influenced by the ambient temperature of the observation day, thus direct comparison of raw temperature values was difficult. To compare soil temperature values among different surveys during 2012–2014, the difference of the temperature from a mean background temperature in each observation (hereafter δT) was calculated and used for the comparison [*Chiodini et al.*, 2007b; *Sansivero et al.*, 2013; *Vilardo et al.*, 2015]. The mean background temperatures for the surveys in 2012–2014 were estimated using the measurement sites in a background region that was set in the southern flank of Kamayama cone (region with “bkg for δT ” in **Fig. 3.2**) where CO_2 flux values were negligible.

Coordinates of measurement sites were recorded using a handheld GPS (eTrex 30, Garmin International Inc.). An uncertainty of the GPS record was considered to be within $\pm 10 \text{ m}$. The coordinates of the measurement sites in this study are presented in Zone 54 North of Universal Transverse Mercator (UTM) projection with a WGS84 datum (EPSG code: 32654, <http://spatialreference.org/ref/epsg/wgs-84-utm-zone-54n/>).

3.3 Statistical treatment of soil CO_2 flux and soil temperature

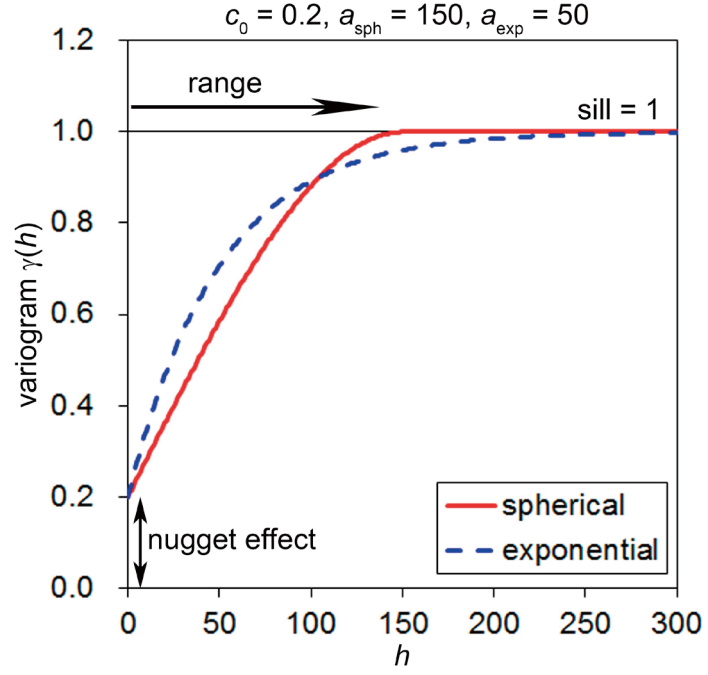
In this study at the summit area, six observations were conducted within four years. Data between 2012 and 2014 were observed during the inactive period (**Fig. 2.3**) and were aggregated as the dataset of inactive period for the following operations. The aggregated data were assumed to be representative of the diffuse CO_2 flux in the inactive period. During the four surveys between 2012 and 2014, seven measurement sites were revisited using GPS records to evaluate the flux difference for the same sites among the different surveys. Not every site was revisited in each round of observation. The relative standard deviations (RSD) of soil CO_2 flux values for the revisited sites were generally within 40 % except for two sites with RSDs of 80 % and 120 %. The

variations, especially for the two exceptions, are probably related to the repeatability of the GPS records (± 10 m) and to the local heterogeneity of soil CO₂ flux. Though the variations are slightly higher than the uncertainty of the CO₂ flux, the assumption that aggregation of the four different surveys yields appropriate representative results for the inactive periods of Asama volcano was considered to be effective in this study.

To reveal characteristics of the soil CO₂ flux data, statistical analysis based on the graphical statistical approach (GSA) was applied [Sinclair, 1974; Chiodini *et al.*, 1998]. This method is frequently used in geochemical exploration and soil CO₂ flux studies for choosing threshold values between anomalous and background geochemical data [Sinclair, 1974; Chiodini *et al.*, 1998]. The data of soil CO₂ flux values were plotted on a log-normal probability graph that had a probability (a cumulative frequency percent) on the x-axis and a CO₂ flux value in a logarithmic scale on the y-axis. Diffuse CO₂ is usually fed by multiple sources such as biological and volcano-hydrothermal [Cardellini *et al.*, 2003b]. This dual origin often results in a bimodal distribution of CO₂ flux values [Cardellini *et al.*, 2003b]. For each origin, CO₂ flux values often have a log-normal population that is represented as a straight line in the log-normal probability plot. The overlap of n log-normal populations results in a curve with $n - 1$ inflection points on the log-normal probability plot [Cardellini *et al.*, 2003b]. In this study, the inflection points of the soil CO₂ flux values on the log-normal probability plot were picked by visual evaluation following Sinclair [1974] and Cardellini *et al.* [2003b]. Then, straight lines were fitted for all populations by a linear least-squares method and statistical values (average, 5th and 95th percentiles) were derived from the fitted lines.

After the procedures of GSA method, spatial distribution maps were constructed with sequential Gaussian simulation (sGs) [Deutsch and Journel, 1998; Cardellini *et al.*, 2003b]. This method is often used in the studies of diffuse CO₂ emissions due to its advantages on an interpolation over parts of the study area where the measurement sites were not set and on an evaluation of the uncertainty of total soil CO₂ emissions [e.g., Cardellini *et al.*, 2003b; Padrón *et al.*, 2008, 2015; Dionis *et al.*, 2015a]. Because the sGs procedure needs a Gaussian distribution for an input data, the CO₂ flux values with a non-normal distribution were converted to normal scores using an open program by Dr. Ashton Shortridge in R software (available at <https://www.msu.edu/~ashton/research/code/nscore.R>). In the conversion, logarithmic CO₂ flux values were applied as the input data because the CO₂ flux values had a wide range in a small area. For the non-detectable flux value, the detection limit value ($0.24 \text{ g m}^{-2} \text{ day}^{-1}$) was used in the conversion. Secondly, empirical variograms for the normal score data were calculated using *variog* program in *geoR* package of R software [Diggle and Ribeiro Jr., 2007]. The empirical variogram is a variogram calculated from the sample data, and it represents a spatial variability as a function of a distance

►**Fig. 3.3** Variograms of spherical and exponential models. A case of $c_0 = 0.2$, $a_{\text{sph}} = 150$, and $a_{\text{exp}} = 50$ is shown. Values of a_{sph} and a_{exp} are selected so that a practical range value of the exponential model equals the range of the spherical model, see text for details.



between two sites in the study field, which is defined by the following equation [Diggle and Ribeiro Jr., 2007]:

$$\gamma(\mathbf{h}) = \frac{1}{2N(\mathbf{h})} \sum_{i=1}^{N(\mathbf{h})} [z(\mathbf{x}_i + \mathbf{h}) - z(\mathbf{x}_i)]^2 \quad (3.2)$$

where $N(\mathbf{h})$ is a number of pairs in a distance \mathbf{h} and $z(\mathbf{x}_i + \mathbf{h})$ and $z(\mathbf{x}_i)$ are input data values at \mathbf{x}_i and $\mathbf{x}_i + \mathbf{h}$. Then, the empirical variograms were fitted to spherical and exponential models by a non-linear least-square method using *variostat* program in *geoR* package of R software [Diggle and Ribeiro Jr., 2007]. In *geoR* package, each model is defined by the following equations:

$$\text{spherical} \quad \gamma(h) = \begin{cases} c_0 + (1 - c_0) \left[\frac{3}{2} \left(\frac{h}{a_{\text{sph}}} \right) - \frac{1}{2} \left(\frac{h}{a_{\text{sph}}} \right)^3 \right] & \text{if } h \leq a_{\text{sph}} \\ 1 & \text{if } h > a_{\text{sph}} \end{cases} \quad (3.3)$$

and

$$\text{exponential} \quad \gamma(h) = c_0 + (1 - c_0) \left[1 - \exp\left(-\frac{h}{a_{\text{exp}}}\right) \right] \quad (3.4)$$

where c_0 is a nugget effect and a_{sph} and a_{exp} are ranges for spherical and exponential models, respectively. Examples of the variogram models ($c_0 = 0.2$, $a_{\text{sph}} = 150$, $a_{\text{exp}} = 50$) are shown in **Fig. 3.3**. The nugget effect $c_0 = \gamma(0)$ corresponds to a discontinuity at the origin ($c_0 = 0.2$ in **Fig. 3.3**), which represents a randomness of the data values at $h = 0$. The range corresponds to a distance in which the difference between the variogram and a sill (= 1 for a normal distribution dataset) becomes negligible. In the definition of exponential model used in **Equation 3.4**, the distance

corresponding to the range of exponential model (a_{exp}) does not give a variogram value close to the sill. Thus, $3a_{\text{exp}}$ is used as the range for exponential model [e.g., *Cardellini et al.*, 2003b]. However, the *geoR* package uses a_{exp} as the range of exponential model in its definition (**Equation 3.4**), hence this study follows the definition of the *geoR* package and $3a_{\text{exp}}$ is called as a practical range of the exponential model. The sill is a limit of the variogram where h is sufficiently larger than the range, and the sill of the dataset with a normal distribution is one (**Fig. 3.3**). If h is larger than the range, $\gamma(h)$ of both models almost equals the sill (= 1), which indicates the data values from two sites at far distance are uncorrelated. For the further simulation, the best-fitted model from the two variogram models was chosen based on the least squares fitting to the empirical variograms.

After deciding the variogram model for the dataset, an ordinary kriging (OK) was applied to obtain a basic spatial distribution of the interpolated values used in the following simulations. The OK estimates the value $z_{\text{OK}}(\mathbf{x})$ at each new location \mathbf{x} in the field as a weighted linear combination of the sampled values [*Deutsch and Journel*, 1998; *Lewicki et al.*, 2005]:

$$z_{\text{OK}}(\mathbf{x}) = \sum_{i=1}^n w_i(\mathbf{x})z(\mathbf{x}_i) \quad (3.5)$$

where n is a number of the sampled sites and $z(\mathbf{x}_i)$ is a value of the i th sampled site \mathbf{x}_i . $w_i(\mathbf{x})$ is a weight for each sampled site. The weights are given by a system of linear equations [*Deutsch and Journel*, 1998; *Lewicki et al.*, 2005]:

$$\sum_{j=1}^n w_j(\mathbf{x})\gamma(\mathbf{x}_i - \mathbf{x}_j) + \lambda = \gamma(\mathbf{x}_i - \mathbf{x}), \quad i = 1, \dots, N(\mathbf{x}) \quad (3.6)$$

and

$$\sum_{j=1}^n w_j(\mathbf{x}) = 1 \quad (3.7)$$

where γ is the variogram model and λ is a Lagrange parameter. The estimation variance of OK $\sigma_{\text{OK}}^2(\mathbf{x})$ at location \mathbf{x} is also calculated as the following equation [*Deutsch and Journel*, 1998; *Lewicki et al.*, 2005]:

$$\sigma_{\text{OK}}^2(\mathbf{x}) = \sum_{i=1}^n w_i(\mathbf{x})\gamma(\mathbf{x}_i - \mathbf{x}) + \lambda \quad (3.8)$$

The spatial distribution interpolated by the kriging is a unique estimation and the local mean and the variance are estimated without specific regard to the resulting spatial statistics [*Deutsch and Journel*, 1998; *Cardellini et al.*, 2003b; *Lewicki et al.*, 2005]. On the contrary, sGs provides a set of equally probable realizations of the spatial distribution in which the global features and statistics of the sampled data are reproduced [*Deutsch and Journel*, 1998; *Cardellini et al.*, 2003b; *Lewicki et al.*, 2005]. This is an advantage of sGs to evaluate the spatial uncertainty and

the reason why sGs is often applied in the studies of diffuse CO₂ flux measurements at volcanoes. The sGs was applied for the data of this study using *predict.gsat* program in *gstat* package of R software [Pebesma, 2004]. In a procedure to obtain a single realization of sGs, a random value that had a probability with a Gaussian distribution function with a mean value of $z_{OK}(\mathbf{x})$ and a standard deviation of $\sigma_{OK}(\mathbf{x})$ was drawn as a “reasonable” value at location \mathbf{x} in the field. This value was added to the original data and was used to estimate the value at the next location. Then, at the next location, a random value was drawn in the same manner and this continued until the simulated values were obtained at all locations. A random path connecting a location to another one was applied in each realization. The number of the grid squares of the simulation in this study was 2,665 squared cells (20 m × 20 m) for the summit area due to the usable memory of the computer. The number of the realizations was 100 following Cardellini *et al.* [2003b]. Finally, the simulated normal scores were back-transformed to the logarithmic flux value. The average and standard deviation of logarithmic CO₂ flux values for 100 realizations were derived for all grids, and the spatial distribution of diffuse CO₂ flux values was expressed by plotting the average value at each grid. Multiplying the average CO₂ flux value at each grid by an area of each grid (400 m²) and summing up them for all grids, the total CO₂ emission rate was calculated for the 2012–2014 data. The standard deviation range of the total CO₂ emission was calculated by the same procedure replacing the average flux value by average ± standard deviation in logarithmic scale at each grid and considering the law of propagation of error in the summation. Operations for estimating δT distribution were the same as those for diffuse CO₂ flux values.

3.4 Soil gas sampling and laboratory analysis

To reveal origins of the diffuse CO₂, soil gases for chemical and isotopic analysis were collected at selected measurement sites in the 2016 survey. Gases at 30–40 cm depth were sampled with a 60 mL syringe (Terumo Corp.) using a 50-cm long commercial stainless probe inserted in the ground [Notsu *et al.*, 2006] and were drawn into a 12 mL glass vial (Labco Ltd.) [Dionis *et al.*, 2015b]. At each site, 4 or 5 samples were collected for subsequent analyses. At Jigokudani fumarolic field, bubbling gases from the bottom of Jaborigawa river were also sampled in the vials by putting the vial upside down in the river water on the bubbling area. The glass vial for the gas sampling was sealed with a butyl rubber septum. According to the previous studies, loss of CO₂ through the rubber septum is negligible [Tu *et al.*, 2001; Chiodini *et al.*, 2008; Robertson *et al.*, 2016], and chemical as well as isotopic compositions of gas samples were preserved at least one month using the vials [Robertson *et al.*, 2016]. Subsequent analyses of this study were made within eight weeks from the sampling. Thus, significant changes of gas concentrations or carbon

isotopic values of the samples are not expected.

Soil gas composition was analyzed at Instituto Tecnológico y de Energías Renovables (ITER), Tenerife, Canary Islands. To evaluate the CO₂ concentrations and the degree of air contamination in gas samples, gas concentrations of O₂, N₂, and CO₂ were analyzed by a Varian CP-490 (Varian Medical Systems Inc.) micro gas chromatography (micro-GC) with a thermal conductivity detector (TCD) and a carrier gas of argon. The accuracy of the concentrations is about 2.5 % following the previous works by *Dionis et al.* [2015a, 2015b].

Carbon isotope ratio (¹³C/¹²C) of CO₂ in a soil gas sample was analyzed with a Thermo Finnigan MAT 253 (Thermo Fisher Scientific Inc.) continuous-flow isotope ratio mass spectrometer (IRMS) connected with a continuous flow injector of a Finnigan GasBench II (Thermo Fisher Scientific Inc.) at ITER. The ¹³C/¹²C ratio is given as δ¹³C value (unit: ‰) in the following definition:

$$\delta^{13}\text{C} = \left[\frac{(^{13}\text{C}/^{12}\text{C})_{\text{Sample}}}{(^{13}\text{C}/^{12}\text{C})_{\text{Standard}}} - 1 \right] \times 1000 \quad (3.9)$$

where (¹³C/¹²C)_{Sample} and (¹³C/¹²C)_{Standard} are the carbon isotope ratios for a sample and a standard material, respectively. As a standard sample for carbon, Vienna Pee Dee Belemnite (VPDB) was used, which has the ¹³C/¹²C ratio of 11,237.2±2.9.

Chapter 4

Results

4.1 Soil CO₂ flux and soil temperature at the summit area in 2012–2014

Soil CO₂ flux values in 2012–2014 at the summit area (211 in total dataset, **Appendix A.1**) ranged from a non-detectable value to 478 g m⁻² day⁻¹ with an average value of 66.8 g m⁻² day⁻¹ (**Table 4.1**). In total dataset, 48 of 211 sites (22.9 %) were below the detection limit. A log-normal probability plot of soil CO₂ flux by GSA method is depicted in **Fig. 4.1** and the mean and 5th–95th percentiles of the derived populations are summarized in **Table 4.2**. The resulting probability plot allowed a separation of the soil CO₂ flux values into three populations: (A) the peak population (17.5 % of the dataset) with an average value of 195.5 g m⁻² day⁻¹, (B) the intermediate population (45.0 % of the dataset) with an average value of 19.1 g m⁻² day⁻¹, and (C) the background population (14.6 % of the dataset) with an average value of 0.97 g m⁻² day⁻¹.

In many cases of diffuse CO₂ flux measurements, the population in a probability plot consists of combinations of a peak population, a background population, and an intermediate mixture of the peak and background populations. The peak and background populations are interpreted, respectively, as being supplied from deep volcano-hydrothermal and surface biogenic origins [*Chiodini et al.*, 1998, 2008; *Camarda et al.*, 2007; *Granieri et al.*, 2014]. In the probability plot of this study (**Fig. 4.1**), the average value of Population C (the background population) was 0.97 g m⁻² day⁻¹, which is much lower than CO₂ flux values derived from ground with vegetation (several tens of grams per square meters per day) [*Chiodini et al.*, 2008]. The value of the background population is in agreement with the negligible vegetation of the study area and probably means that contribution of the biogenic source is very limited in the study area. The average value of the peak population (Population A) was 195.5 g m⁻² day⁻¹, which is one or two order of magnitude lower than those from ground near fumaroles [e.g., *Chiodini et al.*, 2008] or those from enormous diffuse degassing areas like Etna volcano [*Giammanco et al.*, 2016]. This population can be considered as representative of volcano-hydrothermal CO₂ source [*Chiodini et al.*, 1998, 2008; *Cardellini et al.*, 2003b]. The intermediate population (Population B) can be interpreted as a mixture of Populations A and C.

The soil CO₂ flux values were plotted on a map of the summit area (**Fig. 4.2a**). CO₂ flux values in the range of Population A (circles in **Fig. 4.2a**) were obtained only in the eastern side of the study area. These high CO₂ flux values were surrounded by lower CO₂ flux values in the

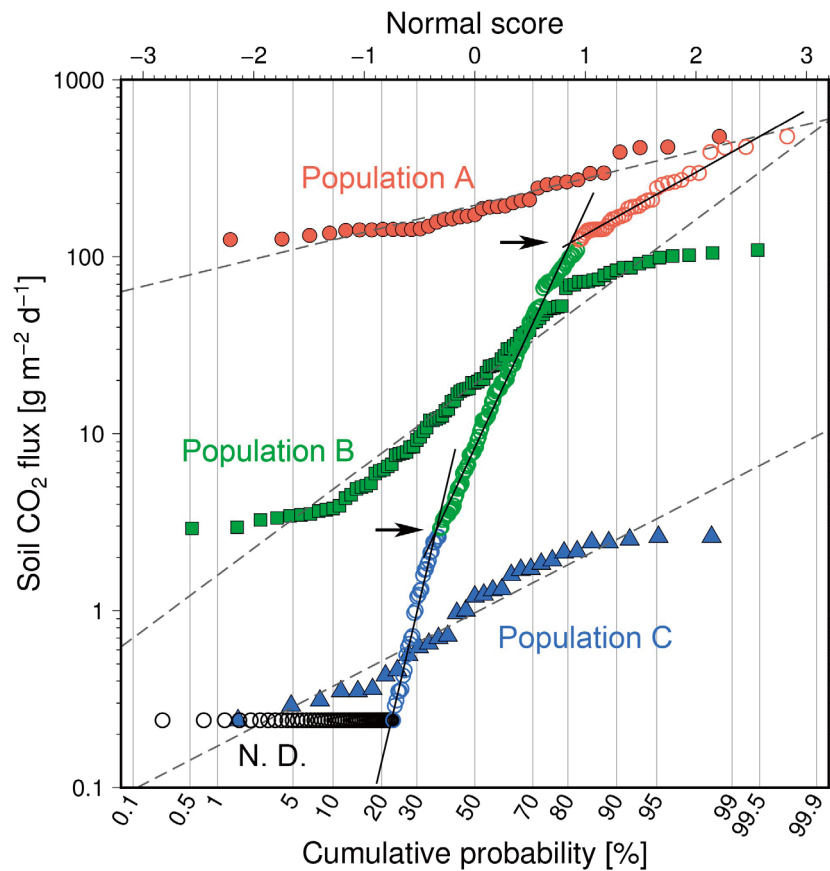
Table 4.1 Summary of the observations in the summit area [modified from Morita *et al.*, 2016]

Date	No. of sites	Soil CO ₂ flux [g m ⁻² day ⁻¹]					No. of n.d.	No. of sites	Soil temperature [°C]				Bkg. for δT
		Min.	Median	Mean	Max.	Min.			Median	Mean	Max.		
26 Oct. 2012	40	1.19	42.6	68.6	296	11	40	4	8.9	8.6	15	8.3	
15 May 2013	64	0.62	49.6	92.4	414	11	63	11.0	18.3	18.0	29.1	16.7	
27 May 2014	75	0.72	24.2	68.0	478	18	70	6.7	11.5	12.2	44.6	9.7	
8 Oct. 2014	32	0.24	1.6	4.84	20.4	8	32	5.7	8.3	9.1	28.0	7.9	
Total (2012–2014)	211	0.24	20.4	66.8	478	48	205	4	11.5	12.8	44.6	—	
29 Oct. 2015	54	0.47	140	180	623	4	54	6.1	10.3	10.5	18.8	10.0	
8 Aug. 2016	26	0.27	94.9	519	6,640	0	23	19.4	22.2	22.1	24.9	20.0	
Total (2015–2016)	80	0.27	129	296	6,640	4	77	6.1	11.5	14.0	24.9	—	

Maximum, mean, median, and minimum values of soil CO₂ flux exclude non-detectable values.

n.d. non-detectable, *bkg.* background for δT , — not defined

►**Fig. 4.1** A log-normal probability plot for soil CO₂ flux values of the summit area in 2012–2014 [modified from Morita *et al.*, 2016]. Soil CO₂ flux values are plotted against the cumulative probability of the total data (open circles). Non-detectable values ("N. D.") are plotted with the detection limit value. Red, green, and blue symbols, respectively, denote the cumulative probabilities in Populations A, B, and C. Solid and broken lines are regression lines for the populations. Arrows show inflection points of the total data.



ranges of Populations B and C (squares and triangles in **Fig. 4.2a**, respectively). Inside the high CO₂ flux values of Population A, CO₂ flux values as low as the range of Population C were found. In contrast, in the western side of the study area, CO₂ flux values were basically in the range of Population C and those in the range of Population B were obtained only along the northern part of western Maekake crater wall where very weak fumaroles exist (orange crosses in **Fig. 4.2a**). At the other northern, southern, and western parts of the study area, low flux values only in the range of

► **Table 4.2** Summary of the probability plots for soil CO₂ flux values in the summit area [Morita et al., 2016]

Population	Probability [%]	Mean [g m ⁻² day ⁻¹]	5-95 % percentiles [g m ⁻² day ⁻¹]
A	17.5	195.5	109.7–348.3
B	45.0	19.1	3.29–111.1
C	14.6	0.97	0.29–3.30
N.D.	22.9	—	—

N.D. non-detectable, — not defined

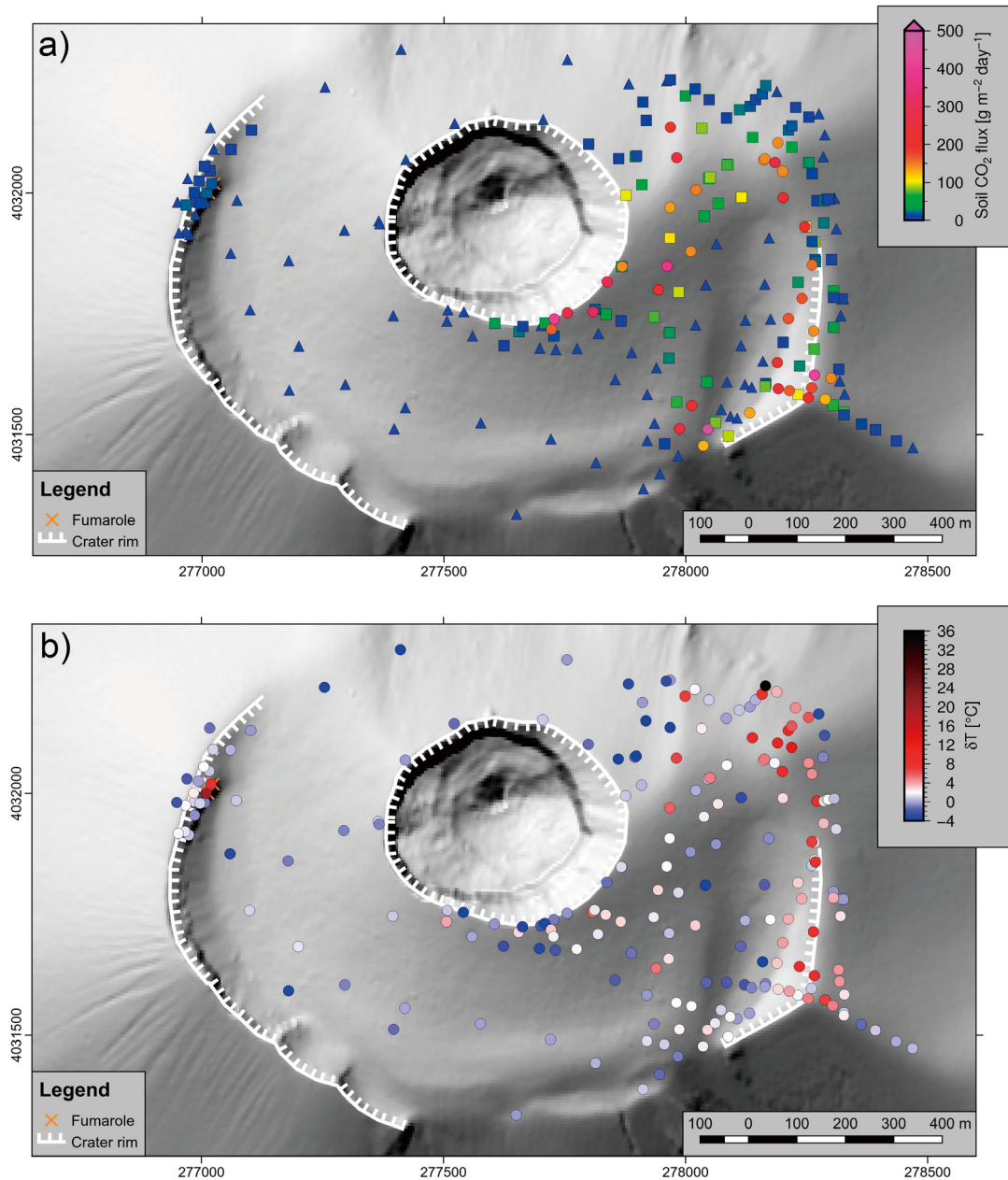


Fig. 4.2 a Soil CO₂ flux and b ΔT values of the summit area in 2012–2014. In a, circle, square, and triangle symbols correspond to CO₂ flux values in Populations A, B, and C in Fig. 4.1. Coordinates are shown in meter of easting and northing (WGS84, UTM Zone 54 North). A digital elevation model (5-m grid) is provided by the Geospatial Information Authority of Japan.

Population C were obtained. The sites with CO₂ flux values in the range of Population A were only found in the eastern side of the study area.

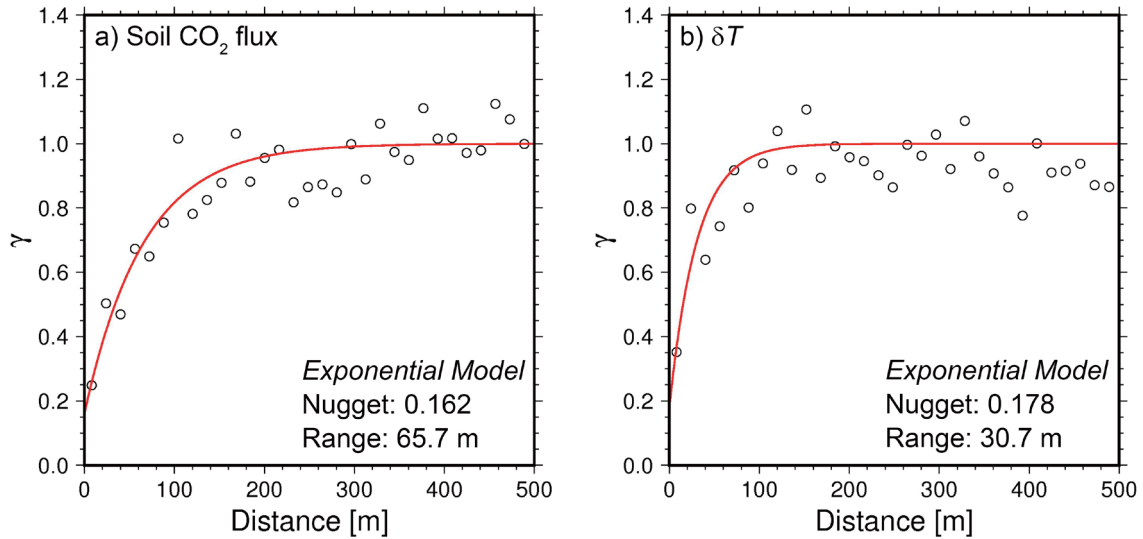


Fig. 4.3 Empirical variograms (black circle) for the distance up to 500 m and the best-fit variogram model used in the simulations (red line) for **a** soil CO₂ flux and **b** δT values of the summit area in 2012–2014 [modified from *Morita et al.*, 2016]

An empirical variogram for the soil CO₂ flux values in 2012–2014 was plotted for the distance below 500 m, at which the empirical variograms have already become almost one, in **Fig. 4.3a**. Then, variogram models were fitted and the best-fit model using an exponential variogram model was derived (**Fig. 4.3a**). The nugget effect and range values were respectively 0.162 and 65.7 m (**Fig. 4.3a**). As illustrated in **Fig. 4.3a**, the model values correspond reasonably well with the empirical variograms in the distance below 500 m, especially below 197 m that is the practical range of the exponential model.

A hundred simulations of sGs were performed to reveal the spatial distribution of soil CO₂ flux and to evaluate the total CO₂ emission from the study area. An averaged soil CO₂ flux value at each grid of 100 realizations is shown in **Fig. 4.4a**. High CO₂ flux values in the range of Population A were obtained only in the eastern side of the study area as expected from **Fig. 4.2a**. In this high-flux area, a high-flux zone surrounding a low-flux zone like an elliptical ring elongated to N–S is clearly visible. The outer and inner sizes of the elliptical ring were about 700 m \times 400 m and about 300 m \times 150 m in N–S and in E–W, respectively. By multiplying the average CO₂ flux value and an area of each grid and summing the products of all the grids in the study area, a total diffuse CO₂ emission rate from the study area (1.066 km²) was calculated to be 12.6 t day⁻¹ with a standard deviation range of 12.2–14.6 t day⁻¹ [*Morita et al.*, 2016].

To identify the DDS of the study area more clearly, a probability map from 100 realizations of sGs was prepared (**Fig. 4.5**). This map shows a probability that the simulated CO₂ flux value of each grid is above a cutoff value and is used for defining the extent of the DDS [*Cardellini et al.*, 2003b; *Chiodini et al.*, 2008]. As the cutoff value, *Chiodini et al.* [2008] used the average flux value

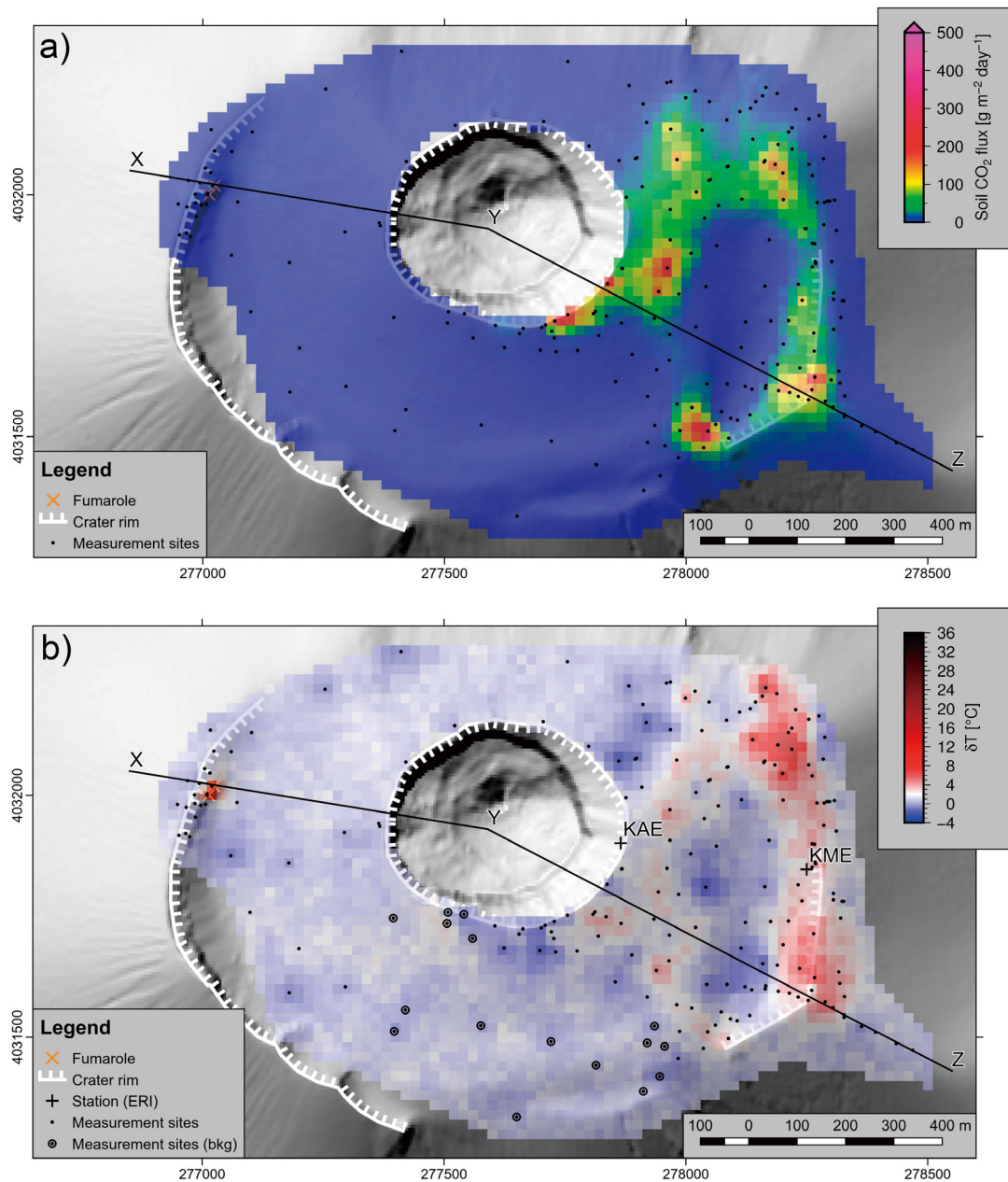


Fig. 4.4 **a** Soil CO₂ flux and **b** δT values of the summit area in 2012–2014 obtained by 100 realizations of the simulations [modified from *Morita et al.*, 2016]. Measurement sites with the symbol of a bullet with a circle in **b** (“Measurement sites (bkg)”) correspond to the sites used as background for the δT calculation (see text). A line with “X”, “Y”, and “Z” corresponds to the transection in **Fig. 4.9**. Names of the observation stations of ERI are shown (“KAE” and “KME”). Coordinates are shown in meter of easting and northing (WGS84, UTM Zone 54 North). A digital elevation model (5-m grid) is provided by the Geospatial Information Authority of Japan.

of the intermediate population in the log-normal probability plot and showed that it was realistic. Following this result, the cutoff value in this study was set to 19.1 g m⁻² day⁻¹ that was the average value of Population B. The DDS is defined as grids with a probability larger than 50 % (yellow to red colors in **Fig. 4.5**). In **Fig. 4.5**, the DDS was found only in the eastern side of the study area and it corresponds to the elliptical ring of high CO₂ flux depicted in **Fig. 4.4a**. In the western part of

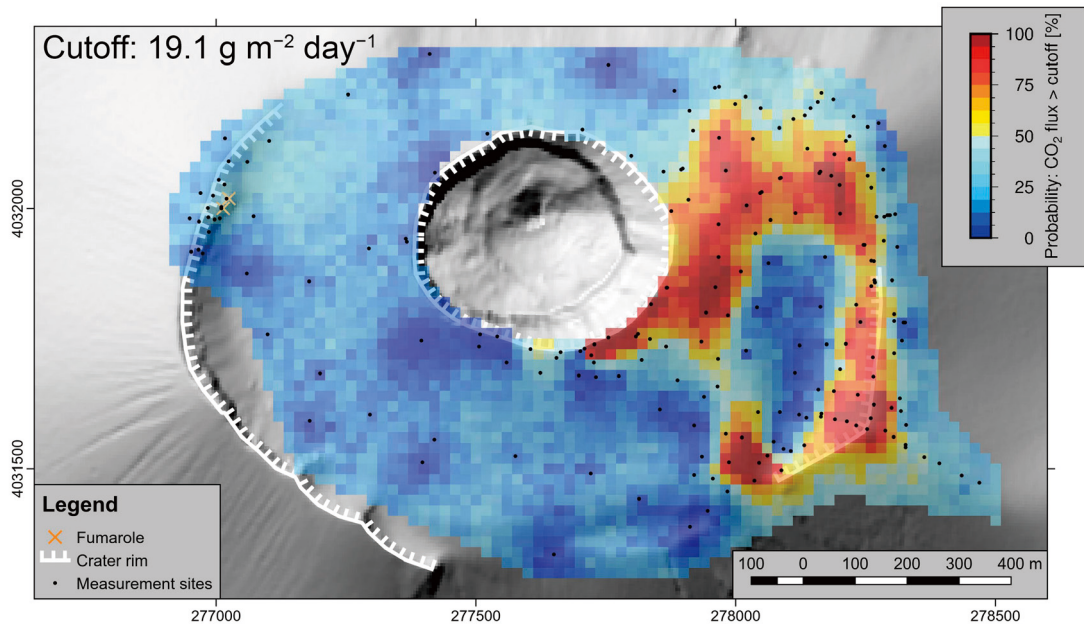


Fig. 4.5 A probability map for soil CO₂ flux with a cutoff value of 19.1 g m⁻² day⁻¹. A grid with a probability larger than 50 % is shown with yellow to red colors. Coordinates are shown in meter of easting and northing (WGS84, UTM Zone 54 North). A digital elevation model (5-m grid) is provided by the Geospatial Information Authority of Japan.

the ring along Kamayama crater and the northern part of the ring, the DDS seems to extend to the outer field for about one or two hundred meters but it fits within the study area.

Soil temperature values in 2012–2014 at the summit area (205 in total dataset, **Appendix A.1**) ranged from 4 to 44.6 °C with an average value of 12.8 °C (**Table 4.1**). As illustrated in **Table 4.1**, mean and median values measured in May were larger than those measured in October mainly due to an air temperature difference. This result suggests that the measured soil temperatures could be affected by seasonal difference. Therefore, the difference of the temperature from a mean background temperature in each observation (δT) was calculated as explained in **Section 3.2**. Mean background temperature values calculated from the background flux region set in the southern flank of Kamayama cone are listed in **Table 4.1**.

The calculated δT values were plotted on a map of the summit area (**Fig. 4.2b**). High δT values (>6 °C) were obtained along Maekake crater rim in the eastern side of the study area and around the weak fumaroles in western Maekake crater wall. Relatively high δT values (2–6 °C) were obtained around these areas and also on the slopes of Kamayama cone in the eastern side of the study area. The highest δT value (34.9 °C) was derived at the northern edge of the study area. At this site, a dark red brown oxidized rock unit was exposed to the ground surface, while the other area was mainly covered with pyroclastic rocks ejected by vulcanian eruptions. This unit corresponds to welded pyroclastic materials in the 1783 plinian eruption [*Yasui and Koyaguchi,*

1998, 2004]. The high δT values on the western Maekake crater wall are related to the weak steam emissions. The temperature of the steam at the vent was 48.0 °C in the October 2014 survey and it was in the range of the steam temperature (36–53 °C) measured during 1933–1937 [Noguchi, 1938b]. Inside the high δT values in the eastern side and at the other northern, southern, and western parts of the study area, only low δT values (<2 °C) were obtained.

An empirical variogram for the δT values in 2012–2014 was plotted for the distance below 500 m, at which the empirical variograms have already become almost one, in **Fig. 4.3b**. Then, variogram models were fitted and the best-fit model using an exponential variogram model was derived (**Fig. 4.3b**). The nugget effect and range values were respectively 0.178 and 30.7 m (**Fig. 4.3b**). As illustrated in **Fig. 4.3b**, the model values correspond reasonably well with the empirical variograms in the distance below 500 m, especially below 92 m that is the practical range of the exponential model.

A hundred simulations of sGs were performed to reveal the spatial distribution of δT values. An averaged δT value at each grid of 100 realizations is shown in **Fig. 4.4b**. High δT values (>6 °C) were obtained along Maekake crater rim in the eastern side of the study area and around the weak fumaroles in western Maekake crater wall (**Fig. 4.4b**). In the high- δT area in the eastern side, a high- δT zone surrounded a low- δT zone (<2 °C) like an elliptical ring elongated to N–S (**Fig. 4.4b**). This characteristic is similar to the soil CO₂ flux anomalies but the high- δT anomalies in the eastern flank of Kamayama cone is relatively weaker than those in the eastern Maekake crater rim. The elliptical ring of the high- δT anomalies stretched to the northern edge of the study area where the highest δT value was obtained (**Fig. 4.4b**). In this area, soil CO₂ flux values was not high (**Fig. 4.4a**) and this is different from other high- δT anomalies. Around the weak fumaroles in western Maekake crater wall, the δT value was high (**Fig. 4.4b**) but the soil CO₂ flux value was low (**Fig. 4.4a**). This is also the difference of spatial distributions between soil CO₂ flux and δT values. In the other northern, southern, and western parts of the study area, low δT (<2 °C) values were obtained. Although there are some differences between the distributions of soil CO₂ flux and δT anomalies as pointed above, overall distributions of them are similar, which probably suggests that CO₂ and heat are ascending together.

Six examples of realizations of soil CO₂ flux values out of the 100 realizations are randomly selected to see the variability of the 100 realizations (**Fig. 4.6**). Although individual realizations have large difference between each other in **Fig. 4.6**, there are some common characteristics in the realizations. In all realizations shown in **Fig. 4.6**, the elliptical-ring shape of the high soil CO₂ flux values can be clearly recognized in the eastern side of the study area even though the extent of the ring is variable in each realization. In the western, northern, and southern parts of the study

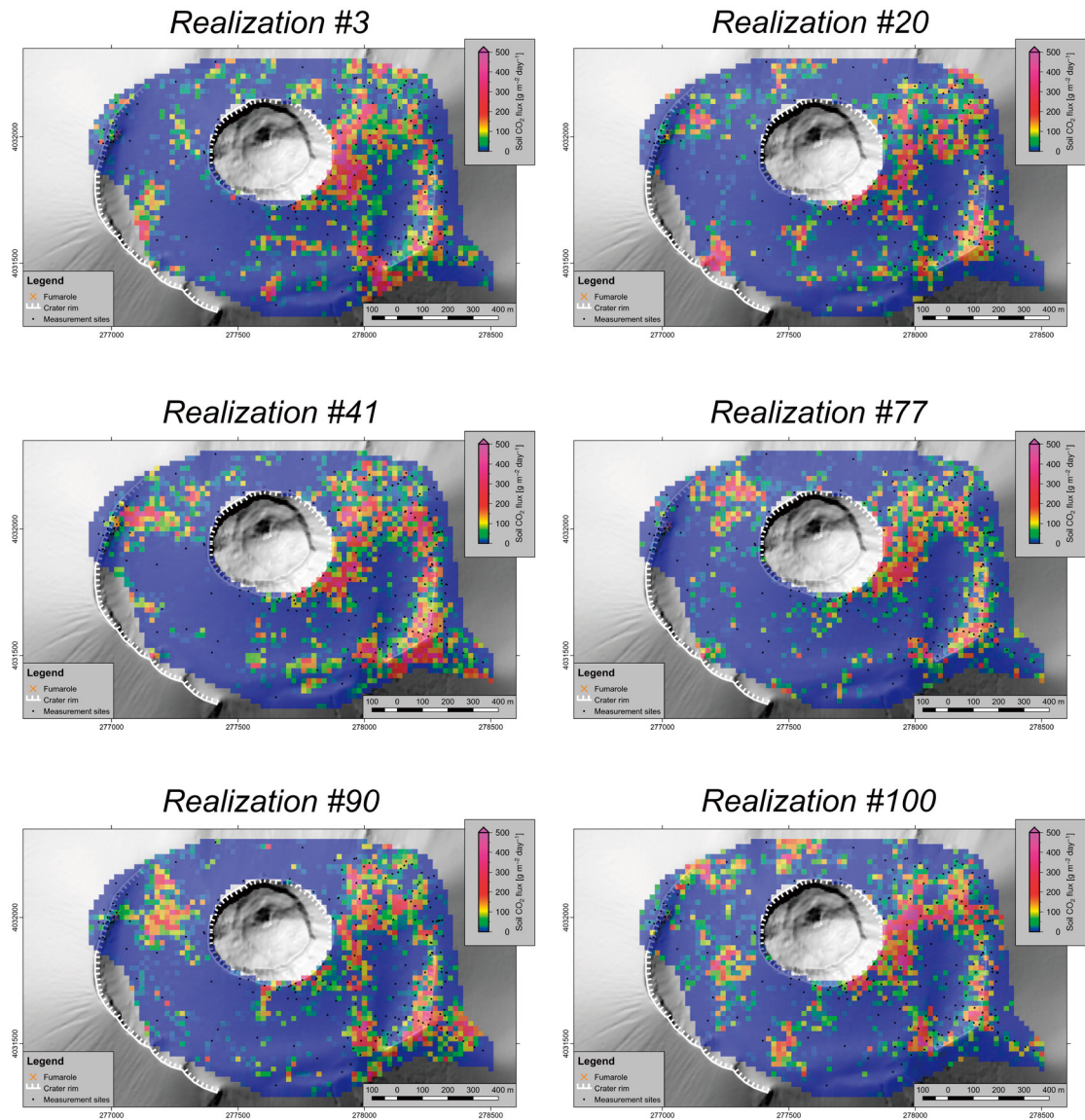


Fig. 4.6 Six randomly selected examples of the 100 realizations of sGs for soil CO₂ flux values in the summit area during 2012–2014. Coordinates are shown in meter of easting and northing (WGS84, UTM Zone 54 North). A digital elevation model (5-m grid) is provided by the Geospatial Information Authority of Japan.

area, the soil CO₂ flux values are generally in the background range. However, some patches of high soil CO₂ flux values appear in respective realizations in the western, northern, and southern parts. The locations and the soil CO₂ flux values of these patches are very different between each realization and are not common characteristics. The characteristics of the realizations mentioned above are not only applicable to the six realizations in **Fig. 4.6** but also applicable to the rest of the 100 realizations. In the sGs, all the obtained realizations are considered equiprobable [Deutsch and Journel, 1998], thus the DDS found as the elliptical ring in the eastern side of the study area is very likely to exist and reliable. In the other part of the study area, the patches appeared in respective realizations. This is probably related to the distances between the measurement sites in these

areas, which were near the practical range of the variogram model used in the simulations. Thus, the existence of small scale DDS at these parts cannot be completely denied, but, considering the averaged values of the realizations were in the range of the background population (**Fig. 4.4a**), the presence of the DDS in the western side of the study area is likely low.

To evaluate the shape and extent of the DDS with the elliptical-ring shape in the eastern side of the study area (**Fig. 4.5**), the probability map from 100 realizations using lower cutoff value is shown in **Fig. 4.7a**. The cutoff value was set at $1.9 \text{ g m}^{-2} \text{ day}^{-1}$ that is 2 times higher than the average value of the background population (**Fig. 4.1**) following *Cardellini et al.* [2003b]. With this cutoff value, even a small increase from the background level is counted as the CO_2 flux level of DDS. In **Fig. 4.7a**, the DDS with probabilities larger than 50 % (yellow to red colors) was obtained as the elliptical ring in the eastern side and was also found near Maekake crater wall in the northwestern part of the study area. Although the elliptical ring in **Fig. 4.7a** is wider (about 100 m) than that in **Fig. 4.5**, both shapes of the DDS in **Figs. 4.5** and **4.7a** are quite similar. Although the northern and southern parts of the elliptical DDS slightly reach the northern and southern edges of the study area, the eastern side of the DDS is confined in the study area. Hence, the shape and extent of the DDS with the elliptical-ring shape in the eastern side of the study area does not significantly change with the two cutoff values and is reliable. This probably implies that measurement sites distribution for the eastern side of the study area in 2012–2014 surveys were adequate for grasp the characteristics of the DDS. For the northwestern side of the study area, the DDS was found in **Fig. 4.7a** but not in **Fig. 4.5**. This area may have slightly higher values compared to the background level, but the DDS in **Fig. 4.7a** can be probably explained by some extensions of the soil CO_2 flux values of the western Maekake crater wall due to sparse measurement sites of the area.

A probability map from 100 realizations of δT values is also shown in **Fig. 4.7b**. The cutoff value was set to $4 \text{ }^\circ\text{C}$ that is an intermediate value of δT anomalies in **Fig. 4.4b**. In **Fig. 4.7b**, grids with probabilities larger than 50 % (yellow to red colors) were found along Maekake crater rim in the eastern side and in the northwestern part of the study area. These areas are probably regarded as the areas with heat anomalies as discussed earlier. The elliptical ring was also observable in **Fig. 4.7b** but do not have higher probabilities over 50 % for the most part. This might be related to the selection of the background temperature for the δT calculation and/or low heat anomalies of the summit area.

4.2 Soil CO_2 flux and soil temperature at the summit area in 2015 and 2016

Soil CO_2 flux values at the summit area in 2015 and 2016 (respectively 54 and 26 in total

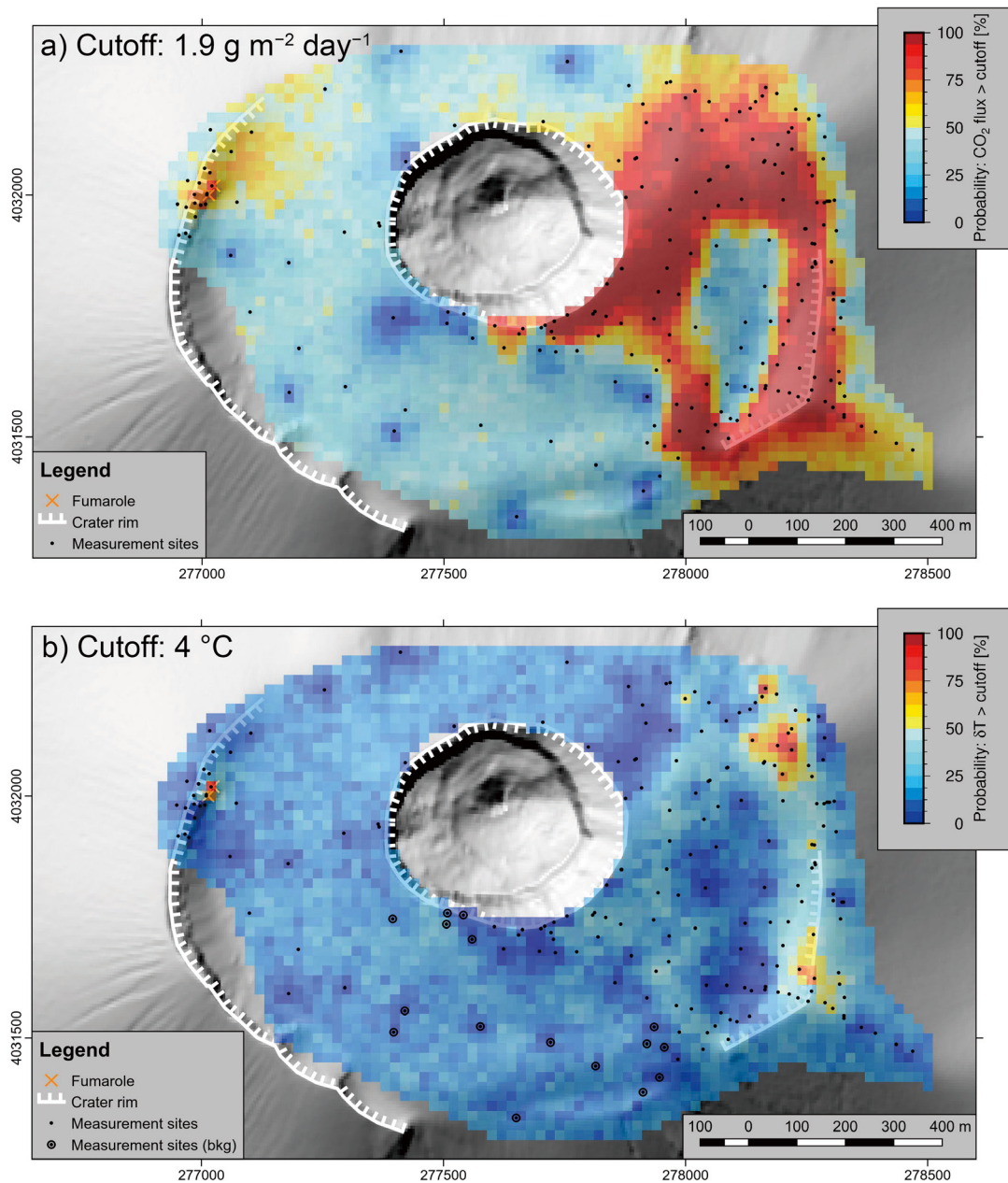


Fig. 4.7 Probability map for **a** soil CO_2 flux values with a cutoff value of $19.1 \text{ g m}^{-2} \text{ day}^{-1}$ and **b** δT values with a cutoff value of $4 \text{ }^\circ\text{C}$. A grid with a probability larger than 50 % is shown with yellow to red colors. Coordinates are shown in meter of easting and northing (WGS84, UTM Zone 54 North). A digital elevation model (5-m grid) is provided by the Geospatial Information Authority of Japan.

dataset, **Appendix A.2**) ranged below a non-detectable value to 620 and $6,640 \text{ g m}^{-2} \text{ day}^{-1}$ with an average value of 180 and $519 \text{ g m}^{-2} \text{ day}^{-1}$, respectively (**Table 4.1**). For the 2015 and 2016 data, 4 of 54 sites (7.4 %) and no sites were below the detection limit, respectively, because the measurement sites were mainly set in the areas of high CO_2 flux anomalies in the eastern side of the study area. The maximum CO_2 flux in 2015 was slightly higher than that in 2012–2014 and that in 2016 was extremely higher than that in 2012–2014. Considering that the seismicity and plume SO_2 flux have intensified since the 2015 eruption (**Fig. 2.3**), this increase of soil CO_2 flux is perhaps related to the

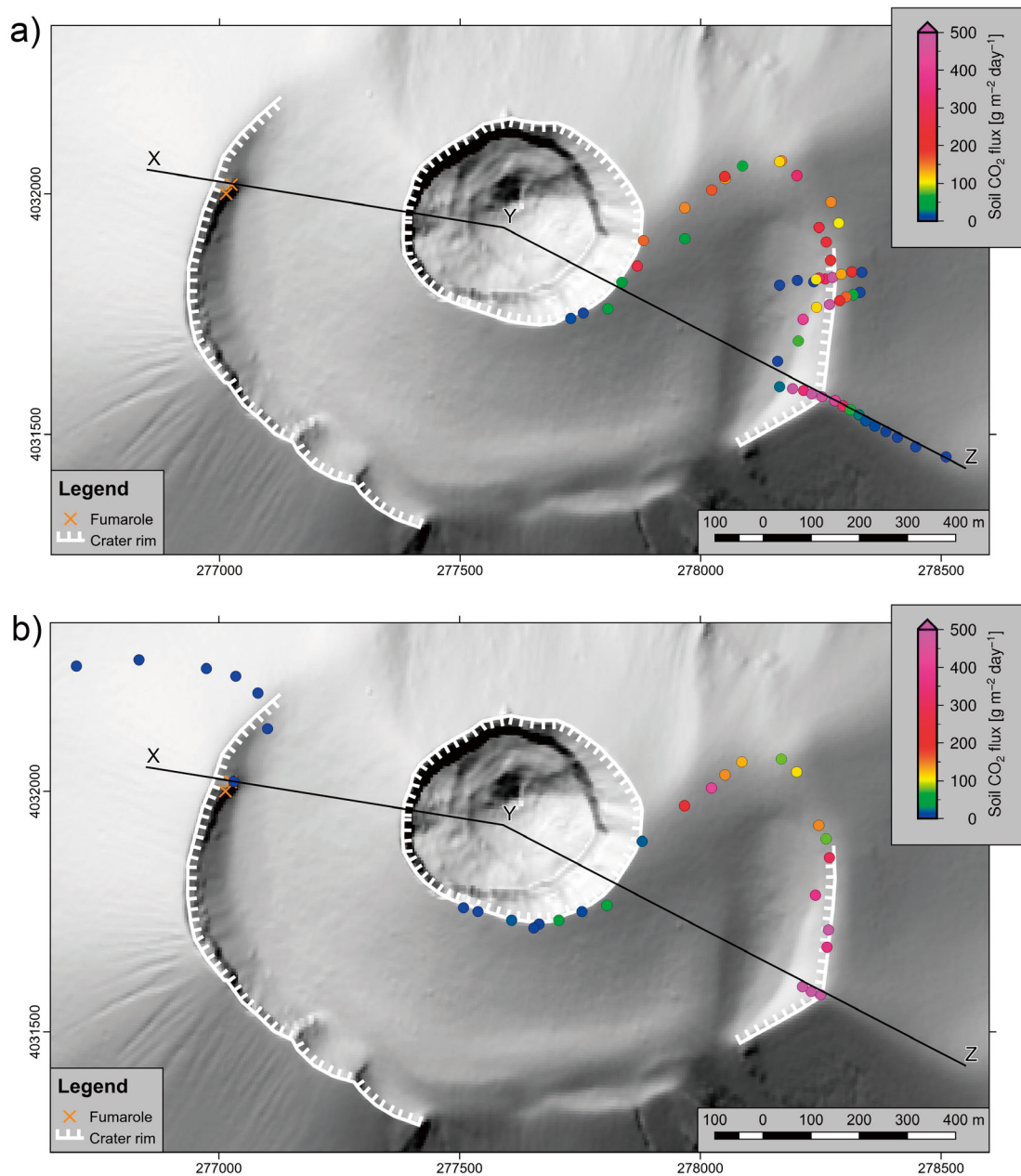
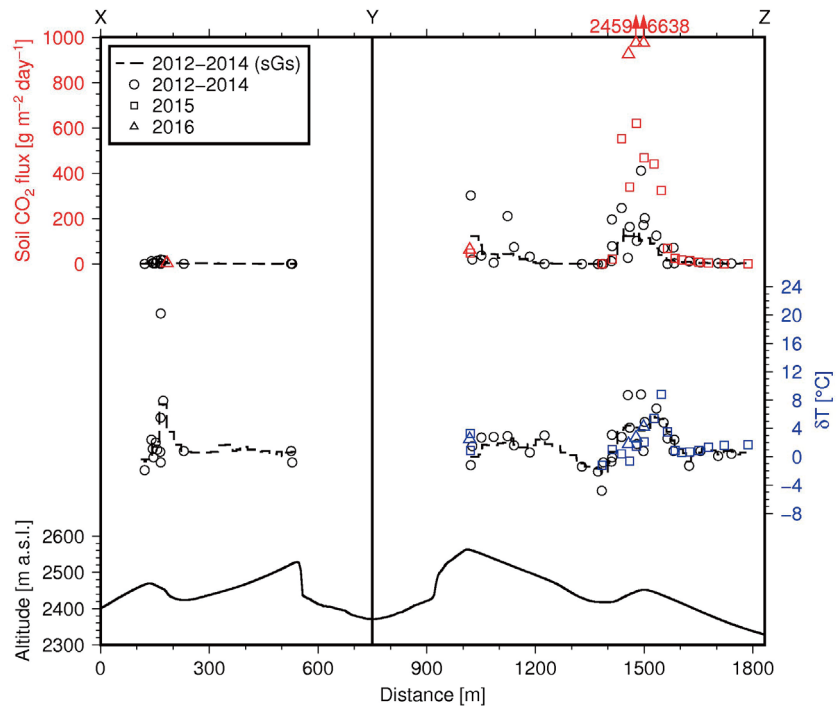


Fig. 4.8 Soil CO₂ flux values of the summit area in **a** 2015 and **b** 2016. A line with "X", "Y", and "Z" corresponds to the transection in **Fig. 4.9**. Coordinates are shown in meter of easting and northing (WGS84, UTM Zone 54 North). A digital elevation model (5-m grid) is provided by the Geospatial Information Authority of Japan.

activity changes of Asama volcano. While the plume SO₂ flux values in 2015 are generally higher than those in 2016 (**Fig. 2.3**), the maximum soil CO₂ flux value in 2015 is one order of magnitude smaller than that in 2016. This perhaps indicates that the diffuse degassing activity during the 2015 survey was weaker than that during the 2016 survey, however it is impossible to conclude the difference by the limited number of dataset.

Spatial distributions of soil CO₂ flux values in 2015 and 2016 are shown in **Figs. 4.8a** and **4.8b**, respectively. Along the elliptical ring of high CO₂ flux anomalies detected in 2012–2014, soil

►**Fig. 4.9** Profiles of soil CO₂ flux and δT values in E-W transection of 2012–2014 [modified from *Morita et al.*, 2016], 2015, and 2016. Transection is along the line (“X–Y–Z”) of **Figs. 4.4** and **4.8**. Altitude along the transection is also shown. A digital elevation model (5-m grid) is provided by the Geospatial Information Authority of Japan.



CO₂ flux values of 2015 and 2016 retained high CO₂ flux values. At least for the eastern Maekake crater area in 2015, low CO₂ flux values were obtained for the locations inside and outside the ring-shape DDS in the inactive period. Thus, the extent of the DDS at least for the eastern Maekake crater did not change significantly between the inactive and the active periods.

To see changes of soil CO₂ flux values from the inactive period of the volcanic activity to the active period, the values along E–W transection (“X–Y–Z”) in **Figs. 4.4** and **4.8** are plotted in **Fig. 4.9**. In **Fig. 4.9**, the 2012–2014, 2015, and 2016 data of the measurement sites within 50 m from the transection line are respectively plotted with circles, squares, and triangles, and the average values of the sGs realizations (**Fig. 4.4a**) along the transection are plotted with broken lines. Soil CO₂ flux values in the active period (squares and triangles in **Fig. 4.9**) were clearly higher than those in the inactive period (circles and broken lines in **Fig. 4.9**) in the eastern part of Maekake crater rim where the maximum flux values were obtained in the 2016 survey. Conversely, the flux values near Kamayama crater rim were similar to the values of the inactive period and no significant changes have been observed (**Fig. 4.9**). This characteristic is commonly found in the edge of Kamayama crater (**Fig. 4.8**) where the soil CO₂ flux was high in the inactive period (**Fig. 4.4a**).

Soil temperature values in 2015 and 2016 at the summit area (respectively 54 and 23 in total dataset, **Appendix A.2**) ranged from 6.1 to 18.8 °C with an average value of 10.5 °C and 19.4 to 24.9 °C with an average value of 22.1 °C, respectively (**Table 4.1**). The measurement sites were set mainly in the soil temperature anomalies in 2012–2014, therefore the background temperature for estimating δT was not able to be determined from the measured data. Based on the average

Table 4.3 Summary of the observations in the flanks of Maekake volcano and Jigokudani fumarolic field

Date	Soil CO ₂ flux [g m ⁻² day ⁻¹]					Soil temperature [°C]					
	No. of sites	Min.	Median	Mean	Max.	No. of n. d.	No. of sites	Min.	Median	Mean	Max.
<i>Eastern and western flanks of Maekake volcano</i>											
8 Oct. 2014	7	0.48	0.61	0.78	1.23	2	7	8.4	9.8	9.9	11.4
8 Aug. 2016	5	0.67	1.37	2.11	4.30	2	n.m.	n.m.	n.m.	n.m.	n.m.
<i>Jigokudani fumarolic field</i>											
1 and 9 Aug. 2016	44	6.27	83.5	1,916	2.18×10 ⁴	0	44	11.3	17.3	17.8	24.5

Maximum, mean, median, and minimum values of soil CO₂ flux exclude non-detectable values.
n.d. non-detectable, *n.m.* not measured

soil temperatures and the air temperatures in the 2015 and 2016 surveys, the background temperature for δT calculation was assumed to be 10.0 °C in 2015 and 20.0 °C in 2016 to compare soil temperatures of the active period with those in the inactive period. In **Fig. 4.9**, δT values in the active periods (squares and triangles) show similar profiles to the δT values in the inactive periods (circles and broken lines). This likely indicates that the change of δT values related to the volcanic activity change was minor or negligible even in the eastern part of Maekake crater where huge increases of the soil CO₂ flux values were observed.

4.3 Soil CO₂ flux at the flanks of Maekake volcano

Soil CO₂ flux values in 2014 at the eastern flank of Maekake volcano (7 in total dataset, **Appendix A.1**) ranged from 0.48 to 1.23 g m⁻² day⁻¹ with an average value of 0.78 g m⁻² day⁻¹ (**Table 4.3**). Soil CO₂ flux values in 2016 at the western flank of Maekake volcano (5 in total dataset, **Appendix A.2**) ranged from 0.67 to 4.30 g m⁻² day⁻¹ with an average value of 2.11 g m⁻² day⁻¹ (**Table 4.3**). Almost all the values in the flanks of Maekake volcano were in low range (Population C in **Fig. 4.1**) of the data at the summit area in 2012–2014. All the observed soil CO₂ flux values of the 2012–2016 surveys at the summit area and the flanks are plotted in **Fig. 4.10**. The high CO₂ flux values higher than the range of Population A in **Fig. 4.1** were obtained only in the eastern side of the summit area. Although the soil CO₂ flux measurements for the flanks of Maekake volcano were very limited (only in the eastern and western flanks along the mountain trails), it is assumed that the diffuse CO₂ degassing is negligible on the flanks outside the crater rims of Maekake volcano in this study.

4.4 Soil CO₂ flux and soil temperature at Jigokudani fumarolic field

Soil CO₂ flux values in 2016 at Jigokudani fumarolic field (44 in total dataset, **Appendix A.3**) ranged from 6.27 to 2.18×10⁴ g m⁻² day⁻¹ with an average value of 1,916 g m⁻² day⁻¹ (**Table 4.3**). The maximum CO₂ flux was two order of magnitude higher than the maximum value of the

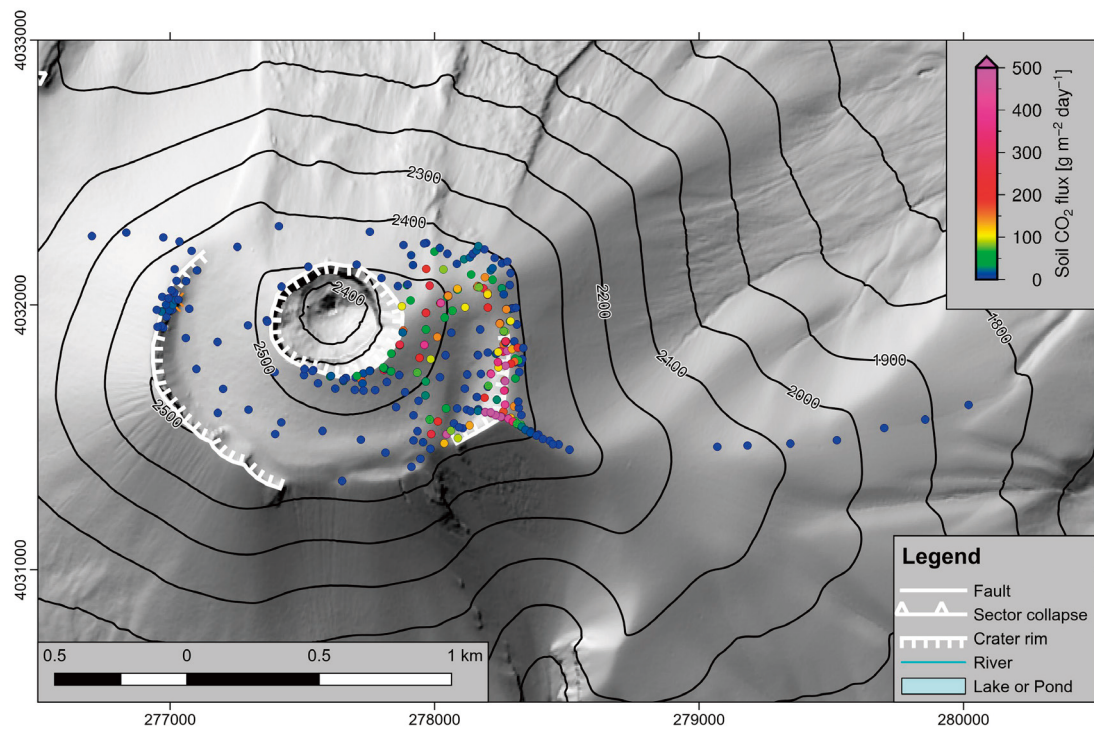


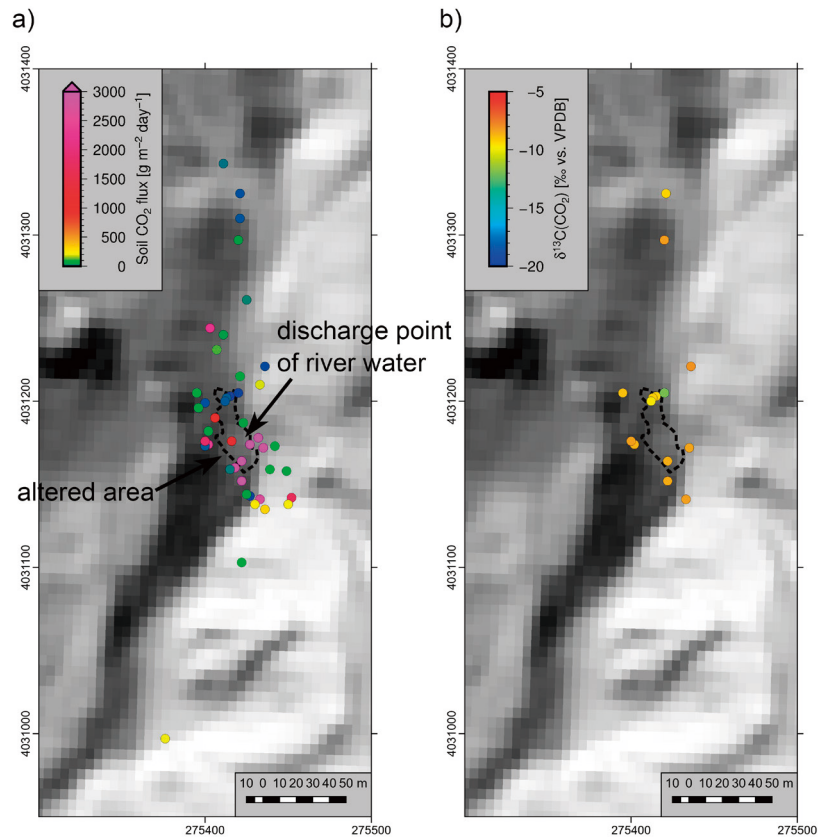
Fig. 4.10 All the soil CO₂ flux values observed in the 2012–2016 surveys. An interval of the contours is 100 m. A digital elevation model (5-m grid) is provided by the Geospatial Information Authority of Japan.

summit area in the inactive period. This value is in the range of CO₂ flux values from ground near fumaroles [e.g., *Chiodini et al.*, 2008]. Although clear fumarolic activity with fumes or significant heat anomalies is currently absent in Jigokudani fumarolic field, this high CO₂ flux value probably indicates that the hydrothermal activity is present beneath Jigokudani fumarolic field and that the diffuse CO₂ is supplied continuously from the hydrothermal fluids.

The soil CO₂ flux values were plotted on a map of the area (**Fig. 4.11a**). The area of the altered region shown in **Fig. 2.5** is depicted with a broken line in **Fig. 4.11a**. High CO₂ flux values (>1,000 g m⁻² day⁻¹) were obtained within or near the altered area (**Fig. 4.11a**). Especially, extremely high soil CO₂ flux values more than 10,000 g m⁻² day⁻¹ were obtained only in the altered area with sulfur precipitation. In the other area, intermediate CO₂ flux values less than a few hundred grams per square meters per day (yellow to green colors in **Fig. 4.11a**) were obtained. The low CO₂ flux values lower than 50 g m⁻² day⁻¹ (blue symbols in **Fig. 4.11a**) were mainly observed from the ground with vegetation, where biogenic contribution to the diffuse CO₂ probably occurs.

The sGs procedure was not performed to the data of Jigokudani fumarolic field because the measurement sites were spatially irregular and they did not limit the high CO₂ flux areas. To estimate an approximate total diffuse CO₂ emission from Jigokudani fumarolic field, the average

►**Fig. 4.11** **a** Soil CO₂ flux values and **b** δ¹³C values of CO₂ in soil gas samples of the 2016 survey in Jigokudani fumarolic field. Coordinates are shown in meter of easting and northing (WGS84, UTM Zone 54 North). A digital elevation model (5-m grid) is provided by the Geospatial Information Authority of Japan.



CO₂ flux value ($1,916 \text{ g m}^{-2} \text{ day}^{-1}$) was multiplied by an area of the altered area surrounded by a broken line in **Fig. 4.11a** (643.9 m^2). The total diffuse CO₂ emission from Jigokudani fumarolic field was calculated to be 1.2 t day^{-1} . This value is the approximate minimum estimation for the total CO₂ emission and includes a large uncertainty. Although the total emission of 1.2 t day^{-1} is a minimum estimation, it is about 10 % of the diffuse CO₂ emission from the summit area. Thus, the diffuse CO₂ emission from Jigokudani fumarolic field cannot be neglected when considering the whole degassing system of Asama volcano.

Soil temperature values in 2016 at Jigokudani fumarolic field (44 in total dataset, **Appendix A.3**) ranged from 11.3 to 24.5 °C with an average value of 17.8 °C (**Table 4.3**). Low soil temperature was mainly obtained near the discharge point of Jaborigawa river (the discharge point is pointed with an arrow in **Fig. 4.11a**). Considering that the water temperature of Jaborigawa river was 15.2 °C on 9 August, the low soil temperatures near the discharge point of the river are probably influenced by the seepage of groundwater that resides beneath the measurement sites.

4.5 Chemical and isotopic compositions of soil gas and bubbling gas

The chemical and isotopic compositions of soil gas and bubbling gas samples from the summit area and Jigokudani fumarolic field are listed in **Table 4.4**. Locations of the sampling

Table 4.4 Chemical compositions (N_2 , O_2 , and CO_2) and $\delta^{13}C(CO_2)$ of soil gas and bubbling gas at the summit area and Jigokudani fumarolic field in 2016

Sample	Longitude [m]	Latitude [m]	Soil CO_2 flux [$g\ m^{-2}\ day^{-1}$]	O_2 [%]	N_2 [%]	CO_2 [%]	$\delta^{13}C(CO_2)$ [‰ vs. VPDB]	
<i>Soil gas at the summit area and the western flank of Maekake volcano</i>								
M01	277,031	4,032,020	4.31	20.9	78.5	0.14	-15.89	± 0.28
M06	276,834	4,032,273	4.30	20.8	78.5	0.51	-16.89	± 0.07
T01	277,508	4,031,758	0.27	20.8	78.1	0.60	-9.47	± 0.08
T03	277,608	4,031,732	18.5	19.9	76.2	0.78	-7.76	± 0.07
T05	277,654	4,031,716	8.86	19.9	76.6	0.89	-6.36	± 0.03
T06	277,706	4,031,732	47.5	20.5	77.8	1.70	-7.66	± 0.06
T08	277,806	4,031,763	63.4	19.7	76.0	1.16	-7.23	± 0.03
T10	277,967	4,031,970	238	18.9	74.6	3.57	-8.31	± 0.06
T11	278,023	4,032,007	429	17.8	73.7	5.22	-8.36	± 0.12
T12	278,051	4,032,034	141	19.5	75.6	4.89	-8.34	± 0.09
T13	278,086	4,032,061	127	19.3	74.9	2.72	-7.46	± 0.06
T14	278,168	4,032,067	79.8	19.3	73.8	6.01	-9.63	± 0.06
T15	278,200	4,032,040	110	18.3	73.5	8.10	-9.11	± 0.08
T16	278,246	4,031,929	144	19.9	76.6	4.05	-7.43	± 0.04
T17	278,261	4,031,901	77.9	19.2	73.3	6.37	-8.59	± 0.07
T18	278,268	4,031,862	298	20.3	77.2	2.54	-8.28	± 0.06
T19	278,239	4,031,784	367	17.4	71.9	10.3	-7.93	± 0.04
T20	278,266	4,031,712	922	17.9	71.1	10.5	-6.93	± 0.04
T21	278,263	4,031,676	360	14.3	63.5	18.5	-6.64	± 0.06
T22	278,250	4,031,577	6,640	13.0	64.0	22.4	-9.29	± 0.03
T23	278,230	4,031,584	2,460	20.2	76.8	2.92	-8.25	± 0.06
T24	278,212	4,031,594	926	19.3	75.4	2.14	n.m.	
<i>Soil gas at Jigokudani fumarolic field</i>								
S02	275,420	4,031,297	37.4	7.93	33.9	42.3	-8.26	± 0.03
S04	275,421	4,031,325	16.2	14.6	56.4	21.3	-9.32	± 0.25
K01	275,420	4,031,205	10.3	20.7	78.7	0.56	-11.96	± 0.19
K02	275,415	4,031,203	6.27	19.3	72.7	6.03	-9.28	± 0.18
K03	275,413	4,031,202	19.6	19.8	74.8	3.73	-9.18	± 0.07
K04	275,412	4,031,200	18.5	19.8	76.5	0.39	-9.66	± 0.17
K05	275,395	4,031,205	94.5	8.24	34.5	48.1	-8.93	± 0.06
K09	275,402	4,031,174	2,368	5.42	22.6	60.1	-8.65	± 0.03
K12	275,400	4,031,176	1,828	2.42	10.3	74.4	-8.31	± 0.05
K13	275,422	4,031,164	7,215	2.17	9.71	75.6	-8.57	± 0.03
K17	275,421	4,031,215	90.2	19.5	77.2	3.09	n.m.	
K19	275,436	4,031,221	13.7	21.0	78.7	0.38	-8.00	± 0.08
K26	275,435	4,031,172	2,844	0.98	13.3	75.5	-8.39	± 0.03
K27-1	275,422	4,031,152	1.52×10^4	3.23	13.9	71.4	-8.59	± 0.04
K27-2	275,422	4,031,152	1.52×10^4	4.07	16.4	68.3	-8.54	± 0.02
K28	275,433	4,031,141	2,659	2.69	23.3	65.1	-8.29	± 0.02
<i>Bubbling gas at Jigokudani fumarolic field</i>								
K99	275,436	4,031,158	n.m.	1.29	7.24	81.1	-8.54	± 0.03
S99	275,406	4,321,124	n.m.	2.95	13.5	66.2	-7.95	± 0.18

n.m. not measured

together with soil CO_2 flux measurement, concentrations of CO_2 , N_2 , and O_2 as well as $\delta^{13}C$ values of CO_2 are shown in the table. **Figs. 4.12a** and **4.12b** show the $\delta^{13}C$ values in soil gas and bubbling gas samples from the summit area and Jigokudani fumarolic field plotted against reciprocal of CO_2 concentrations and soil CO_2 flux values, respectively. The concentration of CO_2 ranged from 0.14 to 22.4 % at the summit area and from 0.38 % to 75.6 % at Jigokudani fumarolic field (**Table 4.4**). Comparing the CO_2 contents and soil CO_2 flux values from the summit area (**Table 4.4**), high CO_2 contents in soil gas larger than a few percent are mainly found from high CO_2 flux sites (>100

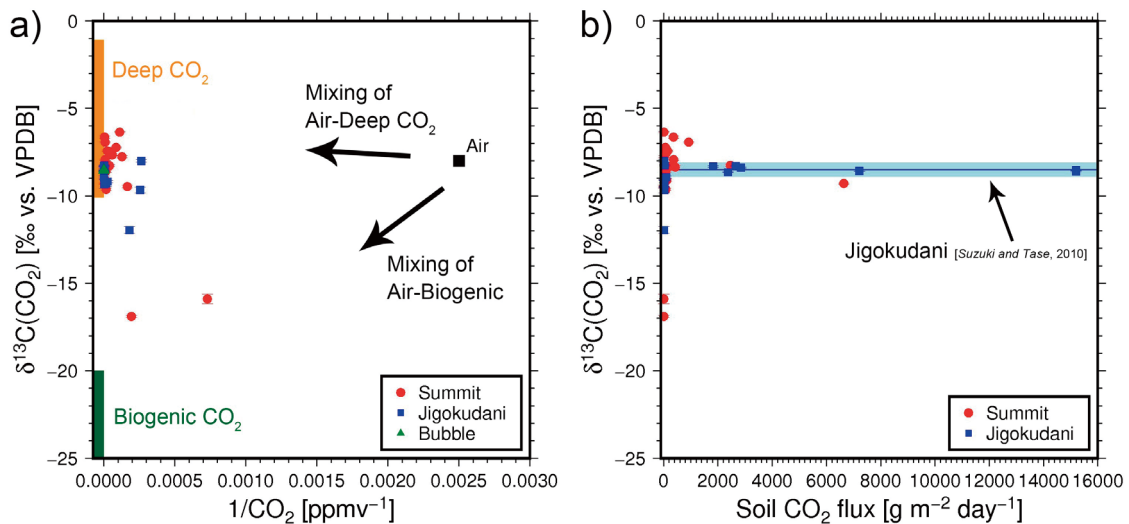
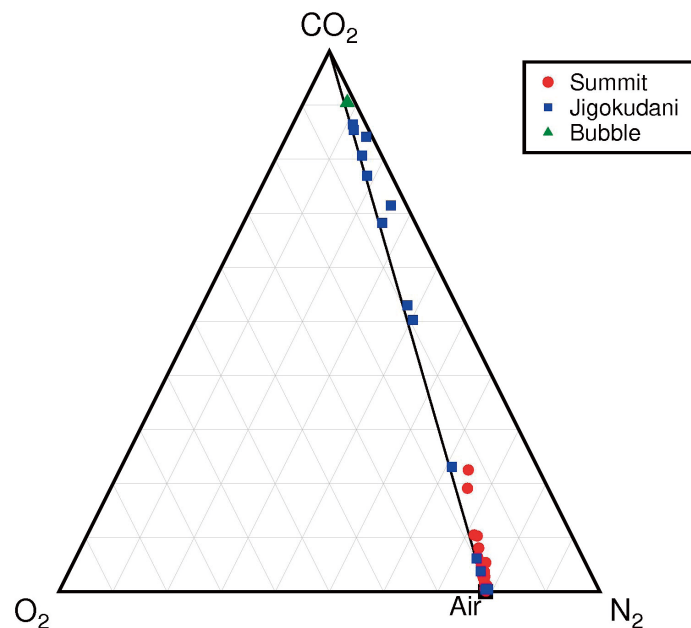


Fig. 4.12 $\delta^{13}\text{C}$ values of CO_2 in soil gas and bubbling gas samples from the summit area and Jigokudani fumarolic field plotted against **a** reciprocal of CO_2 concentrations and **b** soil CO_2 flux values. The end-member ranges for the volcano-hydrothermal, biogenic, and atmospheric CO_2 are also shown in **a** (see text). In **b**, the range of $\delta^{13}\text{C}$ values from soil gas samples in the altered area of Jigokudani fumarolic field reported by Suzuki and Tase [2010] is shown with a light blue area (a broad line is an average and a shaded area is a range of a standard deviation).

► **Fig. 4.13** A trilinear plot of N_2 - O_2 - CO_2 concentrations of the soil gas samples including bubbling gas samples from the summit area and Jigokudani fumarolic field. The end-member of the atmospheric air is shown with a black square. A mixing line of 100% CO_2 and the air is also shown.



$\text{g m}^{-2} \text{ day}^{-1}$). The CO_2 contents and soil CO_2 flux values from Jigokudani fumarolic field also have the similar trend with significantly higher values of CO_2 content and flux compared to those from the summit area (**Table 4.4**). As illustrated in the trilinear plot of N_2 - O_2 - CO_2 concentrations (**Fig. 4.13**), all samples from the summit area (red circles) and Jigokudani fumarolic field (blue squares and green triangles) basically fall on the CO_2 -air mixing line with wide variations of air content.

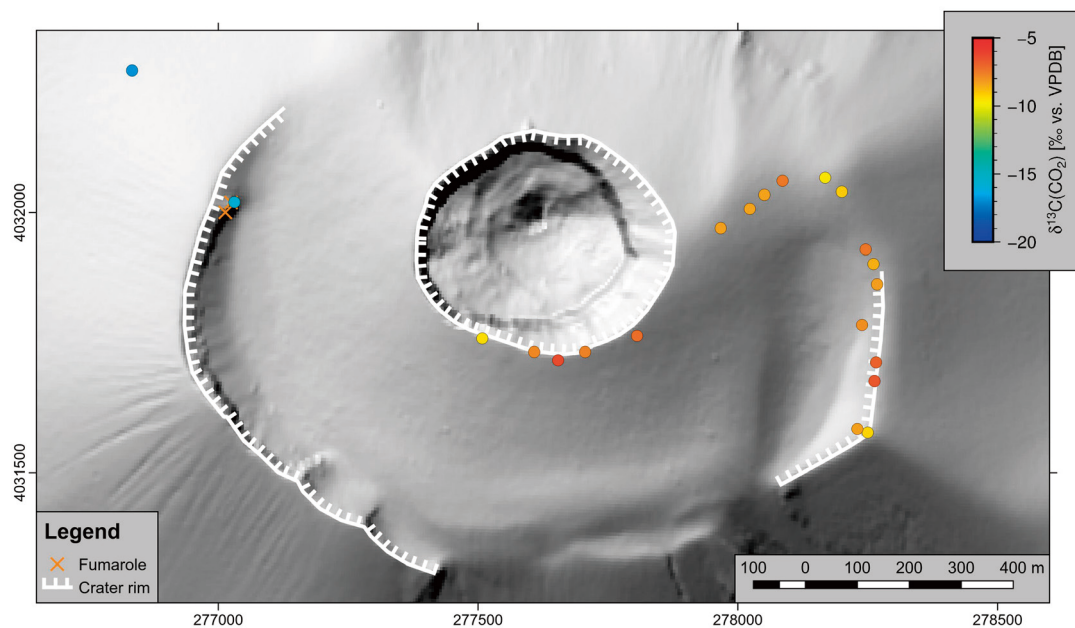


Fig. 4.14 $\delta^{13}\text{C}$ values of CO_2 in soil gas samples of the 2016 survey in the summit area. Coordinates are shown in meter of easting and northing (WGS84, UTM Zone 54 North). A digital elevation model (5-m grid) is provided by the Geospatial Information Authority of Japan.

These characteristics resembles the previous studies of soil gas sampling elsewhere such as in Vulcano Island [Capasso *et al.*, 1997] or Stromboli volcano [Carapezza and Federico, 2000].

The carbon isotopic compositions of soil CO_2 at the summit area ranged from -15.9‰ to -6.4‰ and that of the western flank of Maekake volcano (M06) was -16.9‰ (Table 4.4). The values are indicated on a map of the summit area in Fig. 4.14 to see the distribution of the values. A significant contrast of the carbon isotopic compositions can be seen between the value of the western Maekake crater as well as that of the western flank of Maekake volcano (samples M01 and M06 in Table 4.4) and the values of the eastern part of the study area where the DDS was observed (Fig. 4.14). The $\delta^{13}\text{C}$ value of the western Maekake crater wall (M01) was about -15.9‰ (Table 4.4), which was significantly lower than the average of the samples in the eastern part of the study area ($-8.1 \pm 0.9\text{‰}$).

The $\delta^{13}\text{C}$ values of CO_2 in soil gas and bubbling gas samples at Jigokudani fumarolic field ranged from -12.0‰ to -8.0‰ (Table 4.4) and are indicated on a map in Fig. 4.11b. Almost all the samples from Jigokudani fumarolic field had similar $\delta^{13}\text{C}$ values, especially for the samples with high CO_2 flux values ($>1,000\text{ g m}^{-2}\text{ day}^{-1}$) ranging from -9‰ to -8‰ (Fig. 4.12b). The $\delta^{13}\text{C}$ values of the bubbling gas samples (green triangles in Fig. 4.12a) also correspond to the range of the $\delta^{13}\text{C}$ values with high CO_2 flux values. An average and a standard deviation of $\delta^{13}\text{C}$ values for bubbling gas and soil gas with high CO_2 flux values ($>1,000\text{ g m}^{-2}\text{ day}^{-1}$) was $-8.4 \pm 0.2\text{‰}$. This value corresponds to the range of $\delta^{13}\text{C}$ value of soil gas samples from the altered area of Jigokudani

fumarolic field collected in 1998 and 1999 (-8.5 ± 0.4 ‰, a region surrounded with light blue color in **Fig. 4.12b**) [*Suzuki and Tase, 2010*]. The $\delta^{13}\text{C}$ value of Jigokudani fumarolic field seems to be stable at least for 18 years and this value can probably represent the volcano-hydrothermal CO_2 in Jigokudani fumarolic field.

Chapter 5

Discussion

From the results in the inactive period, the DDS of the summit area was found in the eastern part of the study area showing the N-S elongated elliptical ring and was likely absent in the western part of the study area (**Fig. 4.4a**, **Fig. 4.5**). The similar pattern was also observed in δT values (**Fig. 4.4b**). The extent of the DDS along the eastern Maekake crater rim did not change significantly between the inactive and the active periods (**Fig. 4.8**). The soil CO₂ flux values in the active period were clearly higher than those in the inactive period in the eastern part of Maekake crater rim, but the soil CO₂ flux values near Kamayama crater rim did not show significant changes (**Fig. 4.9**). On the flanks outside the crater rims of Maekake volcano, the diffuse CO₂ degassing is assumed to be negligible (**Fig. 4.10**).

In this chapter, at first, the author discusses about the DDS found in the eastern part of the study area by focusing on the controlling factors of diffuse CO₂ degassing. As mentioned in **Section 1.3**, the ascending process of diffuse CO₂ may be controlled by three factors: regional and volcano-tectonic structures, lithology, and topography [*Schöpa et al.*, 2011; *Peltier et al.*, 2012; *Pantaleo and Walter*, 2014; *Hutchison et al.*, 2015]. Secondly, the heterogeneity of the DDS between the eastern and western parts of the study area is discussed by comparing it with the results of soil gas sampling and the previous studies. Lastly, the degassing system of Asama volcano including the diffuse degassing is presented.

5.1 Controlling factors and the source of diffuse CO₂ degassing

5.1.1 Structure control by regional and volcano-tectonic structures

Firstly, the characteristics of the DDS are compared to regional tectonic structures. The direction of the normal fault near Kurofu volcano is WNW-ESE [*Aramaki*, 1993]. Shear wave splitting on seismograms corresponding to the regional stress field mainly represents the NW-SE trend [*Savage et al.*, 2010]. Additionally, the magma pathway from magma chamber beneath Kurofu volcano to Kamayama crater defines a NW-SE line [*Aoki et al.*, 2013]. Hence, the regional tectonic structures have the NW-SE trend and it does not correspond to the characteristics of the DDS represented as the elliptical ring with the N-S trend. This likely suggests that the DDS is not controlled by regional tectonic structures but instead by volcano-tectonic structures around the summit area.

Comparing the distributions of the DDS with the volcano-tectonic structures around the summit area (**Fig. 4.5**), the eastern part of the elliptical ring DDS corresponds to the eastern rim of Maekake crater that was formed by a collapse of the summit area in the 1108 plinian eruption [*Takahashi and Yasui, 2013; Yasui and Takahashi, 2015*]. Recently, *Yasui and Takahashi [2015]* proposed that the elliptical shape of Maekake crater elongated in E–W resulted from the collapse after a fissure eruption with the E–W trend or from sequential collapses of at least two rounded craters from west to east. Based on the geological studies, they concluded that the latter case (two collapsed craters) was more probable. In **Fig. 5.1**, the DDS of the summit area is compared with the two collapsed craters proposed by *Yasui and Takahashi [2015]*. The first and second collapsed craters correspond to broken lines with labels “Crater 1” and “Crater 2” in **Fig. 5.1**, respectively. The eastern part of the DDS corresponds to the eastern part of the second crater and the western part of the DDS possibly corresponds to the eastern part of the first crater (**Fig. 5.1**). Thus, the DDS presumably reflects the local fractures hidden under the ground along the crater rims. However, the northern and southwestern parts of the DDS do not follow the collapsed crater rims shown in **Fig. 5.1**. To explain the formation of these parts of the DDS, other controlling factors should be considered.

5.1.2 *Lithology control*

The lithology control is generated by the permeability contrasts of the deposits in the volcano body [*Schöpa et al., 2011; Peltier et al., 2012; Pantaleo and Walter, 2014*]. The lithology of the ground surface of the summit area is mainly represented by recent vulcanian deposits [*Yasui and Koyaguchi, 1998; Yasui and Takahashi, 2015*] and there are basically no contrasts of the surface lithology corresponding to the distribution of the DDS. For the lithology contrasts under the ground, the stratigraphy of the shallow part of Kamayama cone can be seen inside Kamayama crater. The inner wall of Kamayama crater is divided into three units consisting of recent vulcanian deposits, pyroclastic materials during the 1783 eruption, and pyroclastic materials before the 1783 eruption [*Yasui and Koyaguchi, 1998, 2004; Yasui and Takahashi, 2015*]. The middle and the lowermost units have stratified structures with columnar joints and the middle unit is very welded [*Yasui and Koyaguchi, 1998*]. The middle unit has some thickness variations of their subunits with directions, but all the subunits exist in any direction [*Yasui and Koyaguchi, 1998*]. Hence, the stratigraphy of the shallow part of Kamayama cone does not seem to form the lithological contrasts corresponding to the DDS.

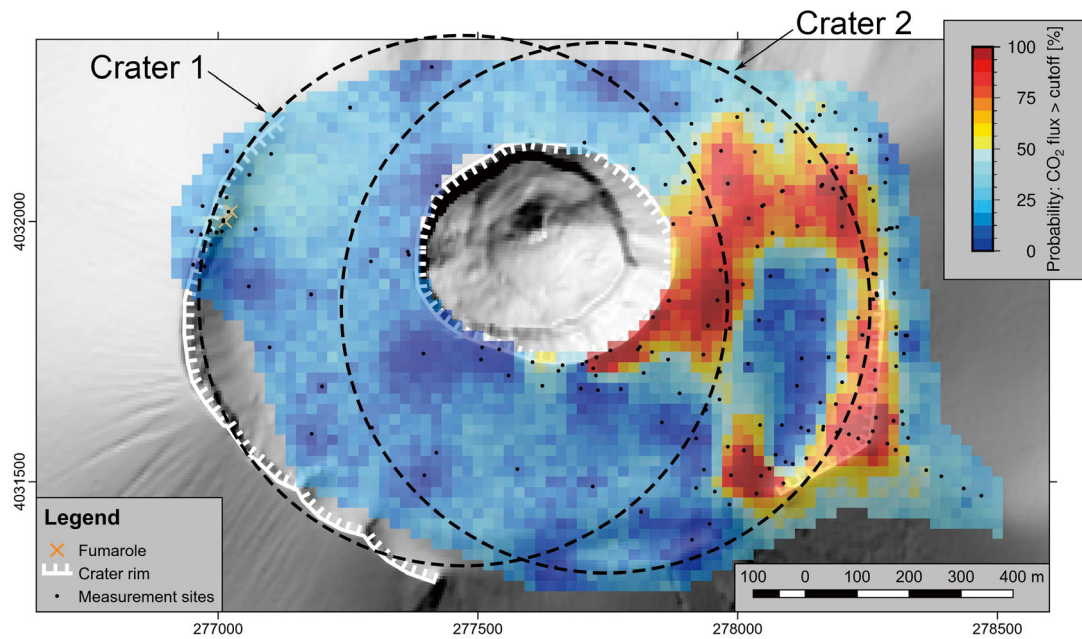


Fig. 5.1 Locations of the two collapsed craters proposed by *Yasui and Takahashi* [2015] shown on the probability map of soil CO₂ flux values in **Fig. 4.5**. Broken lines correspond to the craters ("Crater 1" and "Crater 2"). A digital elevation model (5-m grid) is provided by the Geospatial Information Authority of Japan.

5.1.3 Topography control

Based on *Schöpa et al.* [2011], fumaroles are formed along the crests due to the local stress field induced by topography. To clarify the relation of the DDS and the topography, *Morita et al.* [2016] compared the soil CO₂ flux values with an elevation profile as shown in **Fig. 4.9**. In **Fig. 4.9**, both soil CO₂ flux and δT values are high in the local crests around the eastern Maekake crater rim and the eastern side of Kamayama cone. This correlation was noted as a support that the DDS may be controlled by topography at Asama volcano [*Morita et al.*, 2016].

The averaged soil CO₂ flux values for the 100 realizations (results shown in **Fig. 4.4a**) are projected on a 3-D map of the summit area in **Fig. 5.2**. In **Fig. 5.2a**, the southern part of the DDS is located along the southern part of the eastern Maekake crater rim. In **Figs. 5.2b** and **5.2c**, the northern part of the DDS extends to the northern slope along the ridge lines indicated by arrows in the figures. In **Fig. 5.2d**, the DDS along the eastern Maekake crater rim does not extend below the contour line of 2,420 m. In **Figs. 5.2a–5.2d**, the inner negligible CO₂ flux area surrounded by the elliptical-ring DDS seems to correspond to the lower part or a relative depression in the eastern side of the study area. These images indicate that the DDS is found around the local crests.

To elucidate the topography control on the DDS more clearly, terrain analysis extracting the local crests of the summit area is introduced. The crest is a place where its altitude is higher than the surrounding area in local scale. This factor can be expressed by relative position of the digital elevation model (DEM), which is called as topographic position index (TPI) [*Weiss*, 2001]. The TPI

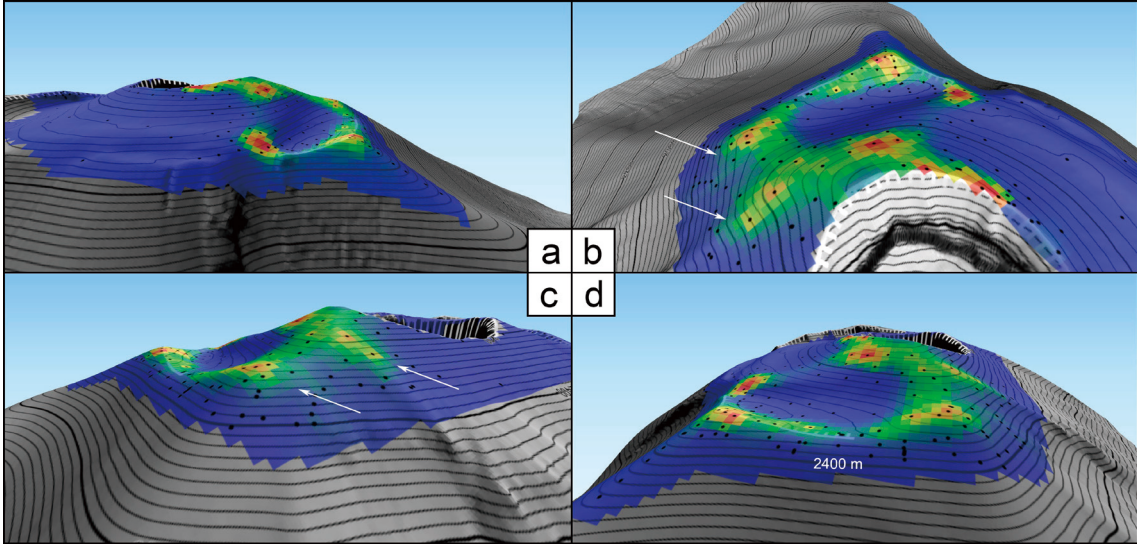


Fig. 5.2 The averaged soil CO₂ flux values of the 100 realizations (**Fig. 4.4a**) projected on a 3-D map of the summit area viewed from **a** SSE, **b** WNW, **c** NNE, and **d** ENE. Arrows in **b** and **c** indicate the extent of the soil CO₂ flux anomalies (see text). An interval of the contours is 10 m. A digital elevation model (5-m grid) is provided by the Geospatial Information Authority of Japan.

compares the altitude of each grid in a DEM to the mean elevation of a specified neighborhood around the grid [Weiss, 2001]. As the specified neighborhood, an annulus neighborhood is used in this study following Weiss [2001]. The TPI is calculated by the following equation [Weiss, 2001; Jenness, 2006]:

$$\text{TPI} = z_0 - \frac{1}{n} \sum_{i=1}^n z_i \quad (5.1)$$

where z_0 is an altitude of the grid, n is a number of grids inside the annulus, and z_i is an altitude of i th grid in the annulus. To construct TPI maps, SAGA GIS 2.2.3 [Conrad *et al.*, 2015] libraries in QGIS software 2.18 [QGIS Development Team, 2016] are used. The crests correspond to positive TPI values in the maps.

The crests derived as the positive TPI values in the TPI maps of Vulcano Island were compared to the permeable zones revealed by stress-field calculation by Schöpa *et al.* [2011]. The DEM of Vulcano Island is provided at 10-m grid by the digital photogrammetry [Baldi *et al.*, 2000] and a shaded relief map illustrated using the DEM is shown in **Fig. 5.3a**. In **Fig. 5.3a**, crater rims of the distinct eruptive stages are also shown with broken lines: Punta Nere (PN), Grotta dei Palizzi (GP), Forgia Vecchia (FV), Pietre Cotte (PC), and Gran Cratere (GC). The circled area in the east of PC is due to artifacts of DEM that are not seen in the original landform [Baldi *et al.*, 2000, fig. 2]. The TPI maps for different sizes of the annulus are calculated and visually compared to select the appropriate size of the annulus for the comparison to the results of Schöpa *et al.* [2011]. From the grid size of the DEM and the scale of crests, the annuli with the outer radii of 10, 30, 50,

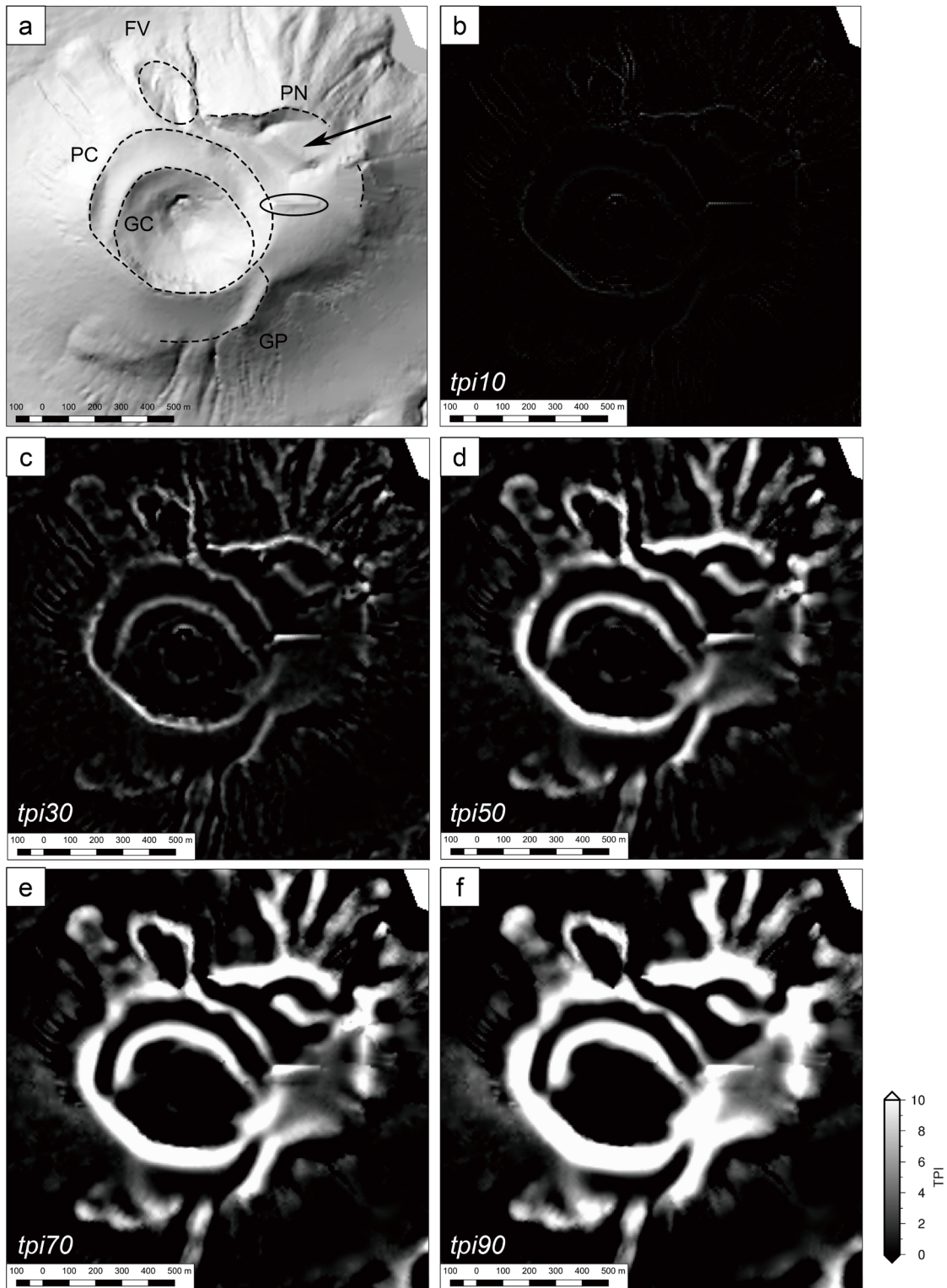


Fig. 5.3 a A shaded relief map of the Fossa cone, Vulcano Island. Crater rims of the distinct eruptive stages are shown with broken lines: Punta Nere (PN), Grotta dei Palizzi (GP), Forgia Vecchia (FV), Pietre Cotte (PC), and Gran Cratere (GC). An area surrounded by a solid line is an artifact of the digital elevation model. An arrow indicates the crest in which CO_2 flux anomalies are found (see text). b-f TPI maps calculated for different outer radii of the annulus (10, 30, 50, 70, and 90 m, respectively). The scale bar of TPI in the right bottom is in meters. The digital elevation model (10-m grid) is from Baldi et al. [2000].

70, 90 m are used and the thickness of the annulus is fixed at 10 m. The constructed TPI maps for 10, 30, 50, 70, and 90 m are shown in **Figs. 5.3b–5.3f**, respectively. In these maps, positive TPI values are expressed with gray to white colors as shown in the fixed scale. The extracted crests of positive TPI values generally correspond to the crater rims (PN, GP, FV, PC, and GC) and other crests such as edges of lava flows. With increasing size of the annulus, the TPI values at the crater rims increase and the area of the positive TPI values along the crater rims becomes wider (**Fig. 5.3**). The five patterns of TPI maps with different radii (**Figs. 5.3b–5.3f**) are compared to the permeable areas of the horizontal stress field at a surface of Vulcano Island ($<3 \times 10^6$ Pa, green to blue colors in Fig. 6 of *Schöpa et al.* [2011]). Based on visual comparisons between Fig. 6 of *Schöpa et al.* [2011] and those of the positive part in the TPI maps (whitish regions in **Figs. 5.3b–5.3f**), the TPI map constructed with the outer radius of 50 m (**Fig. 5.3d**) seems to represent the width and the extent of the permeable zones fairly well. Thus, the TPI map constructed with the outer radius of the annulus of 50 m for Asama is used for the following comparisons with the DDS of the summit area.

The terrain analysis is applied to the DEM of Asama volcano provided by Geospatial Information Authority of Japan. The DEM derived from aerial laser scanner surveys is at 5-m grid. A shaded relief map and a TPI map constructed with the outer radius of 50 m are shown in **Figs. 5.4a** and **5.4b**, respectively. The extracted crests of positive TPI values presented with whitish colors are found along Kamayama crater rims, Maekake crater rims, the southern edge of Kamayama cone, and the northeast slope of Kamayama cone (**Fig. 5.4b**) in the eastern side of the study area where the DDS exists. To compare the crests with the distribution of the DDS (**Fig. 5.4c**, which is the same as **Fig. 4.5**) spatially, the map of TPI values is overlaid on the map of the DDS (**Fig. 5.4d**). In **Fig. 5.4d**, grids with positive TPI values are transparent, thus the probabilities of the DDS (values in **Fig. 5.4c**) are visible. In contrast, the negative TPI values are opaque with black colors and the DDS behind is invisible (**Fig. 5.4d**). In the eastern part of the summit area, yellow to red colors corresponding to the DDS are visible along Kamayama crater rims, Maekake crater rims, and the southern edge and the northeast slope of Kamayama cone (**Fig. 5.4d**). It should be noted that the northwest to northern parts of the DDS (**Fig. 5.4c**), where the DDS cannot be explained by structure or lithology controls, are clearly visible in **Fig. 5.4d**. The extent of the DDS in this area to the northern slopes (pointed by arrows in **Figs. 5.2b** and **5.2c**) also match the extent of the positive TPI values (**Fig. 5.4b**). Although it is very faint and difficult to see, the southwestern part of the DDS, where also the DDS cannot be explained by structure or lithology controls, is faintly visible in **Fig. 5.4d**. These results above indicate that the distribution of the DDS overlaps crests (positive TPI values) even at locations not related to the structure control,

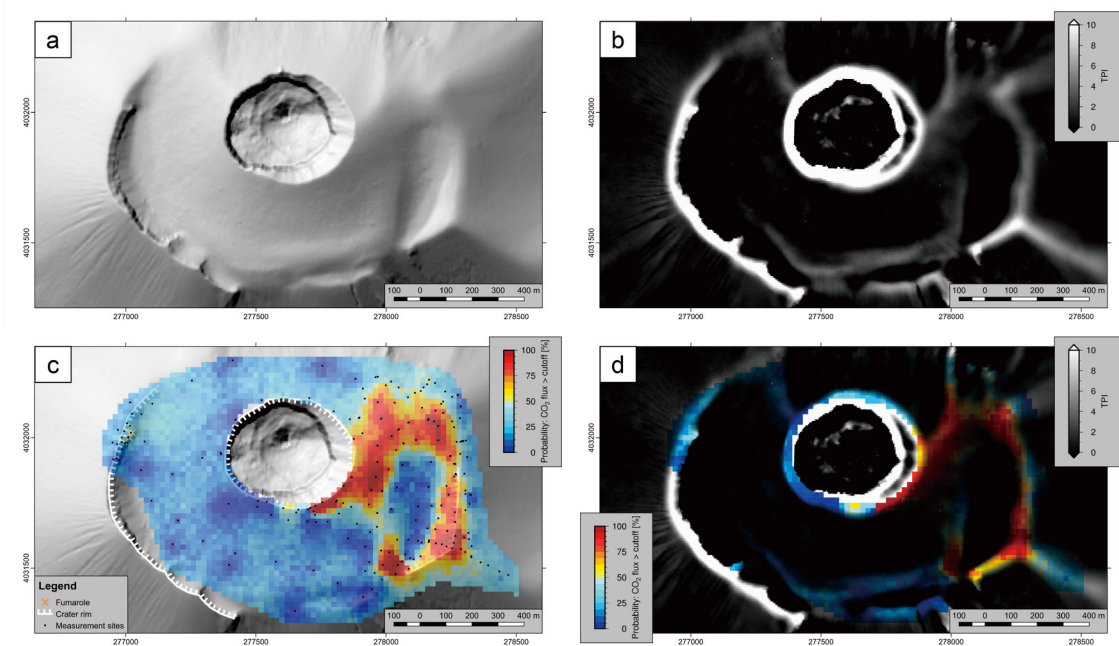


Fig. 5.4 **a** A shaded relief map of the summit area of Asama volcano, **b** A TPI map calculated for the summit area, **c** A probability map for soil CO₂ flux with a cutoff value of 19.1 g m⁻² day⁻¹ (**Fig. 4.5**), and **d** A TPI map (shown in **b**) overlaid on a probability map for soil CO₂ flux (shown in **c**). Coordinates are shown in meter of easting and northing (WGS84, UTM Zone 54 North). A digital elevation model (5-m grid) is provided by the Geospatial Information Authority of Japan.

thus it is likely to consider that the topography control is effective for the DDS distribution found in the eastern side of the summit area of Asama volcano. The area with negative TPI values corresponding to interior of the ring DDS is almost surrounded by positive TPI values (**Fig. 5.4b**) and appears as a depression. The absence of high soil CO₂ flux values in this area (**Fig. 4.4a**) may also be explained by the topography control. Concluding these comparisons, the influence of the topography control is suggested on the diffuse CO₂ degassing of Asama volcano and is spatially indicated by comparison of the TPI map and the DDS in the eastern side of the study area. This comparison between the TPI map and the DDS may be a simple but useful technique as a first-order estimation to grasp spatially the influence of the topography control on the DDS.

In *Schöpa et al.* [2011], the stress-field distribution was not compared to soil CO₂ flux distribution. Here, the horizontal stress field map at a surface of Vulcano Island [*Schöpa et al.*, 2011, fig. 6] as well as the TPI map (**Fig. 5.3d**) are compared to soil CO₂ flux distribution and electrical resistivity structure presented by *Barde-Cabusson et al.* [2009]. The DDS mainly coincides with the crests of the crater rims (GC, PC, and PN), where hidden fractures are supposed to exist [*Barde-Cabusson et al.*, 2009], and also with the crests in the south of PN (pointed with an arrow in **Fig. 5.3a**), where the hidden fractures were not suggested. The latter area is not explained only by the volcano-tectonic structure or lithology but is probably influenced by topography control.

Referring to the resistivity tomography in E–W dimension [Barde-Cabusson *et al.*, 2009, fig. 4], this area corresponds to the low-resistive body at the very shallow part of the volcanic body. The ascent of hydrothermal fluids to this local crest is probably due to the topography control. As in the case indicated here for the DDS at the Fossa cone of Vulcano Island, the horizontal stress field map of Schöpa *et al.* [2011] as well as the TPI map (**Fig. 5.3d**) are useful for finding DDS locations that may be related to the topography control.

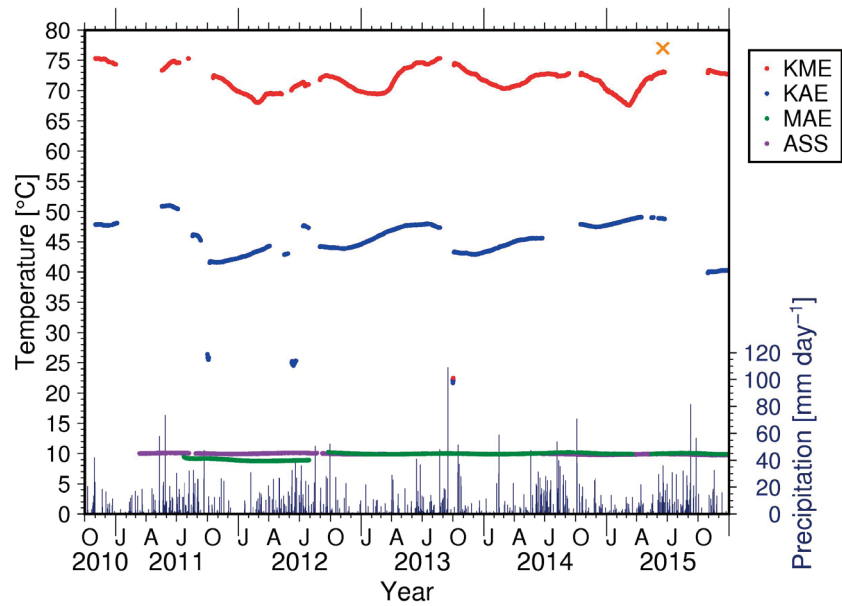
5.1.4 Other controlling factors and the source of diffuse CO₂ degassing

As mentioned in **Section 4.1**, the diffuse CO₂ and heat probably ascend together at the DDS observed in the eastern side of the study area. The heat ascent at the DDS is in fact supported by continuous monitoring data of soil temperature at 12 m depth in tiltmeter borehole stations “KME” and “KAE” (**Fig. 4.4b**) [Ohminato *et al.*, unpublished data, 2015]. The soil temperature values of stations “KME” and “KAE” were respectively about 70 and 45 °C with seasonal variations of 5 °C (**Fig. 5.5**). These stations are located at the observed DDS and the temperature values of these stations were much higher than those of the other stations (about 10 °C) located in the eastern flank of Maekake volcano (“MAE”, about 1 km SE of the main vent inside Kamayama crater) and the southern flank of Kurofu volcano (“ASS”, 3 km southwest of Jigokudani fumarolic field). Thus, it is evident that both diffuse CO₂ and heat ascend together at the DDS of the summit area.

The diffuse CO₂ and heat very likely ascend together at the DDS in the eastern side of the summit area, but they do not ascend to the other parts of the summit area except for the heat and very weak CO₂ emissions observed in the northern part of the western Maekake crater wall (**Fig. 4.9**). Even if the DDS exists in the western side of the summit area as yellow to red colors shown in **Fig. 4.7a**, considering that the size of this area was about 100 grids × 20 m × 20 m and that the CO₂ flux values in this area were mostly lower than 10 g m⁻² day⁻¹ (**Fig. 4.2a**), the diffuse CO₂ emission from this area would be just a few percent of the diffuse CO₂ emission from the whole study area. This heterogeneity between the eastern and western parts of the summit area is a peculiar feature of Asama volcano and is also recognizable in the δ¹³C values of soil gas samples from the summit area (**Section 4.5**). As illustrated in **Figs. 4.12** and **4.14**, the δ¹³C value of the western Maekake crater wall (–15.9 ‰) is significantly lower than the average of the samples in the eastern part of the study area (–8.1±0.9 ‰).

The δ¹³C value of diffuse CO₂ can characterize the CO₂ sources corresponding to volcano-hydrothermal, biogenic, and atmospheric [Chiodini *et al.*, 2008]. The δ¹³C value of the biogenic CO₂ has a wide range: for C₃ plants, it ranges from –35 ‰ to –20 ‰ with a mean of –27 ‰; for C₄ plants, it ranges from –15 ‰ to –7 ‰ with a mean of –13 ‰ [Cheng, 1996]. The δ¹³C value of

► **Fig. 5.5** Soil temperature at 12 m depth from the surface obtained in tiltmeter boreholes of ERI [Ohminato *et al.*, unpublished data, 2015]. Precipitation data at the weather station of Karuizawa is also shown. Orange crosses in June 2015 correspond to the minor eruptions.



the atmospheric air is about -8 ‰ [Hoefs, 2004]. For $\delta^{13}\text{C}$ value of volcano-hydrothermal CO_2 data of fumarole, bubbling gas, mofette, and geothermal well at volcanoes and geothermal fields are compiled in **Appendix B.1** following Sano and Williams [1996], Oppenheimer *et al.* [2014], and Kagoshima *et al.* [2015]. This dataset mainly consists of the data from high to intermediate temperature fumaroles at active volcanoes. Based on this compilation, the average $\delta^{13}\text{C}$ value of CO_2 emitted from the subduction volcanoes is -5.6 ‰ with a standard deviation of 4.5 ‰ . Considering $\delta^{13}\text{C}$ values of the sources above and **Fig. 4.12**, the samples in the eastern part of the study area ($-8.1 \pm 0.9\text{ ‰}$) is strongly influenced by the volcano-hydrothermal CO_2 , whereas the samples from the western Maekake crater wall (-15.9 ‰) is more influenced by the biogenic CO_2 with low influence of the volcano-hydrothermal CO_2 .

As discussed in the previous sections, both the structure and topography controls are affecting the distribution of the DDS in the eastern side of the study area. However, considering that the fractures estimated from the collapsed craters in **Fig. 5.1** and/or crests (positive TPI values) in **Fig. 5.4b** exist not only in the eastern side but also in other areas of the study area, the distribution of soil CO_2 flux in the summit area cannot be explained just by the structure, lithology, and topography controls. Therefore, other controlling factors should be considered to explain the heterogeneous distribution of the soil CO_2 flux for the summit area of Asama volcano.

To find a clue to explain the presence of the DDS only in the eastern side, the author referred to the electrical resistivity structure of Asama volcano [Aizawa *et al.*, 2008]. According to the E–W profile of the 2-D resistivity model by magnetotelluric (MT) and audio-magnetotelluric (AMT) measurements, a low-resistive body ($<10\ \Omega\ \text{m}$) resides in a shallower depth under the eastern

part of the summit area than the western part of that [Aizawa *et al.*, 2008, fig. 10]. Especially, the lowest resistive body (about 1 Ω m) is located only in the eastern side. Preliminary results of a recent denser MT and AMT surveys at the summit area [Koyama *et al.*, 2013] also suggest that the eastern part of Maekake crater has an apparent resistivity as low as several ohmmeters at a depth corresponding to a frequency of about 1 Hz. A low-resistive body in a volcanic edifice can be interpreted as hydrothermal fluid and/or clay-rich layer [Nurhasan *et al.*, 2006; Aizawa *et al.*, 2008]. Considering that the DDS accompanying heat exists in the eastern part and that the $\delta^{13}\text{C}$ values of soil gas samples in the eastern part are mainly explained by the volcano-hydrothermal CO_2 source, it is evident that the low-resistive body in the eastern part corresponds to hydrothermal fluids and the diffuse CO_2 observed in this area would be the hydrothermal fluids ascending from the low-resistive body. Upper part of the low-resistive body in the eastern side may consist of clay-rich layer, but there must be pathways probably related to the collapsed craters, which reach the hydrothermal fluid layer for ascending fluids. A low-resistive body also resides under the western part of the summit area but deeper than the eastern side [Aizawa *et al.*, 2008, fig. 10]. A plausible explanation for the lack of DDS in the western part may be that the pathways of the fluid do not reach the hydrothermal source as in the eastern side because of relatively deeper low-resistive body and/or sealing of clay-rich layers, or that the amount of hydrothermal fluids is lower in the western side. Since the weak steam emission and small amount of soil CO_2 flux with a little contribution of the volcano-hydrothermal CO_2 source exist on the western Maekake crater wall, relatively weak pathways may at least exist in the western side. But, in any case, presence of both the hydrothermal source and the connection from the hydrothermal source to the pathways of diffuse CO_2 are important for the DDS to appear in the surface, and they probably control the E–W heterogeneous diffuse CO_2 distribution observed in the summit area of Asama volcano. In general, it is certain that the main controlling factors for the hydrothermal fluid ascent are the structure, lithology, and topography controls, which significantly influence permeability of relatively shallow volcanic body, but presence of the source and its connection to shallower pathways should also be considered as shown in the case study of Asama volcano. This idea could be applied to explain the heterogeneous distribution of soil CO_2 flux observed in other volcanoes such as Vesuvio volcano [Fron dini *et al.*, 2004]. The conclusion here may be obvious but definitely an important controlling factor for considering the fluid ascent.

5.2 Degassing system of Asama volcano

The total emission rate of diffuse CO_2 from the summit area was 12.6 t day⁻¹ with a standard deviation range of 12.2–14.6 t day⁻¹ in the inactive period as calculated in **Section 4.1** and in

Morita et al. [2016]. The diffuse CO₂ flux distribution and its emission rate of Asama volcano are estimated for the first time. This is an important estimation because little is known for the diffuse CO₂ emission from Japanese volcanoes especially for persistent degassing volcanoes [*Shinohara*, 2013] and because Asama volcano is one of the six active degassing volcanoes in Japan [*Mori et al.*, 2013]. A plume CO₂ emission rate can be calculated by multiplying a plume SO₂ flux by a plume CO₂/SO₂ ratio [*Fischer*, 2008; *Burton et al.*, 2013]. The plume SO₂ flux between October 2012 and October 2014 was 50–300 t day⁻¹ with an average of 170 t day⁻¹ (**Fig. 2.3**). The plume CO₂/SO₂ ratio is fairly stable between active and inactive periods (**Fig. 2.3**), and the average CO₂/SO₂ ratio of the plume is reported to be about 0.80 [*Shinohara et al.*, 2015]. Using these data above, the plume CO₂ flux in the inactive period is estimated to be 28–170 t day⁻¹ with an average of 94 t day⁻¹. The proportion of diffuse to total CO₂ emissions from the summit area is estimated to be 12 % (6.7–34 %). To evaluate the characteristics of the diffuse CO₂ degassing from Asama volcano, the proportion of diffuse/total CO₂ emission is compared with those of other active degassing volcanoes (**Table 5.1**). For intensive plume degassing volcanoes, the ratio generally ranges from almost 0 % to about 50 % with the typical ratio of 10–20 %. The ratio of 12 % for Asama volcano is a typical value. For Japanese volcanoes in **Table 5.1**, the ratios are 0.02 % and 17 % respectively for Aso and Satsuma-Iwojima volcanoes. At Aso volcano, the soil CO₂ flux values were mostly negligible [*Saito et al.*, 2007]. At Satsuma-Iwojima volcano, the observed high CO₂ flux values were recorded outside the main cone of Iwodake and the diffuse CO₂ emission was not detected from the summit area of the cone [*Shimoike et al.*, 2002]. Thus, the clear DDS observed in the summit area of Asama volcano is the first time among the intensive plume degassing volcanoes in Japan. The results obtained at Asama volcano would provide valuable data for understanding volatile flux from Japanese volcanoes as the representative data for the intensive degassing volcanoes.

A schematic diagram of the degassing system of Asama volcano during inactive period considering the results of the previous studies and this study is presented in **Fig. 5.6**. Magmatic volatiles ascending through the conduit (shown as a dike-like conduit and the red arrows along the hypocenters in **Fig. 5.6**) are mainly emitted as volcanic plume with an emission rate of 94 t day⁻¹, which corresponds to about 88 % of total CO₂ emission. Some portion of the volatiles in the conduit spread into the low-resistive body under the summit area of Maekake volcano (orange and pink lines in **Fig. 5.6**) especially toward the eastern side. The ascending hydrothermal fluids are connected to permeable zones that correspond to the pathways of diffuse degassing by structure control probably related to fractures of the collapsed craters (black lines under the summit area in **Fig. 5.6**) and by topography control. The pathways are connected to the hydrothermal fluids in the eastern part but very weakly in the western part because of the larger depth of the

Table 5.1 Plume/fumarole and diffuse CO₂ emissions and diffuse/total ratio of active degassing volcanoes following Viveiros *et al.* [2010], Burton *et al.* [2013], Hernández *et al.* [2015], and Morita *et al.* [2016]

Volcano	Country or area	Plume or fumarole emission [t day ⁻¹]	Diffuse emission [t day ⁻¹]	Diffuse/total ratio [%]	Reference
Popocatepetl	México	32,000	n.d.	0	Goff <i>et al.</i> , 2001; Varley and Armienta, 2001
Aso	Japan	600	0.12	0.02	Saito <i>et al.</i> , 2007
Ol Doinyo Lengai	Tanzania	6,600 ^a	ca. 100	ca. 1	Koepenick <i>et al.</i> , 1996
Erebus	Antarctica	1,930 ^a	40	2.0	Wardell <i>et al.</i> , 2003, 2004
Masaya	Nicaragua	930	20	2.1	Lewicki <i>et al.</i> , 2003; Aiuppa <i>et al.</i> , 2014
Stromboli	Italy	370	46	11	Inguaggiato <i>et al.</i> , 2013
Asama	Japan	94 ^a	12.6	12	This study
White Island	New Zealand	890 ^a	124	12	Werner <i>et al.</i> , 2008; Bloomberg <i>et al.</i> , 2014
Ukinrek Marrs	USA	187	33 ^a	15	Doukas and McGee, 2007; Evans <i>et al.</i> , 2009
Satsuma-Iwojima	Japan	100	20	17	Shimoike <i>et al.</i> , 2002
Vulcano Island	Italy	360	91	20	Inguaggiato <i>et al.</i> , 2012
Etna	Italy	35,000	20,000	36	Hernández <i>et al.</i> , 2015
Merapi	Indonesia	240	215 ^a	47	Toutain <i>et al.</i> , 2009
Sierra Negra	Galápagos	394	605	61	Padrón <i>et al.</i> , 2012a
Pantelleria Island	Italy	77	880	92	Favara <i>et al.</i> , 2001
Raykjanes	Iceland	0.23	13.5	98	Fridriksson <i>et al.</i> , 2006
Ischia	Italy	3	1,282	100	Pecoraino <i>et al.</i> , 2005

^aAn average value of multiple measurements or references
n.d. not detected

hydrothermal source and/or sealing clay-rich layers. Not only the local topography and fractures but also the connection between the hydrothermal fluid source and the pathways create the E–W heterogeneous CO₂ flux distribution and the peculiar DDS revealed as the elliptical ring with N–S trend only in the eastern side of the summit area. The diffuse CO₂ emission of 12.6 t day⁻¹ accounts for about 12 % of the total CO₂ supplied to the summit area. The diffuse CO₂ emission from Jigokudani fumarolic field is at minimum 1.2 t day⁻¹, which is supplied from the hydrothermal fluids under Kurofu volcano coexisting with altered rocks [Aizawa *et al.*, 2008]. By including the diffuse CO₂ emission from peripheral areas of Maekake volcano like Jigokudani fumarolic field, the diffuse/total CO₂ emission ratio of this volcano might be slightly larger than the ratio calculated above.

Although the change in the diffuse CO₂ emission rate between inactive and active periods was not able to reveal in this study, the increase of diffuse CO₂ flux from the eastern Maekake crater rim in active periods (Fig. 4.9) might indicate an increase of the diffuse CO₂ emission from the summit area. The plume CO₂ emission in the active period is definitely one or two order of magnitude higher than that in the inactive period (Fig. 2.3). The change in diffuse/total CO₂ emission ratio corresponding to the activity change of the volcano would be very useful to understand the degassing system more clearly. However, conducting the diffuse CO₂ flux surveys

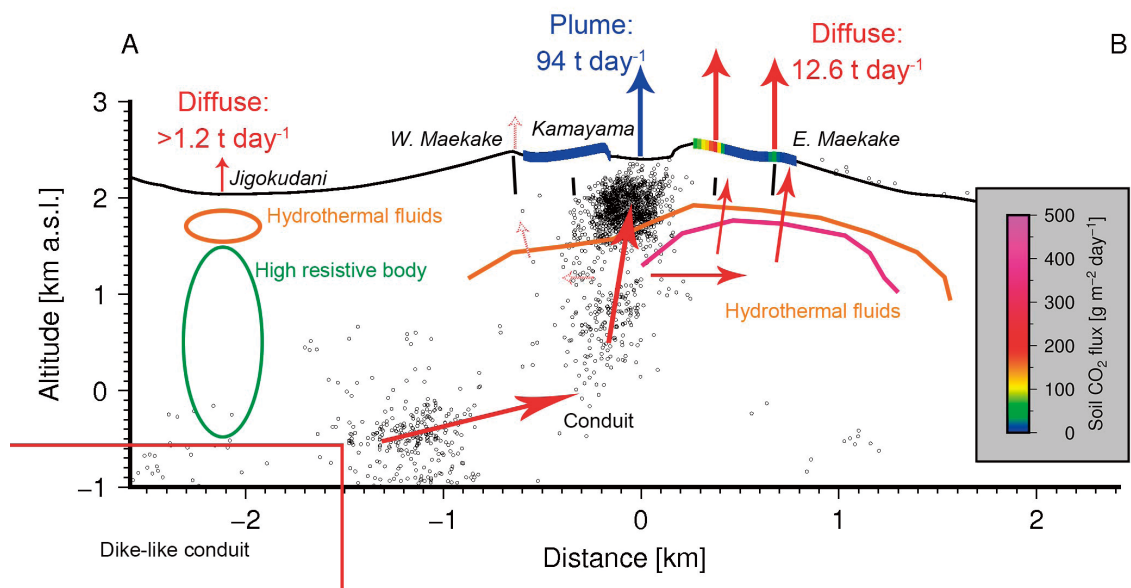


Fig. 5.6 A schematic diagram of the transport of magmatic volatiles to diffuse emission at Asama volcano [modified from *Morita et al.*, 2016]. Gray circle shows a hypocenter during 2004–2015 [*Takeo et al.*, unpublished data, 2015] denoting the location of the main conduit. A location of the dike is from *Takeo et al.* [2006], which is partly shown in this figure. Pink and orange lines under Maekake volcano and under Jigokudani fumarolic field, respectively, correspond to about 1 and 10 Ω m contours of the low-resistive body [*Aizawa et al.*, 2008]. A high-resistive body under Jigokudani is also shown with a green ellipse [*Aizawa et al.*, 2008]. The horizontal length of the high resistive body is unknown. Arrows indicate movement and emission of magmatic volatiles and/or hydrothermal fluids, and arrows with dashed lines in the western side of Maekake volcano indicate the flux is low. Black lines under Maekake volcano correspond to assumed fractures of the two collapsed craters of the 1108 plinian eruption [*Yasui and Takahashi*, 2015]. The length and depth of the fractures are unknown. A digital elevation model (5-m grid) is provided by the Geospatial Information Authority of Japan.

to cover all the study area during the active period would be difficult considering the safety of the observers. Thus, conducting a continuous measurement of diffuse CO_2 flux [e.g., *Carapezza et al.*, 2004; *Pérez et al.*, 2012] may be plausible. In this case, effective site for monitoring the volcanic activity changes by the continuous diffuse CO_2 flux measurement would be at the eastern Maekake crater rim considering the results in **Section 4.2** of this study.

The heterogeneous distribution of the DDS and $\delta^{13}\text{C}$ values compared to the electrical resistivity structure has revealed the presence of hydrothermal fluids and their ascent in the eastern part of the summit area. This is an important information for understanding the structural framework of Asama volcano. The hydrothermal fluids at the low-resistive body would alter the host rock [*Aizawa et al.*, 2008], if the supply of the hydrothermal fluids continues. Changes in the supply rate would control the further alteration of the hydrothermal area. Thus, further repetitive surveys of diffuse CO_2 emissions in this area would be important to understand the development of the hydrothermal system of the volcano especially in the eastern part of the summit area.

Chapter 6

Conclusions

The surveys of diffuse CO₂ flux at the summit area of Asama volcano (Japan) were conducted six times during 2012–2016. Four surveys with total of 211 measurements were conducted in the inactive period before the 2015 minor eruptions. After the 2015 minor eruptions, two surveys with total of 80 measurements were conducted in October 2015 and August 2016. In the 2016 survey, soil gas samples were collected and analyzed for chemical and isotopic compositions at selected measurement sites. A limited number of the measurements were conducted also at the flanks of Maekake volcano and at Jigokudani fumarolic field.

For the observed soil CO₂ flux values of the summit area in the inactive period, statistical analysis based on the graphical statistical approach (GSA) was applied [Sinclair, 1974; Chiodini *et al.*, 1998], and spatial distributions of the soil CO₂ flux and δT values were constructed by sequential Gaussian simulation (sGs) [Deutsch and Journel, 1998; Cardellini *et al.*, 2003b].

The soil CO₂ flux distribution of the inactive period showed the E–W heterogeneous distribution at the summit area and the diffuse degassing structure (DDS) was found only in the eastern side of the study area which formed an elliptical-ring shape elongated to N–S. In the northern, southern, and western parts of the study area, the soil CO₂ flux values were basically negligible except for a small area on the western Maekake crater wall. The similar pattern was also observed in the spatial distribution of δT values.

To explain the ring shape of the DDS in the eastern side of the summit area, influences of the structure, lithology, and topography controls were discussed. The ring shape of the DDS is likely explained by the volcano-tectonic structures corresponding to hidden fractures of the two collapsed craters [Yasui and Takahashi, 2015] and by the topography control as revealed by comparisons between the DDS distribution and the topographic position index (TPI) map, which was introduced to extract the local crests of the summit area. Especially for the northern and southwestern parts of the DDS, the topography control should be considered to explain the observed DDS. The comparison using the TPI map may be a simple but useful technique as a first-order estimation to grasp spatially the influence of the topography control on the DDS. This technique may be also useful for planning locations of measurement sites for the diffuse degassing surveys.

The E–W heterogeneity of the CO₂ flux distribution and the $\delta^{13}\text{C}$ values of soil CO₂ indicated

that other controlling factors except for the structure, lithology, and topography controls should also be considered for the summit area of Asama volcano. The E–W profile of the electrical resistivity structure of Asama volcano [Aizawa *et al.*, 2008] suggested that a low-resistive body resides at shallower depth under the eastern side of Maekake volcano than the western side. Comparisons of the resistivity structure and the results of this study indicated that the low-resistive body in the eastern part corresponds to hydrothermal fluids as the source of the diffuse CO₂. The comparison also suggested that the negligible or very small diffuse CO₂ degassing in the western part may be explained by the very weak connection of the hydrothermal source to the ascending pathways of the fluids or by the low amount of the hydrothermal fluids in the western side. The presence of both the hydrothermal source and the connection from the hydrothermal source to the ascending pathways are probably important to form the E–W heterogeneous diffuse CO₂ distribution observed in the summit area of Asama volcano. The conclusion here may be obvious but definitely an important controlling factor for considering the fluid ascent not only for Asama volcano but also for other volcanoes.

This study revealed that a total emission rate of diffuse CO₂ from the summit area of Asama volcano was 12.6 t day⁻¹ with a standard deviation range of 12.2–14.6 t day⁻¹ in the inactive period and that such significant amount (about 12 % of total CO₂ emission) is emitted as diffuse CO₂ from the eastern part of the summit area. The clear DDS observed in the summit area of Asama volcano is the first time among the intensive plume degassing volcanoes in Japan, and the results obtained at Asama volcano would provide valuable data for understanding volatile flux from Japanese volcanoes as the representative data.

Considering the results of the previous studies and this study, a schematic diagram of the degassing system of Asama volcano during inactive period is presented in **Fig. 5.6**. Magmatic volatiles are mainly emitted as volcanic plume with an emission rate of 94 t day⁻¹ (about 88 % of total CO₂ emission) and some portion of the volatiles spread into the low-resistive body under the summit area of Maekake volcano (orange and pink lines in **Fig. 5.6**) especially toward the eastern side. The ascending hydrothermal fluids are connected to permeable zones that correspond to the pathways of diffuse degassing by structure control (fractures of the collapsed craters shown as black lines under the summit area in **Fig. 5.6**) and by topography control. The pathways are connected to the hydrothermal fluids in the eastern part but relatively weakly in the western part because of the larger depth of the hydrothermal source and/or sealing clay-rich layers. The diffuse CO₂ emission of 12.6 t day⁻¹ (about 12 % of total CO₂ emission) from the summit area is significant to consider the degassing system of Asama volcano, and the diffuse CO₂ emission observed only in the eastern side of the summit area is important for understanding the structural framework

of Asama volcano. Because the hydrothermal fluids in the low-resistive body would alter the host rock [Aizawa *et al.*, 2008], changes in the supply rate would control the further alteration of the hydrothermal area. Thus, further repetitive surveys of diffuse CO₂ emissions in this area would be important to understand the development of the hydrothermal system of the volcano especially in the eastern part of the summit area.

The diffuse CO₂ flux values of the active period in the eastern part of Maekake crater rim showed significant increase from those of the inactive period, but the flux values near Kamayama crater rim did not show significant change. Thus, the results of this study suggest that eastern Maekake crater rim may be an effective site for monitoring the volcanic activity by the continuous diffuse CO₂ flux measurement in the future.

References

- Agusto, M., F. Tassi, A. T. Caselli, O. Vaselli, D. Rouwet, B. Capaccioni, S. Caliro, G. Chiodini, and T. Darrah (2013), Gas geochemistry of the magmatic-hydrothermal fluid reservoir in the Copahue–Caviahue Volcanic Complex (Argentina), *J. Volcanol. Geotherm. Res.*, **257**, 44–56, doi:10.1016/j.jvolgeores.2013.03.003.
- Aiuppa, A., R. Moretti, C. Federico, G. Giudice, S. Guerrieri, M. Liuzzo, P. Papale, H. Shinohara, and M. Valenza (2007), Forecasting Etna eruptions by real-time observation of volcanic gas composition, *Geology*, **35**(12), 1115–1118, doi:10.1130/G24149A.1.
- Aiuppa, A., M. Burton, T. Caltabiano, G. Giudice, S. Guerrieri, M. Liuzzo, F. Murè, and G. Salerno (2010), Unusually large magmatic CO₂ gas emissions prior to a basaltic paroxysm, *Geophys. Res. Lett.*, **37**, L17303, doi:10.1029/2010GL043837.
- Aiuppa, A., P. Robidoux, G. Tamburello, V. Conde, B. Galle, G. Averd, E. Bagnato, J. M. De Moor, M. Martínez, and A. Muñoz (2014), Gas measurements from the Costa Rica–Nicaragua volcanic segment suggest possible along-arc variations in volcanic gas chemistry, *Earth Planet. Sci. Lett.*, **407**, 134–147, doi:10.1016/j.epsl.2014.09.041.
- Aizawa, K., Y. Ogawa, T. Hashimoto, T. Koyama, W. Kanda, Y. Yamaya, M. Mishina, and T. Kagiya (2008), Shallow resistivity structure of Asama volcano and its implications for magma ascent process in the 2004 eruption, *J. Volcanol. Geotherm. Res.*, **173**(3–4), 165–177, doi:10.1016/j.jvolgeores.2008.01.016.
- Allard, P. (1979), ¹³C/¹²C and ³⁴S/³²S ratios in magmatic gases from ridge volcanism in Afar, *Nature*, **282**, 56–58, doi:10.1038/282056a0.
- Allard, P. (1980a), Composition isotopique du carbone dans les gaz d'un volcan d'arc: Le Momotombo (Nicaragua), *C. R. Seances Acad. Sci., Ser. D*, **290**, 1525–1528 (in French with English abstract).
- Allard, P. (1980b), Proportions des isotopes ¹³C et ¹²C du carbone émis à haute température par un dôme andésitique en cours de croissance: Le Mérapi (Indonésie), *C. R. Seances Acad. Sci., Ser. D*, **291**, 613–616 (in French with English abstract).
- Allard, P. (1981), Composition isotopique du carbone dans les gaz d'un magma dacitique (volcan Usu, Japon): Relation entre le rapport ¹³C/¹²C des volatils et le rapport ⁸⁷Sr/⁸⁶Sr de la phase silicatée dans le volcanisme d'arc, *C. R. Acad. Sci., Ser. II: Mec., Phys., Chim., Sci. Terre Univers*, **293**, 583–586 (in French with English abstract).
- Allard, P. (2010), A CO₂-rich gas trigger of explosive paroxysms at Stromboli basaltic volcano, Italy, *J.*

- Volcanol. Geotherm. Res.*, **189**(3–4), 363–374, doi:10.1016/j.jvolgeores.2009.11.018.
- Allard, P. et al. (1991), Eruptive and diffuse emissions of CO₂ from Mount Etna, *Nature*, **351**, 387–391, doi:10.1038/351387a0.
- Allard, P., P. Jean-Baptiste, W. D'Alessandro, F. Parello, B. Parisi, and C. Flehoc (1997), Mantle-derived helium and carbon in groundwaters and gases of Mount Etna, Italy, *Earth Planet. Sci. Lett.*, **148**(3–4), 501–516, doi:10.1016/S0012-821X(97)00052-6.
- Allard, P., A. Aiuppa, F. Beatuducel, D. Gaudin, R. Di Napoli, S. Calabrese, F. Parello, O. Crispi, G. Hammouya, and G. Tamburello (2014), Steam and gas emission rate from La Soufriere volcano, Guadeloupe (Lesser Antilles): Implications for the magmatic supply during degassing unrest, *Chem. Geol.*, **384**, 76–93, doi:10.1016/j.chemgeo.2014.06.019.
- Aoki, Y., H. Watanabe, E. Koyama, J. Oikawa, and Y. Morita (2005), Ground deformation associated with the 2004–2005 unrest of Asama volcano, Japan, *Bull. Volcanol. Soc. Jpn.*, **50**(6), 575–584 (in Japanese with English abstract).
- Aoki, Y. et al. (2009), P-wave velocity structure beneath Asama volcano, Japan, inferred from active source seismic experiment, *J. Volcanol. Geotherm. Res.*, **187**(3–4), 272–277, doi:10.1016/j.jvolgeores.2009.09.004.
- Aoki, Y., M. Takeo, T. Ohminato, Y. Nagaoka, and K. Nishida (2013), Magma pathway and its structural controls of Asama Volcano, Japan, in *Remote Sensing of Volcanoes and Volcanic Processes: Integrating Observation and Modelling*, *Geol. Soc. Spec. Publ.*, vol. 380, edited by D. M. Pyle, T. A. Mather, and J. Biggs, pp. 67–84, doi:10.1144/SP380.6.
- Aramaki, S. (1963), Geology of Asama volcano, *J. Fac. Sci., Univ. Tokyo, Sec. 2*, **14**, 229–443.
- Aramaki, S. (1993), Geological map of Asama volcano, *Geological Map of Volcanoes*, scale 1:50,000, Geol. Surv. of Jpn., Tsukuba, Ibaraki.
- Arnórsson, S. (1995), Geothermal systems in Iceland: Structure and conceptual models—I. High-temperature areas, *Geothermics*, **24**(5–6), 561–602, doi:10.1016/0375-6505(95)00025-9.
- Aubert, M., and J.-C. Baubron (1988), Identification of a hidden thermal fissure in a volcanic terrain using a combination of hydrothermal convection indicators and soil-atmosphere analysis, *J. Volcanol. Geotherm. Res.*, **35**(3), 217–225, doi:10.1016/0377-0273(88)90018-2.
- Baldi, P., S. Bonvalot, P. Briole, and M. Marsella (2000), Digital photogrammetry and kinematic GPS for monitoring volcanic areas, *Geophys. J. Int.*, **142**(3), 801–811, doi:10.1046/j.1365-246x.2000.00194.x.
- Barde-Cabusson, S. et al. (2009), New geological insights and structural control on fluid circulation in La Fossa cone (Vulcano, Aeolian Islands, Italy), *J. Volcanol. Geotherm. Res.*, **185**(3), 231–245, doi:10.1016/j.jvolgeores.2009.06.002.

- Barry, P. H., D. R. Hilton, E. Füre, S. A. Halldórsson, and K. Grönvold (2014), Carbon isotope and abundance systematics of Icelandic geothermal gases, fluids and subglacial basalts with implications for mantle plume-related CO₂ fluxes, *Geochim. Cosmochim. Acta*, **134**, 74–99, doi:10.1016/j.gca.2014.02.038.
- Baubron, J. C., P. Allard, and J. P. Toutain (1990), Diffuse volcanic emissions of carbon dioxide from Vulcano Island, Italy, *Nature*, **344**(6261), 51–53, doi:10.1038/344051a0.
- Benavente, O., F. Tassi, F. Gutiérrez, O. Vaselli, F. Aguilera, and M. Reich (2013), Origin of fumarolic fluids from Tupungatito Volcano (Central Chile): Interplay between magmatic, hydrothermal, and shallow meteoric sources, *Bull. Volcanol.*, **75**, 746, doi:10.1007/s00445-013-0746-x.
- Bergfeld, D., W. C. Evans, J. F. Howle, and C. D. Farrar (2006), Carbon dioxide emissions from vegetation-kill zones around the resurgent dome of Long Valley caldera, eastern California, USA, *J. Volcanol. Geotherm. Res.*, **152**(1–2), 140–156, doi:10.1016/j.jvolgeores.2005.11.003.
- Bloomberg, S., C. Werner, C. Rissmann, A. Mazot, T. Horton, D. Gravley, B. Kennedy, and C. Oze (2014), Soil CO₂ emissions as a proxy for heat and mass flow assessment, Taupō Volcanic Zone, New Zealand, *Geochem. Geophys. Geosyst.*, **15**, 4885–4904, doi:10.1002/2014GC005327.
- Brombach, T., J. C. Hunziker, G. Chiodini, C. Cardellini, and L. Marini (2001), Soil diffuse degassing and thermal energy fluxes from the southern Lakki plain, Nisyros (Greece), *Geophys. Res. Lett.*, **28**(1), 69–72, doi:10.1029/2000GL008543.
- Brothelande, E., A. Finizola, A. Peltier, E. Delcher, J.-C. Komorowski, F. Di Gangi, G. Borgogno, M. Passarella, C. Trovato, and Y. Legendre (2014), Fluid circulation pattern inside La Soufrière volcano (Guadeloupe) inferred from combined electrical resistivity tomography, self-potential, soil temperature and diffuse degassing measurements, *J. Volcanol. Geotherm. Res.*, **288**, 105–122, doi:10.1016/j.jvolgeores.2014.10.007.
- Burton, M. R., G. M. Sawyer, and D. Granieri (2013), Deep carbon emissions from volcanoes, *Rev. Mineral. Geochem.*, **75**(1), 323–354, doi:10.2138/rmg.2013.75.11.
- Byrdina, S., D. Ramos, J. Vandemeulebrouck, P. Masias, A. Revil, A. Finizola, K. Gonzales Zuñiga, V. Cruz, Y. Antayhua, and O. Macedo (2013), Influence of the regional topography on the remote emplacement of hydrothermal systems with examples of Ticsani and Ubinas volcanoes, Southern Peru, *Earth Planet. Sci. Lett.*, **365**, 152–164, doi:10.1016/j.epsl.2013.01.018.
- Byrdina, S. et al. (2014), Relations between electrical resistivity, carbon dioxide flux, and self-potential in the shallow hydrothermal system of Solfatara (Phlegrean Fields, Italy), *J. Volcanol. Geotherm. Res.*, **283**, 172–182, doi:10.1016/j.jvolgeores.2014.07.010.

- Caliro, S., G. Chiodini, D. Galluzzo, D. Granieri, M. La Rocca, G. Saccorotti, and G. Ventura (2005), Recent activity of Nisyros volcano (Greece) inferred from structural, geochemical and seismological data, *Bull. Volcanol.*, **67**(4), 358–369, doi:10.1007/s00445-004-0381-7.
- Camarda, M., S. De Gregorio, R. Favara, and S. Gurrieri (2007), Evaluation of carbon isotope fractionation of soil CO₂ under an advective-diffusive regimen: A tool for computing the isotopic composition of unfractionated deep source, *Geochim. Cosmochim. Acta*, **71**(12), 3016–3027, doi:10.1016/j.gca.2007.04.002.
- Capasso, G., R. Favara, and S. Inguaggiato (1997), Chemical features and isotopic composition of gaseous manifestations on Vulcano Island, Aeolian Islands, Italy: An interpretative model of fluid circulation, *Geochim. Cosmochim. Acta*, **61**(16), 3425–3440, doi:10.1016/S0016-7037(97)00163-4.
- Caracausi, A., M. Paternoster, and P. M. Nuccio (2015), Mantle CO₂ degassing at Mt. Vulture volcano (Italy): Relationship between CO₂ outgassing of volcanoes and the time of their last eruption, *Earth Planet. Sci. Lett.*, **411**, 268–280, doi:10.1016/j.epsl.2014.11.049.
- Carapezza, M. L., and C. Federico (2000), The contribution of fluid geochemistry to the volcano monitoring of Stromboli, *J. Volcanol. Geotherm. Res.*, **95**(1–4), 227–245, doi:10.1016/S0377-0273(99)00128-6.
- Carapezza, M. L., S. Inguaggiato, L. Brusca, and M. Longo (2004), Geochemical precursors of the activity of an open-conduit volcano: The Stromboli 2002–2003 eruptive events, *Geophys. Res. Lett.*, **31**, L07620, doi:10.1029/2004GL019614.
- Carapezza, M. L., T. Ricci, M. Ranaldi, and L. Tarchini (2009), Active degassing structures of Stromboli and variations in diffuse CO₂ output related to the volcanic activity, *J. Volcanol. Geotherm. Res.*, **182**(3–4), 231–245, doi:10.1016/j.jvolgeores.2008.08.006.
- Carapezza, M. L., M. Ranaldi, A. Gattuso, N. M. Pagliuca, and L. Tarchini (2015), The sealing capacity of the cap rock above the Torre Alfina geothermal reservoir (Central Italy) revealed by soil CO₂ flux investigations, *J. Volcanol. Geotherm. Res.*, **291**, 25–34, doi:10.1016/j.jvolgeores.2014.12.011.
- Cardellini, C., G. Chiodini, F. Frondini, D. Granieri, J. Lewicki, and L. Peruzzi (2003a), Accumulation chamber measurements of methane fluxes: Application to volcanic-geothermal areas and landfills, *Appl. Geochem.*, **18**(1), 45–54, doi:10.1016/S0883-2927(02)00091-4.
- Cardellini, C., G. Chiodini, and F. Frondini (2003b), Application of stochastic simulation to CO₂ flux from soil: Mapping and quantification of gas release, *J. Geophys. Res.*, **108**(B9), 2425, doi:10.1029/2002JB002165.
- Castrillo, A., G. Casa, M. van Burgel, D. Tedesco, and L. Gianfrani (2004), First field determination

- of the $^{13}\text{C}/^{12}\text{C}$ isotope ratio in volcanic CO_2 by diode-laser spectrometry, *Opt. Express*, **12**(26), 6515–6523, doi:10.1364/OPEX.12.006515.
- Cellura, D., V. Stagno, M. Camarda, and M. Valenza (2014), Diffuse soil CO_2 degassing from Linosa island, *Annals of Geophysics*, **57**(3), S0329, doi:10.4401/ag-6476.
- Cheng, W. (1996), Measurement of rhizosphere respiration and organic matter decomposition using natural ^{13}C , *Plant Soil*, **183**(2), 263–268, doi:10.1007/BF00011441.
- Chiodini, G., and F. Frondini (2001), Carbon dioxide degassing from the Albani Hills volcanic regions, Central Italy, *Chem. Geol.*, **177**(1–2), 67–83, doi:10.1016/S0009-2541(00)00382-X.
- Chiodini, G., and L. Marini (1998), Hydrothermal gas equilibria: The $\text{H}_2\text{O}-\text{H}_2-\text{CO}_2-\text{CO}-\text{CH}_4$ system, *Geochim. Cosmochim. Acta*, **62**(15), 2673–2687, doi:10.1016/S0016-7037(98)00181-1.
- Chiodini, G., F. Frondini, and B. Raco (1996), Diffuse emission of CO_2 from the Fossa crater, Vulcano Island (Italy), *Bull. Volcanol.*, **58**(1), 41–50, doi:10.1007/s004450050124.
- Chiodini, G., R. Cioni, M. Guidi, B. Raco, and L. Marini (1998), Soil CO_2 flux measurements in volcanic and geothermal areas, *Appl. Geochem.*, **13**(5), 543–552, doi:10.1016/S0883-2927(97)00076-0.
- Chiodini, G., F. Frondini, D. M. Kerrick, J. Rogie, F. Parello, L. Peruzzi, and A. R. Zanzari (1999), Quantification of deep CO_2 fluxes from Central Italy. Examples of carbon balance for regional aquifers and of soil diffuse degassing, *Chem. Geol.*, **159**(1–4), 205–222, doi:10.1016/S0009-2541(99)00030-3.
- Chiodini, G., F. Frondini, C. Cardellini, D. Granieri, L. Marini, and G. Ventura (2001), CO_2 degassing and energy release at Solfatara volcano, Campi Flegrei, Italy, *J. Geophys. Res.*, **106**(B8), 16213–16221, doi:10.1029/2001JB000246.
- Chiodini, G., D. Granieri, R. Avino, S. Caliro, A. Costa, and C. Werner (2005), Carbon dioxide diffuse degassing and estimation of heat release from volcanic and hydrothermal systems, *J. Geophys. Res.*, **110**, B08204, doi:10.1029/2004JB003542.
- Chiodini, G., A. Baldini, F. Barberi, M. L. Carapezza, C. Cardellini, F. Frondini, D. Granieri, and M. Ranaldi (2007a), Carbon dioxide degassing at Latera caldera (Italy): Evidence of geothermal reservoir and evaluation of its potential energy, *J. Geophys. Res.*, **112**, B12204, doi:10.1029/2006JB004896.
- Chiodini, G., G. Vilardo, V. Augusti, D. Granieri, S. Caliro, C. Minopoli, and C. Terranova (2007b), Thermal monitoring of hydrothermal activity by permanent infrared automatic stations: Results obtained at Solfatara di Pozzuoli, Campi Flegrei (Italy), *J. Geophys. Res.*, **112**, B12206, doi:10.1029/2007JB005140.
- Chiodini, G., S. Caliro, C. Cardellini, R. Avino, D. Granieri, and A. Schmidt (2008), Carbon isotopic

- composition of soil CO₂ efflux, a powerful method to discriminate different sources feeding soil CO₂ degassing in volcanic-hydrothermal areas, *Earth Planet. Sci. Lett.*, **274**(3–4), 372–379, doi:10.1016/j.epsl.2008.07.051.
- Chiodini, G., D. Granieri, R. Avino, S. Caliro, A. Costa, C. Minopoli, and G. Vilardo (2010), Non-volcanic CO₂ Earth degassing: Case of Mefite d’Ansanto (southern Apennines), Italy, *Geophys. Res. Lett.*, **37**, L11303, doi:10.1029/2010GL042858.
- Chiodini, G., S. Caliro, A. Aiuppa, R. Avino, D. Granieri, R. Moretti, and F. Parello (2011), First ¹³C/¹²C isotopic characterisation of volcanic plume CO₂, *Bull. Volcanol.*, **73**(5), 531–542, doi:10.1007/s00445-010-0423-2.
- Chiodini, G., C. Cardellini, M. C. Lamberti, M. Agosto, A. Caselli, C. Liccioli, G. Tamburello, F. Tassi, O. Vaselli, and S. Caliro (2015), Carbon dioxide diffuse emission and thermal energy release from hydrothermal systems at Copahue–Caviahue Volcanic Complex (Argentina), *J. Volcanol. Geotherm. Res.*, **304**, 294–303, doi:10.1016/j.jvolgeores.2015.09.007.
- Conrad, O., B. Bechtel, M. Bock, H. Dietrich, E. Fischer, L. Gerlitz, J. Wehberg, V. Wichmann, and J. Böhner (2015), System for Automated Geoscientific Analyses (SAGA) v. 2.1.4, *Geosci. Model Dev.*, **8**, 1991–2007, doi:10.5194/gmd-8-1991-2015.
- Craig, H. (1953), The geochemistry of the stable carbon isotopes, *Geochim. Cosmochim. Acta*, **3**(2–3), 53–92, doi:10.1016/0016-7037(53)90001-5.
- Cruz, J. V., R. M. Coutinho, M. R. Carvalho, N. Oskarsson, and S. R. Gislason (1999), Chemistry of waters from Furnas volcano, São Miguel, Azores: Fluxes of volcanic carbon dioxide and leached material, *J. Volcanol. Geotherm. Res.*, **92**(1–2), 151–167, doi:10.1016/S0377-0273(99)00073-6.
- D’Alessandro, W., S. Bellomo, L. Brusca, J. Fiebig, M. Longo, M. Martelli, G. Pecoraino, and F. Salerno (2009), Hydrothermal methane fluxes from the soil at Pantelleria island (Italy), *J. Volcanol. Geotherm. Res.*, **187**(3–4), 147–157, doi:10.1016/j.jvolgeores.2009.08.018.
- Deutsch, C. V., and A. G. Journel (1998), *GSLIB: Geostatistical Software Library and User’s Guide*, 2nd ed., Oxford University Press, New York.
- Diggle, P. J., and P. J. Ribeiro Jr. (2007), *Model-based geostatistics*, Springer, New York.
- Dionis, S. M. et al. (2015a), Diffuse CO₂ degassing and volcanic activity at Cape Verde islands, West Africa, *Earth Planets Space*, **67**, 48, doi:10.1186/s40623-015-0219-x.
- Dionis, S. M. et al. (2015b), Diffuse volcanic gas emission and thermal energy release from the summit crater of Pico do Fogo, Cape Verde, *Bull. Volcanol.*, **77**, 10, doi:10.1007/s00445-014-0897-4.
- Doukas, M. P., and K. A. McGee (2007), A compilation of gas emission-rate data from volcanoes

of Cook Inlet (Spurr, Crater Peak, Redoubt, Iliamna, and Augustine) and Alaska Peninsula (Douglas, Fourpeaked, Griggs, Mageik, Martin, Peulik, Ukinrek Maars, and Veniaminof), Alaska, from 1995–2006, *U. S. Geol. Surv. Open-File Rep. 2007-1400*, U. S. Geol. Surv., Reston, Virginia.

- Evans, W. C., M. L. Sorey, A. C. Cook, B. M. Kennedy, D. L. Shuster, E. M. Colvard, L. D. White, and M. A. Huebner (2002), Tracing and quantifying magmatic carbon discharge in cold groundwaters: lessons learned from Mammoth Mountain, USA, *J. Volcanol. Geotherm. Res.*, **114**(3–4), 291–312, doi:10.1016/S0377-0273(01)00268-2.
- Evans, W. C., D. Bergfeld, R. G. McGimsey, and A. G. Hunt (2009), Diffuse gas emissions at the Ukinrek Maars, Alaska: Implications for magmatic degassing and volcanic monitoring, *Appl. Geochem.*, **24**(4), 527–535, doi:10.1016/j.apgeochem.2008.12.007.
- Favara, R., S. Giammanco, S. Inguaggiato, and G. Pecoraino (2001), Preliminary estimate of CO₂ output from Pantelleria Island volcano (Sicily, Italy): Evidence of active mantle degassing, *Appl. Geochem.*, **16**(7–8), 883–894, doi:10.1016/S0883-2927(00)00055-X.
- Finizola, A., F. Sortino, J. F. Lénat, M. Aubert, M. Ripepe, and M. Valenza (2003), The summit hydrothermal system of Stromboli. New insights from self-potential, temperature, CO₂ and fumarolic fluid measurements, with structural and monitoring implications, *Bull. Volcanol.*, **65**, 486–504, doi:10.1007/s00445-003-0276-z.
- Finizola, A., A. Revil, E. Rizzo, S. Piscitelli, T. Ricci, J. Morin, B. Angeletti, L. Mocochain, and F. Sortino (2006), Hydrogeological insights at Stromboli volcano (Italy) from geoelectrical, temperature, and CO₂ soil degassing investigations, *Geophys. Res. Lett.*, **33**, L17304, doi:10.1029/2006GL026842.
- Finizola, A., M. Aubert, A. Revil, C. Schütze, and F. Sortino (2009), Importance of structural history in the summit area of Stromboli during the 2002–2003 eruptive crisis inferred from temperature, soil CO₂, self-potential, and electrical resistivity tomography, *J. Volcanol. Geotherm. Res.*, **183**(3–4), 213–227, doi:10.1016/j.jvolgeores.2009.04.002.
- Finizola, A. et al. (2010), Adventive hydrothermal circulation on Stromboli volcano (Aeolian Islands, Italy) revealed by geophysical and geochemical approaches: Implications for general fluid flow models on volcanoes, *J. Volcanol. Geotherm. Res.*, **196**(1–2), 111–119, doi:10.1016/j.jvolgeores.2010.07.022.
- Fischer, T. P. (2008), Fluxes of volatiles (H₂O, CO₂, N₂, Cl, F) from arc volcanoes, *Geochem. J.*, **42**, 21–38, doi:10.2343/geochemj.42.21.
- Fischer, T. P., and T. M. Lopez (2016), First airborne samples of a volcanic plume for δ¹³C of CO₂ determinations, *Geophys. Res. Lett.*, **43**(7), 3272–3279, doi:10.1002/2016GL068499.

- Fischer, T. P., W. F. Giggenbach, Y. Sano, and S. N. Williams (1998), Fluxes and sources of volatiles discharged from Kudryavy, a subduction zone volcano, Kurile Islands, *Earth Planet. Sci. Lett.*, **160**, 81–96, doi:10.1016/S0012-821X(98)00086-7.
- Fischer, T. P. et al. (2015), Temporal variations in fumarole gas chemistry at Poás volcano, Costa Rica, *J. Volcanol. Geotherm. Res.*, **294**, 56–70, doi:10.1016/j.jvolgeores.2015.02.002.
- Fiske, R. S., and E. D. Jackson (1972), Orientation and growth of Hawaiian volcanic rifts: The effect of regional structure and gravitational stresses, *Proc. R. Soc. A*, **329**(1578), 299–326, doi:10.1098/rspa.1972.0115.
- Fridriksson, T., B. R. Kristjánsson, H. Ármannsson, E. Margrétardóttir, S. Ólafsdóttir, and G. Chiodini (2006), CO₂ emissions and heat flow through soil, fumaroles, and steam heated mud pools at the Reykjanes geothermal area, SW Iceland, *Appl. Geochem.*, **21**(9), 1551–1569, doi:10.1016/j.apgeochem.2006.04.006.
- Fronchini, F., G. Chiodini, S. Caliro, C. Cardellini, D. Granieri, and G. Ventura (2004), Diffuse CO₂ degassing at Vesuvio, Italy, *Bull. Volcanol.*, **66**, 642–651, doi:10.1007/s00445-004-0346-x.
- Gerlach, T. M., and B. E. Taylor (1990), Carbon isotope constraints on degassing of carbon dioxide from Kilauea Volcano, *Geochim. Cosmochim. Acta*, **54**(7), 2051–2058, doi:10.1016/0016-7037(90)90270-U.
- Geshi, N. (2009), Asymmetric growth of collapsed caldera by oblique subsidence during the 2000 eruption of Miyakejima, Japan, *Earth Planet. Sci. Lett.*, **280**(1–4), 149–158, doi:10.1016/j.epsl.2009.01.027.
- Giammanco, S., G. Melián, M. Neri, P. A. Hernández, F. Sortino, J. Barrancos, M. López, G. Pecoraino, and N. M. Pérez (2016), Active tectonic features and structural dynamics of the summit area of Mt. Etna (Italy) revealed by soil CO₂ and soil temperature surveying, *J. Volcanol. Geotherm. Res.*, **311**, 79–98, doi:10.1016/j.jvolgeores.2016.01.004.
- Giggenbach, W. F. (1980), Geothermal gas equilibria, *Geochim. Cosmochim. Acta*, **44**(12), 2021–2032, doi:10.1016/0016-7037(80)90200-8.
- Giggenbach, W. F. (1987), Redox processes governing the chemistry of fumarolic gas discharges from White Island, New Zealand, *Appl. Geochem.*, **2**, 143–161, doi:10.1016/0883-2927(87)90030-8.
- Giggenbach, W. F. (1995), Variations in the chemical and isotopic composition of fluids discharged from the Taupo Volcanic Zone, New Zealand, *J. Volcanol. Geotherm. Res.*, **68**(1–3), 89–116, doi:10.1016/0377-0273(95)00009-J.
- Giggenbach, W. F. (1996), Chemical composition of volcanic gases, in *Monitoring and Mitigation of Volcano Hazards*, edited by R. Scarpa and R. I. Tilling, pp. 221–256, Springer-Verlag, Berlin,

Heidelberg.

- Giggenbach, W. F. (1997), Relative importance of thermodynamic and kinetic processes in governing the chemical and isotopic composition of carbon gases in high-heatflow sedimentary basins, *Geochim. Cosmochim. Acta*, **61**(17), 3763–3785, doi:10.1016/S0016-7037(97)00171-3.
- Goff, F., S. P. Love, R. G. Warren, D. Counce, J. Obenholzner, C. Siebe, and S. C. Schmidt (2001), Passive infrared remote sensing evidence for large, intermittent CO₂ emissions at Popocatepetl volcano, Mexico, *Chem. Geol.*, **177**(1–2), 133–156, doi:10.1016/S0009-2541(00)00387-9.
- Granieri, D. et al. (2013), Level of carbon dioxide diffuse degassing from the ground of Vesuvio: Comparison between extensive surveys and inferences on the gas source, *Annals of Geophysics*, **56**(4), S0449, doi:10.4401/ag-6455.
- Granieri, D., G. Chiodini, R. Avino, and S. Caliro (2014), Carbon dioxide emission and heat release estimation for Pantelleria Island (Sicily, Italy), *J. Volcanol. Geotherm. Res.*, **275**, 22–33, doi:10.1016/j.jvolgeores.2014.02.011.
- Gudmundsson, A., I. Fjeldskaar, and S. L. Brenner (2002), Propagation pathways and fluid transport of hydrofractures in jointed and layered rocks in geothermal fields, *J. Volcanol. Geotherm. Res.*, **116**(3–4), 257–278, doi:10.1016/S0377-0273(02)00225-1.
- Hanson, M. C., C. Oze, and T. W. Horton (2014), Identifying blind geothermal systems with soil CO₂ surveys, *Appl. Geochem.*, **50**, 106–114, doi:10.1016/j.apgeochem.2014.08.009.
- Hernández, P. A., N. M. Pérez, J. M. Salazar, S. Nakai, K. Notsu, and H. Wakita (1998), Diffuse emission of carbon dioxide, methane, and helium-3 from Teide Volcano, Tenerife, Canary Islands, *Geophys. Res. Lett.*, **25**(17), 3311–3314, doi:10.1029/98GL02561.
- Hernández, P. A., K. Notsu, J. M. L. Salazar, T. Mori, G. Natale, H. Okada, G. Virgili, Y. Shimoike, M. Sato, and N. M. Pérez (2001a), Carbon dioxide degassing by advective flow from Usu volcano, Japan, *Science*, **292**(5514), 83–86, doi:10.1126/science.1058450.
- Hernández, P. A., J. M. L. Salazar, Y. Shimoike, T. Mori, K. Notsu, and N. M. Pérez (2001b), Diffuse emission of CO₂ from Miyakejima volcano, Japan, *Chem. Geol.*, **177**, 175–185, doi:10.1016/S0009-2541(00)00390-9.
- Hernández, P. A., K. Notsu, H. Okada, T. Mori, M. Sato, F. Barahona, and N. M. Pérez (2006), Diffuse emission of CO₂ from Showa-Shinzan, Hokkaido, Japan: A sign of volcanic dome degassing, *Pure Appl. Geophys.*, **163**(4), 869–881, doi:10.1007/s00024-006-0038-x.
- Hernández, P. A. et al. (2012), Diffuse volcanic degassing and thermal energy release from Hengill volcanic system, Iceland, *Bull. Volcanol.*, **74**(10), 2435–2448, doi:10.1007/s00445-012-0673-2.

- Hernández, P. A. et al. (2015), Contribution of CO₂ and H₂S emitted to the atmosphere by plume and diffuse degassing from volcanoes: the Etna volcano case study, *Surv. Geophys.*, **36**(3), 327–349, doi:10.1007/s10712-015-9321-7.
- Hernández Perez, P., K. Notsu, M. Tsurumi, T. Mori, M. Ohno, Y. Shimoike, J. Salazar, and N. Pérez (2003), Carbon dioxide emissions from soils at Hakkoda, north Japan, *J. Geophys. Res.*, **108**(B4), 2210, doi:10.1029/2002JB001847.
- Hilton, D. R. (1996), The helium and carbon isotope systematics of a continental geothermal system: Results from monitoring studies at Long Valley caldera (California, U.S.A.), *Chem. Geol.*, **127**(4), 269–295, doi:10.1016/0009-2541(95)00134-4.
- Hilton, D. R., C. J. Ramírez, R. Mora-Amador, T. P. Fischer, E. Füre, P. H. Barry, and A. M. Shaw (2010), Monitoring of temporal and spatial variations in fumarole helium and carbon dioxide characteristics at Poás and Turrialba Volcanoes, Costa Rica (2001–2009), *Geochem. J.*, **44**(5), 431–440, doi:10.2343/geochemj.1.0085.
- Hoefs, J. (2004), *Stable Isotope Geochemistry*, 5th ed., Springer, Berlin, Heidelberg.
- Hutchison, W., T. A. Mather, D. M. Pyle, J. Biggs, and G. Yirgu (2015), Structural controls on fluid pathways in an active rift system: A case study of the Aluto volcanic complex, *Geosphere*, **11**(3), 1–21, doi:10.1130/GES01119.1.
- Ilyinskaya, E. et al. (2015), Degassing regime of Hekla volcano 2012–2013, *Geochim. Cosmochim. Acta*, **159**, 80–99, doi:10.1016/j.gca.2015.01.013.
- Inguaggiato, S., A. L. Martin-Del Pozzo, A. Aguayo, G. Capasso, and R. Favara (2005), Isotopic, chemical and dissolved gas constraints on spring water from Popocatepetl volcano (Mexico): evidence of gas-water interaction between magmatic component and shallow fluids, *J. Volcanol. Geotherm. Res.*, **141**(1–2), 91–108, doi:10.1016/j.jvolgeores.2004.09.006.
- Inguaggiato, S., A. Mazot, I. S. Diliberto, C. Inguaggiato, P. Madonia, D. Rouwet, and F. Vita (2012), Total CO₂ output from Vulcano island (Aeolian Islands, Italy), *Geochem. Geophys. Geosyst.*, **13**(2), doi:10.1029/2011GC003920.
- Inguaggiato, S., M. P. Jácome Paz, A. Mazot, H. Delgado Granados, C. Inguaggiato, and F. Vita (2013), CO₂ output discharged from Stromboli Island (Italy), *Chem. Geol.*, **339**, 52–60, doi:10.1016/j.chemgeo.2012.10.008.
- Isaia, R., S. Vitale, M. G. Di Giuseppe, E. Iannuzzi, F. D. Tramparulo, and A. Troiano (2015), Stratigraphy, structure, and volcano-tectonic evolution of Solfatara maar-diatreme (Campi Flegrei, Italy), *Bull. Geol. Soc. Am.*, **127**(9–10), 1485–1504, doi:10.1130/B31183.1.
- Issa et al. (2014), Gas emission from diffuse degassing structures (DDS) of the Cameroon volcanic line (CVL): Implications for the prevention of CO₂-related hazards, *J. Volcanol. Geotherm.*

Res., **283**, 82–93, doi:10.1016/j.jvolgeores.2014.07.001.

- Jácome Paz, M. P., S. Inguaggiato, Y. Taran, F. Vita, and G. Pecoraino (2016), Carbon dioxide emissions from Specchio di Venere, Pantelleria, Italy, *Bull. Volcanol.*, **78**, 29, doi:10.1007/s00445-016-1023-6.
- Jaffe, L. A., D. R. Hilton, T. P. Fischer, and U. Hartono (2004), Tracing magma sources in an arc-arc collision zone: Helium and carbon isotope and relative abundance systematics of the Sangihe Arc, Indonesia, *Geochem. Geophys. Geosyst.*, **5**(4), Q04J10, doi:10.1029/2003GC000660.
- Japan Meteorological Agency (2013), *National catalogue of the active volcanoes in Japan*, 4th ed., edited by Japan Meteorological Agency and Volcanological Society of Japan, Japan Meteorological Agency, Tokyo.
- Japan Meteorological Agency (2015a), Volcanic activity of Asama volcano from June to October 2015, *Rep. Coord. Comm. Pred. Volcanic Erupt.*, **133**(5), 42–89 (in Japanese).
- Japan Meteorological Agency (2015b), *Volcanic activity of Asama Volcano in 2015*, Japan Meteorol. Agency, Tokyo, Japan (in Japanese).
- Japan Meteorological Agency (2016), *SO₂ emission rates from Asama volcano*, Available from: http://www.data.jma.go.jp/svd/vois/data/tokyo/306_Asamayama/306_So2emission.htm (Accessed 13 December 2016)
- Jenness, J. (2006), *Topographic Position Index (tpi_jen.avx) extension for ArcView 3.x, v. 1.2*, Jenness Enterprises. Available from: <http://www.jennessent.com/arcview/tpi.htm>
- Jitsufuchi, T. (2011), Brightness temperature distributions in Asama volcano crater acquired using ARTS, *Tech. Note Natl. Res. Inst. Earth Sci. Disaster Prev.* **355**, Natl. Res. Inst. Earth Sci. Disaster Resilience, Tsukuba, Ibaraki, Japan (in Japanese with English abstract).
- Jolie, E., M. Klinkmueller, and I. Moeck (2015), Diffuse surface emanations as indicator of structural permeability in fault-controlled geothermal systems, *J. Volcanol. Geotherm. Res.*, **290**, 97–113, doi:10.1016/j.jvolgeores.2014.11.003.
- Kagoshima, T., Y. Sano, N. Takahata, T. Maruoka, T. P. Fischer, and K. Hattori (2015), Sulphur geodynamic cycle, *Sci. Rep.*, **5**, 8330, doi:10.1038/srep08330.
- Kagoshima, T. et al. (2016), Spatial and temporal variations of gas geochemistry at Mt. Ontake, Japan, *J. Volcanol. Geotherm. Res.*, **325**, 179–188, doi:10.1016/j.jvolgeores.2016.06.013.
- Kämpf, H., K. Bräuer, J. Schumann, K. Hahne, and G. Strauch (2013), CO₂ discharge in an active, non-volcanic continental rift area (Czech Republic): Characterisation ($\delta^{13}\text{C}$, $^3\text{He}/^4\text{He}$) and quantification of diffuse and vent CO₂ emissions, *Chem. Geol.*, **339**, 71–83, doi:10.1016/j.chemgeo.2012.08.005.

- Kazahaya, K., H. Shinohara, and G. Saito (1994), Excessive degassing of Izu-Oshima volcano: magma convection in a conduit, *Bull. Volcanol.*, **56**(3), 207–216, doi:10.1007/BF00279605.
- Kazahaya, R., T. Mori, M. Takeo, T. Ohminato, T. Urabe, and Y. Maeda (2011), Relation between single very-long-period pulses and volcanic gas emissions at Mt. Asama, Japan, *Geophys. Res. Lett.*, **38**, L11307, doi:10.1029/2011GL047555.
- Kazahaya, R., Y. Aoki, and H. Shinohara (2015a), Budget of shallow magma plumbing system at Asama Volcano, Japan, revealed by ground deformation and volcanic gas studies, *J. Geophys. Res. Solid Earth*, **120**(5), 2961–2973, doi:10.1002/2014JB011715.
- Kazahaya, R., Y. Maeda, T. Mori, H. Shinohara, and M. Takeo (2015b), Changes to the volcanic outgassing mechanism and very-long-period seismicity from 2007 to 2011 at Mt. Asama, Japan, *Earth Planet. Sci. Lett.*, **418**, 1–10, doi:10.1016/j.epsl.2015.02.034.
- Kazama, T., S. Okubo, T. Sugano, S. Matsumoto, W. Sun, Y. Tanaka, and E. Koyama (2015), Absolute gravity change associated with magma mass movement in the conduit of Asama Volcano (Central Japan), revealed by physical modeling of hydrological gravity disturbances, *J. Geophys. Res. Solid Earth*, **120**, 1263–1287, doi:10.1002/2014JB011563.
- Kita, I., K. Nagao, S. Taguchi, K. Nitta, and H. Hasegawa (1993), Emission of magmatic He with different $^3\text{He}/^4\text{He}$ ratios from the Unzen volcanic area, Japan, *Geochem. J.*, **27**(4–5), 251–259, doi:10.2343/geochemj.27.251.
- Koepenick, K. W., S. L. Brantley, J. M. Thompson, G. L. Rowe, A. A. Nyblade, and C. Moshy (1996), Volatile emissions from the crater and flank of Oldoinyo Lengai volcano, Tanzania, *J. Geophys. Res.*, **101**(B6), 13819–13830, doi:10.1029/96JB00173.
- Koyama, T. et al. (2013), Preliminary report of wide band MT survey in the summit area of Mt. Asama, Japan, paper presented at Jpn. Geosci. Union Meeting, SVC48-P09 (in Japanese with English abstract), Chiba, Japan.
- Lan, T. F., T. F. Yang, H.-F. Lee, Y.-G. Chen, C.-H. Chen, S.-R. Song, and S. Tsao (2007), Compositions and flux of soil gas in Liu-Huang-Ku hydrothermal area, northern Taiwan, *J. Volcanol. Geotherm. Res.*, **165**(1–2), 32–45, doi:10.1016/j.jvolgeores.2007.04.015.
- Lee, H., J. D. Muirhead, T. P. Fischer, C. J. Ebinger, S. A. Kattenhorn, Z. D. Sharp, and G. Kianji (2016), Massive and prolonged deep carbon emissions associated with continental rifting, *Nat. Geosci.*, **9**, 145–149, doi:10.1038/NGEO2622.
- Lewicki, J. L., T. Fischer, and S. N. Williams (2000), Chemical and isotopic compositions of fluids at Cumbal Volcano, Colombia: Evidence for magmatic contribution, *Bull. Volcanol.*, **62**(4–5), 347–361, doi:10.1007/s004450000100.
- Lewicki, J. L., C. Connor, K. St-Amand, J. Stix, and W. Spinner (2003), Self-potential, soil CO₂

- flux, and temperature on Masaya volcano, Nicaragua, *Geophys. Res. Lett.*, **30**(15), 1817, doi:10.1029/2003GL017731.
- Lewicki, J. L., D. Bergfeld, C. Cardellini, G. Chiodini, D. Granieri, N. Varley, and C. Werner (2005), Comparative soil CO₂ flux measurements and geostatistical estimation methods on Masaya volcano, Nicaragua, *Bull. Volcanol.*, **68**(1), 76–90, doi:10.1007/s00445-005-0423-9.
- Liotta, M., A. Paonita, A. Caracausi, M. Martelli, A. Rizzo, and R. Favara (2010), Hydrothermal processes governing the geochemistry of the crater fumaroles at Mount Etna volcano (Italy), *Chem. Geol.*, **278**(1–2), 92–104, doi:10.1016/j.chemgeo.2010.09.004.
- Lowenstern, J. B., D. Bergfeld, W. C. Evans, and A. G. Hunt (2015), Origins of geothermal gases at Yellowstone, *J. Volcanol. Geotherm. Res.*, **302**, 87–101, doi:10.1016/j.jvolgeores.2015.06.010.
- Lyon, G. L., and J. R. Hulston (1984), Carbon and hydrogen isotopic compositions of New Zealand geothermal gases, *Geochim. Cosmochim. Acta*, **48**(6), 1161–1171, doi:10.1016/0016-7037(84)90052-8.
- Maeda, Y., and M. Takeo (2011), Very-long-period pulses at Asama volcano, central Japan, inferred from dense seismic observations, *Geophys. J. Int.*, **185**(1), 265–282, doi:10.1111/j.1365-246X.2011.04938.x.
- Maeno, F., Y. Suzuki, S. Nakada, E. Koyama, T. Kaneko, T. Fujii, J. Miyamura, S. Onizawa, and M. Nagai (2010), Course and ejecta of the eruption of Asama volcano on 2 February 2009, *Bull. Volcanol. Soc. Jpn.*, **55**(3), 147–154 (in Japanese with English abstract).
- Marrero, R., D. L. López, P. A. Hernández, and N. M. Pérez (2008), Carbon dioxide discharged through the Las Cañadas aquifer, Tenerife, Canary Islands, *Pure Appl. Geophys.*, **165**(1), 147–172, doi:10.1007/s00024-007-0287-3.
- Martelli, M., A. Caracausi, A. Paonita, and A. Rizzo (2008), Geochemical variations of air-free crater fumaroles at Mt Etna: New inferences for forecasting shallow volcanic activity, *Geophys. Res. Lett.*, **35**, L21302, doi:10.1029/2008GL035118.
- Marty, B., and W. F. Giggenbach (1990), Major and rare gases at White Island volcano, New Zealand: Origin and flux of volatiles, *Geophys. Res. Lett.*, **17**(3), 247–250, doi:10.1029/GL017i003p00247.
- Marty, B., and I. N. Tolstikhin (1998), CO₂ fluxes from mid-ocean ridges, arcs and plumes, *Chem. Geol.*, **145**(3–4), 233–248, doi:10.1016/S0009-2541(97)00145-9.
- Marty, B., V. Meynier, E. Nicolini, E. Greisshaber, and J. P. Toutain (1993), Geochemistry of gas emanations: A case study of the Réunion Hot Spot, Indian Ocean, *Appl. Geochem.*, **8**, 141–152, doi:10.1016/0883-2927(93)90030-K.
- Mazot, A., D. Rouwet, Y. Taran, S. Inguaggiato, and N. Varley (2011), CO₂ and He degassing at El

- Chichón volcano, Chiapas, Mexico: Gas flux, origin and relationship with local and regional tectonics, *Bull. Volcanol.*, **73**(4), 423–441, doi:10.1007/s00445-010-0443-y.
- Mazot, A., E. R. Smid, L. Schwendenmann, H. Delgado-Granados, and J. Lindsay (2013), Soil CO₂ flux baseline in an urban monogenetic volcanic field: The Auckland Volcanic Field, New Zealand, *Bull. Volcanol.*, **75**, 757, doi:10.1007/s00445-013-0757-7.
- McGuire, W. J., and A. D. Pullen (1989), Location and orientation of eruptive fissures and feederdykes at Mount Etna; influence of gravitational and regional tectonic stress regimes, *J. Volcanol. Geotherm. Res.*, **38**(3–4), 325–344, doi:10.1016/0377-0273(89)90046-2.
- Melián, G. et al. (2012), A magmatic source for fumaroles and diffuse degassing from the summit crater of Teide Volcano (Tenerife, Canary Islands): A geochemical evidence for the 2004–2005 seismic-volcanic crisis, *Bull. Volcanol.*, **74**(6), 1465–1483, doi:10.1007/s00445-012-0613-1.
- Melián, G., P. A. Hernández, E. Padrón, N. M. Pérez, J. Barrancos, G. Padilla, S. Dionis, F. Rodríguez, D. Calvo, and D. Nolasco (2014), Spatial and temporal variations of diffuse CO₂ degassing at El Hierro volcanic system: Relation to the 2011–2012 submarine eruption, *J. Geophys. Res. Solid Earth*, **119**, 6976–6991, doi:10.1002/2014JB011013.
- Minakami, T. (1960), Fundamental research for predicting volcanic eruptions (Part 1), *Bull. Earthq. Res. Inst., Univ. Tokyo*, **38**, 497–544.
- Moffat, A. J., T. Nakahara, T. Akitomo, and L. Langal (1972), Mt. Asama volcano SO₂, *Barringer Research Technical Paper*, **62**.
- Mori, T., and K. Notsu (2005), Remote FT-IR measurements of volcanic gas chemistry in the plume of Asama volcano, *Bull. Volcanol. Soc. Jpn.*, **50**(6), 567–574 (in Japanese with English abstract).
- Mori, T., J. Hirabayashi, K. Kazahaya, T. Mori, M. Ohwada, M. Miyashita, H. Iino, and Y. Nakahori (2007), A compact ultraviolet spectrometer system (COMPUSS) for monitoring volcanic SO₂ emission: Validation and preliminary observation, *Bull. Volcanol. Soc. Jpn.*, **52**(2), 105–112.
- Mori, T., H. Shinohara, K. Kazahaya, J. Hirabayashi, T. Matsushima, T. Mori, M. Ohwada, M. Odai, H. Iino, and M. Miyashita (2013), Time-averaged SO₂ fluxes of subduction-zone volcanoes: Example of a 32-year exhaustive survey for Japanese volcanoes, *J. Geophys. Res. Atmos.*, **118**, 8662–8674, doi:10.1002/jgrd.50591.
- Morita, M., T. Mori, R. Kazahaya, and H. Tsuji (2016), Diffuse carbon dioxide emissions from hidden subsurface structures at Asama volcano, Japan, *Bull. Volcanol.*, **78**(3), 17, doi:10.1007/s00445-016-1008-5.
- Murakami, M. (2005), Magma plumbing system of the Asama volcano inferred from continuous

- measurements of GPS, *Bull. Volcanol. Soc. Jpn.*, **50**(5), 347–361 (in Japanese with English abstract).
- Murase, M. et al. (2007), Time-dependent model for volume changes in pressure sources at Asama volcano, central Japan due to vertical deformations detected by precise leveling during 1902–2005, *J. Volcanol. Geotherm. Res.*, **164**, 54–75, doi:10.1016/j.jvolgeores.2007.04.001.
- Nagaoka, Y., K. Nishida, Y. Aoki, M. Takeo, and T. Ohminato (2012), Seismic imaging of magma chamber beneath an active volcano, *Earth Planet. Sci. Lett.*, **333–334**, 1–8, doi:10.1016/j.epsl.2012.03.034.
- Nakada, S., M. Yoshimoto, E. Koyama, H. Tsuji, and T. Urabe (2005), Comparative study of the 2004 eruption with old eruptions at Asama volcano and the activity evaluation, *Bull. Volcanol. Soc. Jpn.*, **50**(5), 303–313 (in Japanese with English abstract).
- Natale, G., P. Hernández, T. Mori, and K. Notsu (2000), Pressure gradient measurements in volcanic diffuse gas emanations, *Geophys. Res. Lett.*, **27**(24), 3985–3987, doi:10.1029/2000GL008540.
- Newhall, C. G., and S. Self (1982), The Volcanic Explosivity Index (VEI): An estimate of explosive magnitude for historical volcanism, *J. Geophys. Res.*, **87**(C2), 1231–1238, doi:10.1029/JC087iC02p01231.
- Nogami, K., S. Onizawa, and J. Hirabayashi (2008), Geochemical observation on the 2004 eruption of Asama volcano through analysis of water-soluble components on the ash, *Bull. Volcanol. Soc. Jpn.*, **53**(2), 69–77 (in Japanese with English abstract).
- Noguchi, K. (1935), Geochemical investigations of volcanoes in Japan. I: Studies on the gases and the spring waters of Volcano Asama. I, *Nippon Kagaku Kaishi*, **56**(12), 1495–1510 (in Japanese), doi:10.1246/nikkashi1921.56.12_1495.
- Noguchi, K. (1936), Geochemical investigations of volcanoes in Japan. IV: Studies on the gases and the spring waters of Volcano Asama. II, *Nippon Kagaku Kaishi*, **57**(9), 920–928 (in Japanese), doi:10.1246/nikkashi1921.57.9_920.
- Noguchi, K. (1938a), Geochemical investigations of volcanoes in Japan. XI: Studies on the gases and the spring waters of Volcano Asama. III, *Nippon Kagaku Kaishi*, **59**(4), 521–543 (in Japanese), doi:10.1246/nikkashi1921.59.521.
- Noguchi, K. (1938b), Geochemical investigations of volcanoes in Japan. XII: Studies on the gases and the spring waters of Volcano Asama. IV, *Nippon Kagaku Kaishi*, **59**(6), 902–908 (in Japanese), doi:10.1246/nikkashi1921.59.902.
- Noguchi, K., and H. Kamiya (1963), Prediction of volcanic eruption by measuring the chemical composition and amounts of gases, *Bull. Volcanol.*, **26**, 367–378, doi:10.1007/BF02597298.
- Notsu, K. (2016), Who analyzed volcanic gases in the world and in Japan for the first time?, *Bull.*

Volcanol. Soc. Jpn., **61**(1), 253–258 (in Japanese).

- Notsu, K., K. Sugiyama, M. Hosoe, A. Uemura, Y. Shimoike, F. Tsunomori, H. Sumino, J. Yamamoto, T. Mori, and P. A. Hernández (2005), Diffuse CO₂ efflux from Iwojima volcano, Izu-Ogasawara arc, Japan, *J. Volcanol. Geotherm. Res.*, **139**(3–4), 147–161, doi:10.1016/j.jvolgeores.2004.08.003.
- Notsu, K., T. Mori, S. C. Do Vale, H. Kagi, and T. Ito (2006), Monitoring quiescent volcanoes by diffuse CO₂ degassing: Case study of Mt. Fuji, Japan, *Pure Appl. Geophys.*, **163**(4), 825–835, doi:10.1007/s00024-006-0051-0.
- Nurhasan, Y. Ogawa, N. Ujihara, S. Bulent Tank, Y. Honkura, S. Onizawa, T. Mori, and M. Makino (2006), Two electrical conductors beneath Kusatsu-Shirane volcano, Japan, imaged by audiomagnetotellurics, and their implications for the hydrothermal system, *Earth Planets Space*, **58**, 1053–1059, doi:10.1186/BF03352610.
- Ohba, T., J. Hirabayashi, K. Nogami, M. Kusakabe, and M. Yoshida (2008), Magma degassing process during the eruption of Mt. Unzen, Japan in 1991 to 1995: Modeling with the chemical composition of volcanic gas, *J. Volcanol. Geotherm. Res.*, **175**(1–2), 120–132, doi:10.1016/j.jvolgeores.2008.03.040.
- Ohsawa, S., K. Kazahaya, and M. Yasuhara (2002), Geochemistry of fluids from hot springs, mineral springs, wells and fumarolic area in the Shimabara Peninsula, Middle Western Kyushu, Japan, *J. Jpn. Soc. Hot Spring Sci.*, **52**(2), 51–68 (in Japanese with English abstract).
- Ohwada, M., K. Kazahaya, T. Mori, R. Kazahaya, J. Hirabayashi, M. Miyashita, S. Onizawa, and T. Mori (2013), Sulfur dioxide emissions related to volcanic activity at Asama volcano, Japan, *Bull. Volcanol.*, **75**(12), 775, doi:10.1007/s00445-013-0775-5.
- Okita, T., and D. Shimozuru (1974), Remote sensing of volcanic gases: Amount of sulfur dioxide emitted from volcanoes, *Bull. Volcanol. Soc. Jpn.*, **19**(1), 63–64 (in Japanese).
- Omori, F. (1912), The eruptions and earthquakes of the Asama-yama, *Bull. Imp. Earthq. Invest. Comm.*, **6**, 1–147.
- Ono, A., Y. Sano, H. Wakita, and W. F. Giggenbach (1993), Carbon isotopes of methane and carbon dioxide in hydrothermal gases of Japan, *Geochem. J.*, **27**(4–5), 287–295.
- Oppenheimer, C., B. Scaillet, and R. S. Martin (2011), Sulfur degassing from volcanoes: Source conditions, surveillance, plume chemistry and Earth system impacts, *Rev. Mineral. Geochem.*, **73**(1), 363–421, doi:10.2138/rmg.2011.73.13.
- Oppenheimer, C., T. P. Fischer, and B. Scaillet (2014), Volcanic degassing: Process and impact, in *Treatise on Geochemistry*, vol. 4, edited by H. Holland and K. Turekian, pp. 111–179, Elsevier Ltd.

- Padrón, E., P. A. Hernández, T. Toulkeridis, N. M. Pérez, R. Marrero, G. V. Melián, G. Virgili, and K. Notsu (2008), Diffuse CO₂ emission rate from Pululahua and the lake-filled Cuicocha calderas, Ecuador, *J. Volcanol. Geotherm. Res.*, **176**(1), 163–169, doi:10.1016/j.jvolgeores.2007.11.023.
- Padrón, E., P. A. Hernández, N. M. Pérez, T. Toulkeridis, G. Melián, J. Barrancos, G. Virgili, H. Sumino, and K. Notsu (2012a), Fumarole/plume and diffuse CO₂ emission from Sierra Negra caldera, Galapagos archipelago, *Bull. Volcanol.*, **74**(6), 1509–1519, doi:10.1007/s00445-012-0610-4.
- Padrón, E., N. M. Pérez, P. A. Hernández, H. Sumino, G. Melián, J. Barrancos, D. Nolasco, and G. Padilla (2012b), Helium emission at Cumbre Vieja volcano, La Palma, Canary Islands, *Chem. Geol.*, **312–313**, 138–147, doi:10.1016/j.chemgeo.2012.04.018.
- Padrón, E. et al. (2015), Dynamics of diffuse carbon dioxide emissions from Cumbre Vieja volcano, La Palma, Canary Islands, *Bull. Volcanol.*, **77**, 28, doi:10.1007/s00445-015-0914-2.
- Pantaleo, M., and T. R. Walter (2014), The ring-shaped thermal field of Stefanos crater, Nisyros Island: a conceptual model, *Solid Earth*, **5**(1), 183–198, doi:10.5194/se-5-183-2014.
- Paonita, A., A. Caracausi, G. Iacono-Marziano, M. Martelli, and A. Rizzo (2012), Geochemical evidence for mixing between fluids exsolved at different depths in the magmatic system of Mt Etna (Italy), *Geochim. Cosmochim. Acta*, **84**, 380–394, doi:10.1016/j.gca.2012.01.028.
- Parkinson, K. J. (1981), An improved method for measuring soil respiration in the field, *J. Appl. Ecol.*, **18**(1), 221–228, doi:10.2307/2402491.
- Parks, M. M., S. Caliro, G. Chiodini, D. M. Pyle, T. A. Mather, K. Berlo, M. Edmonds, J. Biggs, P. Nomikou, and C. Raptakis (2013), Distinguishing contributions to diffuse CO₂ emissions in volcanic areas from magmatic degassing and thermal decarbonation using soil gas ²²²Rn– $\delta^{13}\text{C}$ systematics: Application to Santorini volcano, Greece, *Earth Planet. Sci. Lett.*, **377–378**, 180–190, doi:10.1016/j.epsl.2013.06.046.
- Pebesma, E. J. (2004), Multivariable geostatistics in S: the gstat package, *Comput. Geosci.*, **30**(7), 683–691, doi:10.1016/j.cageo.2004.03.012.
- Pecoraino, G., L. Brusca, W. D'Alessandro, S. Giammanco, S. Inguaggiato, and M. Longo (2005), Total CO₂ output from Ischia Island volcano (Italy), *Geochem. J.*, **39**(5), 451–458, doi:10.2343/geochemj.39.451.
- Pedroni, A., K. Hammerschmidt, and H. Friedrichsen (1999), He, Ne, Ar, and C isotope systematics of geothermal emanations in the Lesser Antilles Islands Arc, *Geochim. Cosmochim. Acta*, **63**(3–4), 515–532, doi:10.1016/S0016-7037(99)00018-6.
- Peiffer, L., R. Bernard-Romero, A. Mazot, Y. A. Taran, M. Guevara, and E. Santoyo (2014), Fluid geochemistry and soil gas fluxes (CO₂–CH₄–H₂S) at a promissory Hot Dry Rock Geothermal

- System: The Acoculco caldera, Mexico, *J. Volcanol. Geotherm. Res.*, **284**, 122–137, doi:10.1016/j.jvolgeores.2014.07.019.
- Peltier, A., A. Finizola, G. A. Douillet, E. Brothelande, and E. Garaebiti (2012), Structure of an active volcano associated with a resurgent block inferred from thermal mapping: The Yasur–Yenkahe volcanic complex (Vanuatu), *J. Volcanol. Geotherm. Res.*, **243–244**, 59–68, doi:10.1016/j.jvolgeores.2012.06.022.
- Pérez, N. M., S. Nakai, H. Wakita, K. Notsu, and B. Talai (1998), Anomalous diffuse degassing of helium-3 and CO₂ related to the active ring-fault structure at Rabaul caldera, Papua New Guinea, paper presented at AGU Fall Meeting, V12B-11, San Francisco, CA, USA.
- Pérez, N. M. et al. (2012), Precursory diffuse CO₂ and H₂S emission signatures of the 2011–2012 El Hierro submarine eruption, Canary Islands, *Geophys. Res. Lett.*, **39**, L16311, doi:10.1029/2012GL052410.
- QGIS Development Team (2016), *QGIS Geographic Information System*, Open Source Geospatial Foundation Project. Available from: <http://www.qgis.org/>
- Ray, M. C., D. R. Hilton, J. Muñoz, T. P. Fischer, and A. M. Shaw (2009), The effects of volatile recycling, degassing and crustal contamination on the helium and carbon geochemistry of hydrothermal fluids from the Southern Volcanic Zone of Chile, *Chem. Geol.*, **266**(1–2), 38–49, doi:10.1016/j.chemgeo.2008.12.026.
- Revil, A. et al. (2008), Inner structure of La Fossa di Vulcano (Vulcano Island, southern Tyrrhenian Sea, Italy) revealed by high-resolution electric resistivity tomography coupled with self-potential, temperature, and CO₂ diffuse degassing measurements, *J. Geophys. Res.*, **113**, B07207, doi:10.1029/2007JB005394.
- Revil, A. et al. (2011), Hydrogeology of Stromboli volcano, Aeolian Islands (Italy) from the interpretation of resistivity tomograms, self-potential, soil temperature and soil CO₂ concentration measurements, *Geophys. J. Int.*, **186**(3), 1078–1094, doi:10.1111/j.1365-246X.2011.05112.x.
- Rizzo, A. et al. (2009), Geochemical evaluation of observed changes in volcanic activity during the 2007 eruption at Stromboli (Italy), *J. Volcanol. Geotherm. Res.*, **182**(3–4), 246–254, doi:10.1016/j.jvolgeores.2008.08.004.
- Rizzo, A. L., H.-J. Jost, A. Caracausi, M. Liotta, and M. Martelli (2014), Real-time measurements of the concentration and isotope composition of atmospheric and volcanic CO₂ at Mount Etna (Italy), *Geophys. Res. Lett.*, **41**, 2382–2389, doi:10.1002/2014GL059722.
- Rizzo, A. L., M. Liuzzo, M. A. Ancellin, and H.-J. Jost (2015), Real-time measurements of $\delta^{13}\text{C}$, CO₂ concentration, and CO₂/SO₂ in volcanic plume gases at Mount Etna, Italy, over 5

- consecutive days, *Chem. Geol.*, **411**, 182–191, doi:10.1016/j.chemgeo.2015.07.007.
- Robertson, E., J. Biggs, M. Edmonds, L. Clor, T. P. Fischer, C. Vye-Brown, G. Kianji, W. Koros, and R. Kandie (2016), Diffuse degassing at Longonot volcano, Kenya: Implications for CO₂ flux in continental rifts, *J. Volcanol. Geotherm. Res.*, **327**, 208–222, doi:10.1016/j.jvolgeores.2016.06.016.
- Rogie, J. D., D. M. Kerrick, G. Chiodini, and F. Frondini (2000), Flux measurements of nonvolcanic CO₂ emission from some vents in central Italy, *J. Geophys. Res.*, **105**(B4), 8435–8445, doi:10.1029/1999JB900430.
- Rose, T. P., and M. L. Davisson (1996), Radiocarbon in hydrologic systems containing dissolved magmatic carbon dioxide, *Science*, **273**(5280), 1367–1370, doi:10.1126/science.273.5280.1367.
- Rouilleau, E., Y. Sano, N. Takahata, S. Kawagucci, and H. Takahashi (2013), He, N and C isotopes and fluxes in Aira caldera: Comparative study of hydrothermal activity in Sakurajima volcano and Wakamiko crater, Kyushu, Japan, *J. Volcanol. Geotherm. Res.*, **258**, 163–175, doi:10.1016/j.jvolgeores.2013.04.003.
- Rouilleau, E., N. Vinet, Y. Sano, N. Takahata, H. Shinohara, M. Ooki, H. A. Takahashi, and R. Furukawa (2015), Effect of the volcanic front migration on helium, nitrogen, argon, and carbon geochemistry of hydrothermal/magmatic fluids from Hokkaido volcanoes, Japan, *Chem. Geol.*, **414**, 42–58, doi:10.1016/j.chemgeo.2015.08.006.
- Ryan, W. B. F. et al. (2009), Global multi-resolution topography synthesis, *Geochem. Geophys. Geosyst.*, **10**(3), Q03014, doi:10.1029/2008GC002332.
- Saito, G., H. Shinohara, and K. Kazahaya (2002), Successive sampling of fumarolic gases at Satsuma-Iwojima and Kuju volcanoes, southwest Japan: Evaluation of short-term variations and precision of the gas sampling and analytical techniques, *Geochem. J.*, **36**(1), 1–20, doi:10.2343/geochemj.36.1.
- Saito, M., J. Hirabayashi, K. Nogami, T. Mori, S. Mizuhashi, and M. Oikawa (2004), Discharge rate of CO₂ from the summit area of Kusatsu-Shirane volcano, in *The 4th Joint Observations of Kusatsu-Shirane Volcano*, pp. 175–181 (in Japanese).
- Saito, M., T. Matsushima, N. Matsuwo, and H. Shimizu (2007), Observation of SO₂ and CO₂ fluxes in and around the active crater of Aso Nakadake Volcano, *Sci. Rep., Dept. Earth Planet. Sci., Kyushu Univ.*, **22**(2), 51–62 (in Japanese with English abstract).
- Sakai, H., and O. Matsubaya (1977), Stable isotopic studies of Japanese geothermal systems, *Geothermics*, **5**, 97–124, doi:10.1016/0375-6505(77)90014-1.
- Salazar, J. M. L., P. A. Hernández, N. M. Pérez, G. Melián, J. Álvarez, F. Segura, and K. Notsu (2001),

- Diffuse emission of carbon dioxide from Cerro Negro volcano, Nicaragua, Central America, *Geophys. Res. Lett.*, **28**(22), 4275–4278, doi:10.1029/2001GL013709.
- Salazar, J. M. L., P. A. Hernández, N. M. Pérez, R. Olmos, F. Barahona, R. Cartagena, T. Soriano, D. L. López, H. Sumino, and K. Notsu (2004), Spatial and temporal variations of diffuse CO₂ degassing at the Santa Ana–Izalco–Coatepeque volcanic complex, El Salvador, Central America, in *Natural Hazards in El Salvador. GSA Spec. Pap.*, vol. 375, edited by W. I. Rose, J. J. Bommer, D. L. López, M. J. Carr, and J. J. Major, pp. 135–146.
- Sano, Y., and B. Marty (1995), Origin of carbon in fumarolic gas from island arcs, *Chem. Geol.*, **119**, 265–274, doi:doi:10.1016/0009-2541(94)00097-R.
- Sano, Y., and S. N. Williams (1996), Fluxes of mantle and subducted carbon along convergent plate boundaries, *Geophys. Res. Lett.*, **23**(20), 2749–2752, doi:10.1029/96GL02260.
- Sano, Y., J. Hirabayashi, T. Oba, and T. Gamo (1994), Carbon and helium isotopic ratios at Kusatsu-Shirane Volcano, Japan, *Appl. Geochem.*, **9**(4), 371–377, doi:10.1016/0883-2927(94)90059-0.
- Sano, Y., T. Gamo, K. Notsu, and H. Wakita (1995), Secular variations of carbon and helium isotopes at Izu-Oshima Volcano, Japan, *J. Volcanol. Geotherm. Res.*, **64**(1–2), 83–94, doi:10.1016/0377-0273(94)00041-E.
- Sano, Y., T. Gamo, and S. N. Williams (1997), Secular variations of helium and carbon isotopes at Galeras volcano, Colombia, *J. Volcanol. Geotherm. Res.*, **77**(1–4), 255–265, doi:10.1016/S0377-0273(96)00098-4.
- Sano, Y., Y. Nishio, S. Sasaki, T. Gamo, and K. Nagao (1998), Helium and carbon isotope systematics at Ontake volcano, Japan, *J. Geophys. Res.*, **103**(B10), 23863–23873, doi:10.1029/98JB01666.
- Sansivero, F., G. Scarpato, and G. Vilardo (2013), The automated infrared thermal imaging system for the continuous long-term monitoring of the surface temperature of the Vesuvius crater, *Annals of Geophysics*, **56**(4), S0454, doi:10.4401/ag-6460.
- Sato, M., T. Mori, K. Notsu, and H. Wakita (1999), Carbon and helium isotopic composition of fumarolic gases and hot spring gases from Kirishima volcanic area, *Bull. Volcanol. Soc. Jpn.*, **44**(6), 279–283 (in Japanese).
- Sato, M., T. Mori, Y. Shimoike, K. Nagao, and K. Notsu (2002), Carbon isotope systematics of CO₂, CO and CH₄ in fumarolic gases from Satsuma-Iwojima volcanic island, Japan, *Earth Planets Space*, **54**(3), 257–263, doi:10.1186/BF03353025.
- Savage, M. K., T. Ohminato, Y. Aoki, H. Tsuji, and S. M. Greve (2010), Stress magnitude and its temporal variation at Mt. Asama Volcano, Japan, from seismic anisotropy and GPS, *Earth Planet. Sci. Lett.*, **290**(3–4), 403–414, doi:10.1016/j.epsl.2009.12.037.
- Schöpa, A., M. Pantaleo, and T. R. Walter (2011), Scale-dependent location of hydrothermal vents:

- Stress field models and infrared field observations on the Fossa Cone, Vulcano Island, Italy, *J. Volcanol. Geotherm. Res.*, **203**(3–4), 133–145, doi:10.1016/j.jvolgeores.2011.03.008.
- Shaw, A. M., D. R. Hilton, T. P. Fischer, J. A. Walker, and G. E. Alvarado (2003), Contrasting He-C relationships in Nicaragua and Costa Rica: Insights into C cycling through subduction zones, *Earth Planet. Sci. Lett.*, **214**(3–4), 499–513, doi:10.1016/S0012-821X(03)00401-1.
- Shibata, Y., K. Noguchi, and O. Kaneko (1937), Geochemical investigations of volcanoes in Japan. IX: Investigation of the concentration of D₂O in the spring waters in vicinity of Volcano Asama. I, *Nippon Kagaku Kaishi*, **58**(10), 1013–1024 (in Japanese), doi:10.1246/nikkashi1921.58.10_1013.
- Shimano, T., A. Iida, M. Yoshimoto, A. Yasuda, and S. Nakada (2005), Petrological characteristics of the 2004 eruptive deposits of Asama volcano, Central Japan, *Bull. Volcanol. Soc. Jpn.*, **50**(5), 315–332 (in Japanese with English abstract).
- Shimoike, Y., K. Kazahaya, and H. Shinohara (2002), Soil gas emission of volcanic CO₂ at Satsuma-Iwojima volcano, Japan, *Earth Planets Space*, **54**(3), 239–247, doi:10.1186/BF03353023.
- Shinohara, H. (2008), Excess degassing from volcanoes and its role on eruptive and intrusive activity, *Rev. Geophys.*, **46**, RG4005, doi:10.1029/2007RG000244.
- Shinohara, H. (2013), Volatile flux from subduction zone volcanoes: Insights from a detailed evaluation of the fluxes from volcanoes in Japan, *J. Volcanol. Geotherm. Res.*, **268**, 46–63, doi:10.1016/j.jvolgeores.2013.10.007.
- Shinohara, H., T. Ohba, K. Kazahaya, and H. Takahashi (2008), Origin of volcanic gases discharging from a cooling lava dome of Unzen volcano, Japan, *J. Volcanol. Geotherm. Res.*, **175**(1–2), 133–140, doi:10.1016/j.jvolgeores.2008.03.024.
- Shinohara, H., T. Ohminato, M. Takeo, H. Tsuji, and R. Kazahaya (2015), Monitoring of volcanic gas composition at Asama volcano, Japan, during 2004–2014, *J. Volcanol. Geotherm. Res.*, **303**, 199–208, doi:10.1016/j.jvolgeores.2015.07.022.
- Sinclair, A. J. (1974), Selection of threshold values in geochemical data using probability graphs, *J. Geochem. Explor.*, **3**, 129–149, doi:10.1016/0375-6742(74)90030-2.
- Siniscalchi, A., S. Tripaldi, M. Neri, S. Giammanco, S. Piscitelli, M. Balasco, B. Behncke, C. Magri, V. Naudet, and E. Rizzo (2010), Insights into fluid circulation across the Pernicana Fault (Mt. Etna, Italy) and implications for flank instability, *J. Volcanol. Geotherm. Res.*, **193**(1–2), 137–142, doi:10.1016/j.jvolgeores.2010.03.013.
- van Soest, M. C., D. R. Hilton, and R. Kreulen (1998), Tracing crustal and slab contributions to arc magmatism in the Lesser Antilles island arc using helium and carbon relationships in geothermal fluids, *Geochim. Cosmochim. Acta*, **62**(19–20), 3323–3335, doi:10.1016/S0016-

7037(98)00241-5.

- Sorey, M. L., W. C. Evans, B. M. Kennedy, C. D. Farrar, L. J. Hainsworth, and B. Hausback (1998), Carbon dioxide and helium emissions from a reservoir of magmatic gas beneath Mammoth Mountain, California, *J. Geophys. Res.*, **103**(B7), 15303–15323, doi:10.1029/98JB01389.
- Spampinato, L., S. Calvari, C. Oppenheimer, and E. Boschi (2011), Volcano surveillance using infrared cameras, *Earth-Sci. Rev.*, **106**(1–2), 63–91, doi:10.1016/j.earscirev.2011.01.003.
- Sparks, R. S. J. (2003), Dynamics of magma degassing, in *Volcanic Degassing, Geol. Soc. Lond. Spec. Pub.*, vol. 213, edited by C. Oppenheimer, D. M. Pyle, and J. Barclay, pp. 5–22, doi:10.1144/GSL.SP.2003.213.01.02.
- Stolper, E., and J. R. Holloway (1988), Experimental determination of the solubility of carbon dioxide in molten basalt at low pressure, *Earth Planet. Sci. Lett.*, **87**, 397–408, doi:10.1016/0012-821X(88)90004-0.
- Sturchio, N. C., S. N. Williams, and Y. Sano (1993), The hydrothermal system of Volcan Puracé, Colombia, *Bull. Volcanol.*, **55**(4), 289–296, doi:10.1007/BF00624356.
- Sumino, H., K. Notsu, S. Nakai, M. Sato, K. Nagao, M. Hosoe, and H. Wakita (2004), Noble gas and carbon isotopes of fumarolic gas from Iwojima volcano, Izu-Ogasawara arc, Japan: implications for the origin of unusual arc magmatism, *Chem. Geol.*, **209**(1–2), 153–173, doi:10.1016/j.chemgeo.2004.05.002.
- Suto, S. (1998), The fact finding study on volcanic gas and its disaster in Japan, *Geol. Surv. Jpn. Open-file Rep.*, 328, Geol. Surv. of Jpn., Tsukuba, Ibaraki, Japan (in Japanese).
- Suzuki, H., and N. Tase (2010), Carbon isotopic ratio of dissolved inorganic carbon in the spring water around Asama volcano: Estimation of the contribution rate of volcanic CO₂, *J. Groundwater Hydrol.*, **52**(3), 247–260 (in Japanese with English abstract), doi:10.5917/jagh.52.247.
- Takagi, A., K. Fukui, K. Fujiwara, Y. Ueda, S. Iijima, T. Yamamoto, T. Sakai, T. Kanno, and H. Katayama (2005), Magma supply system of the 2004 eruption at Asama Volcano estimated by crustal deformation data, *Bull. Volcanol. Soc. Jpn.*, **50**, 363–375 (in Japanese with English abstract).
- Takahashi, M., and M. Yasui (2013), Proximal volcanic geology and field excursion guide to the Asama-Maekake Volcano: Historical eruptive products of the Asama-Maekake Volcano distributed around the Kuromamegawara area, *Bull. Volcanol. Soc. Jpn.*, **58**(1), 311–328 (in Japanese).
- Takahata, N., R. Yokochi, Y. Nishio, and Y. Sano (2003), Volatile element isotope systematics at Ontake volcano, Japan, *Geochem. J.*, **37**(3), 299–310, doi:10.2343/geochemj.37.299.

- Takeo, M., Y. Aoki, T. Ohminato, and M. Yamamoto (2006), Magma supply path beneath Mt. Asama volcano, Japan, *Geophys. Res. Lett.*, **33**, L15310, doi:10.1029/2006GL026247.
- Tanaka, H. K. M., T. Uchida, M. Tanaka, M. Takeo, J. Oikawa, T. Ohminato, Y. Aoki, E. Koyama, and H. Tsuji (2009), Detecting a mass change inside a volcano by cosmic-ray muon radiography (muography): First results from measurements at Asama volcano, Japan, *Geophys. Res. Lett.*, **36**, L17302, doi:10.1029/2009GL039448.
- Tanaka, H. K. M., H. Taira, T. Uchida, M. Tanaka, M. Takeo, T. Ohminato, Y. Aoki, R. Nishitama, D. Shoji, and H. Tsuji (2010), Three-dimensional computational axial tomography scan of a volcano with cosmic ray muon radiography, *J. Geophys. Res.*, **115**, B12332, doi:10.1029/2010JB007677.
- Taran, Y., J. C. Gavilanes, and A. Cortés (2002a), Chemical and isotopic composition of fumarolic gases and the SO₂ flux from Volcán de Colima, México, between the 1994 and 1998 eruptions, *J. Volcanol. Geotherm. Res.*, **117**(1–2), 105–119, doi:10.1016/S0377-0273(02)00239-1.
- Taran, Y., S. Inguaggiato, N. Varley, G. Capasso, and R. Favara (2002b), Helium and carbon isotopes in thermal waters of the Jalisco block, Mexico, *Geoffs. Int.*, **41**(4), 459–466.
- Taran, Y. A., A. M. Rozhkov, E. K. Serafimova, and A. D. Esikov (1991), Chemical and isotopic composition of magmatic gases from the 1988 eruption of Klyuchevskoy volcano, Kamchatka, *J. Volcanol. Geotherm. Res.*, **46**(3–4), 255–263, doi:10.1016/0377-0273(91)90087-G.
- Taran, Y. A., V. P. Pilipenko, A. M. Rozhkov, and E. A. Vakin (1992), A geochemical model for fumaroles of the Mutnovsky volcano, Kamchatka, USSR, *J. Volcanol. Geotherm. Res.*, **49**(3–4), 269–283, doi:10.1016/0377-0273(92)90018-9.
- Taran, Y. A., J. W. Hedenquist, M. A. Korzhinsky, S. I. Tkachenko, and K. I. Shmulovich (1995), Geochemistry of magmatic gases from Kudryavy volcano, Iturup, Kuril Islands, *Geochim. Cosmochim. Acta*, **59**(9), 1749–1761, doi:10.1016/0016-7037(95)00079-F.
- Taran, Y. A., C. B. Connor, V. N. Shapar, A. A. Ovsyannikov, and A. A. Bilichenko (1997), Fumarolic activity of Avachinsky and Koryaksky volcanoes, Kamchatka, from 1993 to 1994, *Bull. Volcanol.*, **58**(6), 441–448, doi:10.1007/s004450050152.
- Tassi, F., J. Fiebig, O. Vaselli, and M. Nocentini (2012), Origins of methane discharging from volcanic-hydrothermal, geothermal and cold emissions in Italy, *Chem. Geol.*, **310–311**, 36–48, doi:10.1016/j.chemgeo.2012.03.018.
- Tassi, F., O. Vaselli, C. B. Papazachos, L. Giannini, G. Chiodini, G. E. Vougioukalakis, E. Karagianni, D. Vamvakaris, and D. Panagiotopoulos (2013), Geochemical and isotopic changes in the

- fumarolic and submerged gas discharges during the 2011–2012 unrest at Santorini caldera (Greece), *Bull. Volcanol.*, **75**, 711, doi:10.1007/s00445-013-0711-8.
- Tassi, F. et al. (2016), Geochemistry of fluid discharges from Peteroa volcano (Argentina-Chile) in 2010–2015: Insights into compositional changes related to the fluid source region(s), *Chem. Geol.*, **432**, 41–53, doi:10.1016/j.chemgeo.2016.04.007.
- Toutain, J.-P., F. Sortino, J.-C. Baubron, P. Richon, Surono, S. Sumarti, and A. Nonell (2009), Structure and CO₂ budget of Merapi volcano during inter-eruptive periods, *Bull. Volcanol.*, **71**(7), 815–826, doi:10.1007/s00445-009-0266-x.
- Tu, K. P., P. D. Brooks, and T. E. Dawson (2001), Using septum-capped vials with continuous-flow isotope ratio mass spectrometric analysis of atmospheric CO₂ for keeling plot applications, *Rapid Commun. Mass Spectrom.*, **15**(12), 952–956, doi:10.1002/rcm.320.
- Varekamp, J. C., R. Kreulen, R. P. E. Poorter, and M. J. Van Bergen (1992), Carbon sources in arc volcanism, with implications for the carbon cycle, *Terra Nova*, **4**(3), 363–373, doi:10.1111/j.1365-3121.1992.tb00825.x.
- Varley, N. R., and M. A. Armienta (2001), The absence of diffuse degassing at Popocatepetl volcano, Mexico, *Chem. Geol.*, **177**, 157–173, doi:10.1016/S0009-2541(00)00389-2.
- Vilardo, G., F. Sansivero, and G. Chiodini (2015), Long-term TIR imagery processing for spatiotemporal monitoring of surface thermal features in volcanic environment: A case study in the Campi Flegrei (Southern Italy), *J. Geophys. Res. Solid Earth*, **120**, 812–826, doi:10.1002/2014JB011497.
- Viveiros, F., C. Cardellini, T. Ferreira, S. Caliro, G. Chiodini, and C. Silva (2010), Soil CO₂ emissions at Furnas volcano, São Miguel Island, Azores archipelago: Volcano monitoring perspectives, geomorphologic studies, and land use planning application, *J. Geophys. Res.*, **115**, B12208, doi:10.1029/2010JB007555.
- Wallace, P. J. (2005), Volatiles in subduction zone magmas: concentrations and fluxes based on melt inclusion and volcanic gas data, *J. Volcanol. Geotherm. Res.*, **140**(1–3), 217–240, doi:10.1016/j.jvolgeores.2004.07.023.
- Wardell, L. J., P. R. Kyle, and A. R. Campbell (2003), Carbon dioxide emissions from fumarolic ice towers, Mount Erebus volcano, Antarctica, in *Volcanic Degassing*, *Geol. Soc. Lond. Spec. Pub.*, vol. 213, edited by C. Oppenheimer, D. M. Pyle, and J. Barclay, pp. 231–246, doi:10.1144/GSL.SP.2003.213.01.1.
- Wardell, L. J., P. R. Kyle, and C. Chaffin (2004), Carbon dioxide and carbon monoxide emission rates from an alkaline intra-plate volcano: Mt. Erebus, Antarctica, *J. Volcanol. Geotherm. Res.*, **131**(1–2), 109–121, doi:10.1016/S0377-0273(03)00320-2.

- Wei, F., J. Xu, Z. Shangguan, B. Pan, H. Yu, W. Wei, X. Bai, and Z. Chen (2016), Helium and carbon isotopes in the hot springs of Changbaishan Volcano, northeastern China: A material connection between Changbaishan Volcano and the west Pacific plate?, *J. Volcanol. Geotherm. Res.*, **327**, 398–406, doi:10.1016/j.jvolgeores.2016.09.005.
- Weiss, A. D. (2001), Topographic position and landforms analysis, paper presented at ESRI User Conference, San Diego, CA.
- Wen, H.-Y., T. F. Yang, T. F. Lan, H.-F. Lee, C.-H. Lin, Y. Sano, and C.-H. Chen (2016), Soil CO₂ flux in hydrothermal areas of the Tatun Volcano Group, Northern Taiwan, *J. Volcanol. Geotherm. Res.*, **321**, 114–124, doi:10.1016/j.jvolgeores.2016.04.021.
- Werner, C., and S. Brantley (2003), CO₂ emissions from the Yellowstone volcanic system, *Geochem. Geophys. Geosyst.*, **4**(7), 1061, doi:10.1029/2002GC000473.
- Werner, C., and C. Cardellini (2006), Comparison of carbon dioxide emissions with fluid upflow, chemistry, and geologic structures at the Rotorua geothermal system, New Zealand, *Geothermics*, **35**(3), 221–238, doi:10.1016/j.geothermics.2006.02.006.
- Werner, C., T. Hurst, B. Scott, S. Sherburn, B. W. Christenson, K. Britten, J. Cole-Baker, and B. Mullan (2008), Variability of passive gas emissions, seismicity, and deformation during crater lake growth at White Island Volcano, New Zealand, 2002–2006, *J. Geophys. Res.*, **113**, B01204, doi:10.1029/2007JB005094.
- Werner, C., D. Bergfeld, C. D. Farrar, M. P. Doukas, P. J. Kelly, and C. Kern (2014), Decadal-scale variability of diffuse CO₂ emissions and seismicity revealed from long-term monitoring (1995–2013) at Mammoth Mountain, California, USA, *J. Volcanol. Geotherm. Res.*, **289**, 51–63, doi:10.1016/j.jvolgeores.2014.10.020.
- Wessel, P., W. H. F. Smith, R. Scharroo, J. Luis, and F. Wobbe (2013), Generic Mapping Tools: Improved version released, *EOS Trans., Am. Geophys. Union*, **94**(45), 409–410, doi:10.1002/2013EO450001.
- Williams-Jones, G., J. Stix, M. Heiligmann, A. Charland, B. Sherwood Lollar, N. Arner, G. Garzón V, J. Barquero, and E. Fernandez (2000), A model of diffuse degassing at three subduction-related volcanoes, *Bull. Volcanol.*, **62**(2), 130–142, doi:10.1007/s004450000075.
- Yasui, M., and T. Koyaguchi (1998), Formation of a pyroclastic cone in the 1783 plinian eruptions of Asama Volcano, *Bull. Volcanol. Soc. Jpn.*, **43**(6), 457–465 (in Japanese with English abstract).
- Yasui, M., and T. Koyaguchi (2004), Sequence and eruptive style of the 1783 eruption of Asama Volcano, central Japan: a case study of an andesitic explosive eruption generating fountain-fed lava flow, pumice fall, scoria flow and forming a cone, *Bull. Volcanol.*, **66**(3), 243–262,

doi:10.1007/s00445-003-0308-8.

Yasui, M., and M. Takahashi (2015), Formation of the andesitic welded pyroclastic cones by pyroclastic eruption recorded in the summit area of Asama-Maekake volcano and the collapsed caldera wall of Kurofu volcano, *Bull. Volcanol. Soc. Jpn.*, **60**(2), 109–123 (in Japanese with English abstract).

Yoshimoto, M. et al. (2005), Mass estimation and characteristics of ejecta from the 2004 eruption of Asama volcano, *Bull. Volcanol. Soc. Jpn.*, **50**(6), 519–533 (in Japanese with English abstract).

Appendix A

Observed data of soil CO₂ flux and soil temperature

A.1 Soil CO₂ flux and soil temperature in 2012–2014 at the summit area and the eastern flank of Asama volcano

Site	Easting [m]	Northing [m]	Date (YYMMDD)	CO ₂ flux [g m ⁻² day ⁻¹]	Temperature [°C]	ΔT [°C]
400	277808	4031754	121026	296	14	6
370	277655	4031713	121026	24.0	11	3
280	277395	4031746	121026	nd	9	1
260	277365	4031942	121026	1.2	9	1
180	277421	4032069	121026	nd	8	0
170	277522	4032144	121026	1.3	7	-1
130	277705	4032152	121026	2.61	9	1
110	277799	4032101	121026	5.08	7	-1
70	277876	4031995	121026	98.9	9	1
T1	277895	4032075	121026	42.6	7	-1
T2	277911	4032188	121026	10.3	8	0
120	277968	4032234	121026	3.92	8	0
140	277755	4032276	121026	nd	8	0
60	277868	4031848	121026	141	10	2
90	278184	4032063	121026	265	10	2
430	278106	4031534	121026	1.59	8	0
410	277920	4031583	121026	nd	8	0
420	277912	4031388	121026	nd	9	1
390	277650	4031335	121026	nd	8	0
340	277397	4031512	121026	nd	7	-1
330	277180	4031592	121026	nd	5	-3
270	277059	4031875	121026	nd	5	-3
190	277254	4032219	121026	1.70	5	-3
160	277411	4032297	121026	nd	4	-4
T3	278087	4032059	121026	74.6	9	1
T4	278047	4032030	121026	51.4	9	1
T5	278201	4031990	121026	210	11	3
T6	278266	4031899	121026	86.6	10	2
T7	278261	4031851	121026	157	9	1
T8	278305	4031797	121026	45.1	8	0
T9	278323	4031781	121026	6.16	9	1
T10	278326	4031781	121026	nd	8	0
T11	278260	4031597	121026	173	9	1
T12	278288	4031573	121026	126	15	7
T13	278304	4031561	121026	69.3	13	5
T14	278327	4031546	121026	72.6	9	1
T15	278363	4031522	121026	11.9	7	-1
T16	278392	4031510	121026	5.96	9	1
T17	278435	4031487	121026	3.34	8.3	0.1
T18	278469	4031473	121026	2.61	8.7	0.4
A1 (60)	277867	4031848	130515	37.4	17.9	1.2
A2	277837	4031816	130515	298	15.5	-1.2
A3 (400)	277812	4031759	130515	19.7	18.2	1.5
A4	277755	4031752	130515	272	16.3	-0.4
A5	277701	4031726	130515	nd	14.7	-2.0
A6	277728	4031739	130515	414	15.8	-0.9
A7	277709	4031731	130515	43.1	13.3	-3.4

Site	Easting [m]	Northing [m]	Date (YYMMDD)	CO ₂ flux [g m ⁻² day ⁻¹]	Temperature [°C]	δT [°C]
A8	277663	4031724	130515	7.70	13.3	-3.4
A9	277605	4031730	130515	32.3	16.3	-0.4
A10	277541	4031754	130515	nd	12.2	-4.5
A11	277508	4031758	130515	nd	17.4	0.7
A12	277506	4031735	130515	nd	20.6	3.9
A13	277559	4031704	130515	nd	16.7	0.0
A14	277624	4031684	130515	7.57	14.3	-2.4
A15	277698	4031679	130515	nd	13.6	-3.1
A16	277722	4031718	130515	164	19.8	3.1
A17	277727	4031704	130515	15.2	18.4	1.7
A18	277731	4031676	130515	nd	14.7	-2.0
A19	277775	4031678	130515	1.23	18.5	1.8
A20	277819	4031709	130515	1.84	18.2	1.5
A21	277835	4031749	130515	36.7	19.4	2.7
A22	277866	4031735	130515	5.23	19.5	2.8
A23	277934	4031744	130515	74.0	18.3	1.6
A24	277943	4031800	130515	208	19.6	2.9
A25	277961	4031849	130515	391	18.8	2.1
A26	277967	4031907	130515	109	18.6	1.9
A27	277967	4031970	130515	136	22.3	5.6
A28	277909	4032017	130515	49.6	17.1	0.4
A29	277861	4032071	130515	7.89	11.0	-5.7
A30	277898	4032077	130515	3.78	11.9	-4.8
A31	277981	4032073	130515	256	23.4	6.7
A32	278021	4032006	130515	149	16.9	0.2
A33	277968	4032136	130515	187	13.1	-3.6
A34	277918	4032150	130515	10.8	11.3	-5.4
A35	278033	4032134	130515	83.9	19.1	2.4
A36	278050	4032032	130515	86.8	21.5	4.8
A37	278038	4031952	130515	52.2	18.3	1.6
A38	278010	4031879	130515	143	16.3	-0.4
A39	277985	4031795	130515	94.0	17.9	1.2
A40	277966	4031711	130515	31.4	17.3	0.6
A41	277888	4031670	130515	2.43	15.6	-1.1
A42	277854	4031614	130515	nd	15.0	-1.7
A43	277965	4031658	130515	26.4	19.3	2.6
A44	277939	4031638	130515	0.65	21.8	5.1
A45	278020	4031727	130515	0.62	19.7	3.0
A46	278041	4031810	130515	nd	12.0	-4.7
A47	278063	4031895	130515	nd	16.3	-0.4
A48	278067	4031978	130515	66.6	19.2	2.5
A49	278085	4032058	130515	72.2	18.6	1.9
A50 (90)	278161	4032068	130515	143	20.6	3.9
A51	278190	4032104	130515	143	27.6	10.9
A52	278212	4032130	130515	19.4	26.4	9.7
A53	278219	4032139	130515	17.7	22.7	6.0
A54	278219	4032095	130515	47.3	29.1	12.4
A55	278200	4032045	130515	142	25.7	9.0
A56	278246	4031930	130515	194	nan	nan
A57	278267	4031862	130515	16.8	19.3	2.6
A58	278232	4031815	130515	30.3	19.7	3.0
A59	278212	4031740	130515	168	20.4	3.7
A60	278189	4031649	130515	192	19.8	3.1
A61	278165	4031606	130515	12.6	16.0	-0.7
A62	278159	4031652	130515	nd	11.9	-4.8
A63	278201	4031691	130515	7.78	20.8	4.1
A64	278240	4031782	130515	170	20.5	3.8
310	278253	4031576	140527	202	14.6	4.9
311	278232	4031583	140527	101	11.5	1.8
312	278214	4031591	140527	163	13.8	4.1

Site	Easting [m]	Northing [m]	Date (YYMMDD)	CO ₂ flux [g m ⁻² day ⁻¹]	Temperature [°C]	δT [°C]
313	278191	4031595	140527	245	12.5	2.8
314	278164	4031600	140527	78.5	9.6	-0.1
315	278132	4031545	140527	132	9.5	-0.2
316	278088	4031497	140527	91.5	11.8	2.1
317	278036	4031477	140527	125	11.3	1.6
318	277984	4031456	140527	0.72	8.8	-0.9
319	277946	4031419	140527	nd	8.4	-1.3
320	277920	4031488	140527	2.43	11.0	1.3
321	277981	4031567	140527	69.6	11.8	2.1
322	277935	4031523	140527	nd	8.9	-0.8
323	277987	4031512	140527	261	11.9	2.2
324	277956	4031481	140527	9.21	10.6	0.9
325	278012	4031560	140527	191	11.8	2.1
326	278043	4031609	140527	52.6	8.2	-1.5
327	278085	4031609	140527	nd	7.9	-1.8
328	278122	4031604	140527	nd	7.6	-2.1
329	278073	4031552	140527	nd	10.7	1.0
330	278045	4031511	140527	478	12.5	2.8
331	278061	4031525	140527	81.2	11.2	1.5
332	278092	4031538	140527	nd	11.9	2.2
333	278136	4031598	140527	nd	8.9	-0.8
334	278114	4031684	140527	nd	8.3	-1.4
335	278123	4031737	140527	nd	10.0	0.3
336	278175	4031739	140527	nd	11.7	2.0
337	278163	4031811	140527	nd	8.0	-1.7
338	278172	4031907	140527	nd	9.1	-0.6
339	278115	4031991	140527	105	7.0	-2.7
340 (90)	278163	4032071	140527	143	14.7	5.0
341	278138	4032115	140527	51.0	19.5	9.8
342	278084	4032155	140527	8.46	9.6	-0.1
343	277999	4032201	140527	38.5	16.6	6.9
344	277882	4032226	140527	nd	6.7	-3.0
345 (120)	277960	4032232	140527	2.13	7.0	-2.7
346	278019	4032215	140527	11.9	11.5	1.8
347	278048	4032193	140527	4.99	10.6	0.9
348	278111	4032172	140527	24.7	10.4	0.7
349	278133	4032179	140527	18.0	9.5	-0.2
350	278144	4032193	140527	4.33	10.0	0.3
351	278158	4032205	140527	17.9	17.2	7.5
352	278188	4032210	140527	1.92	13.3	3.6
353	278165	4032222	140527	22.1	44.6	34.9
354	278227	4032177	140527	2.92	14.2	4.5
355	278254	4032157	140527	8.40	15.7	6.0
356	278275	4032164	140527	nd	6.7	-3.0
357	278287	4032120	140527	nd	7.5	-2.2
358	278284	4032075	140527	1.32	9.0	-0.7
359	278254	4032063	140527	30.1	14.2	4.5
360	278261	4032040	140527	12.3	14.2	4.5
361	278271	4031984	140527	9.60	17.3	7.6
362	278286	4031984	140527	24.5	11.4	1.7
363	278297	4031987	140527	3.25	10.0	0.3
364	278292	4031987	140527	13.5	11.2	1.5
365	278295	4031987	140527	6.26	11.8	2.1
366	278307	4031989	140527	1.72	10.2	0.5
367	278311	4031926	140527	nd	10.8	1.1
368 (A57)	278268	4031858	140527	20.3	17.5	7.8
369	278261	4031900	140527	15.4	16.6	6.9
370B (A56)	278248	4031930	140527	102	nan	nan
371	278285	4031938	140527	24.2	13.2	3.5
372	278301	4031862	140527	3.48	nan	nan

Site	Easting [m]	Northing [m]	Date (YYMMDD)	CO ₂ flux [g m ⁻² day ⁻¹]	Temperature [°C]	δT [°C]
373	278305	4031784	140527	4.88	13.5	3.8
374	278320	4031746	140527	nd	12.3	2.6
375	278305	4031722	140527	35.7	nan	nan
376	278265	4031677	140527	72.2	nan	nan
377	278264	4031714	140527	142	17.4	7.7
378	278235	4031642	140527	27.6	18.4	8.7
379	278266	4031623	140527	417	18.5	8.8
380	278300	4031617	140527	144	nan	nan
381	278318	4031611	140527	2.52	14.0	4.3
382	278316	4031635	140527	6.72	14.0	4.3
383	278328	4031584	140527	nd	12.3	2.6
384	278327	4031541	140527	3.44	12.1	2.4
w01 (260)	277367	4031936	141008	0.46	7.0	-0.9
w02	277294	4031923	141008	0.29	7.0	-0.9
w03	277179	4031860	141008	nd	6.9	-0.9
w04	277007	4031981	141008	0.97	7.0	-0.9
w05	276986	4031955	141008	0.43	7.3	-0.6
w06	276974	4031914	141008	0.35	8.4	0.6
w07	276966	4031921	141008	0.35	9.2	1.4
w08	276985	4031983	141008	3.66	8.9	1.1
w09	276997	4031979	141008	13.8	8.8	1.0
w10	277010	4032003	141008	2.16	13.3	5.5
w11	277010	4032000	141008	19.4	28.0	20.2
w12	277020	4032019	141008	17.4	15.7	7.9
w13	277016	4032046	141008	3.72	8.5	0.7
w14	276952	4031917	141008	nd	9.6	1.8
w15	276967	4031975	141008	20.4	9.6	1.8
w16	276949	4031981	141008	nd	5.7	-2.2
w17	276970	4032030	141008	0.31	6.0	-1.9
w18	276984	4032001	141008	12.1	10.2	2.4
w19	276994	4032025	141008	2.96	7.7	-0.1
w20	277005	4032055	141008	3.52	9.8	2.0
w21	277024	4032091	141008	1.0	8.8	1.0
w22	277017	4032135	141008	0.56	6.7	-1.2
w23	277060	4032090	141008	6.54	8.2	0.4
w24	277102	4032130	141008	4.52	7.5	-0.4
w25	277072	4031985	141008	0.70	8.6	0.8
w26	277099	4031758	141008	0.36	8.8	1.0
w27	277200	4031683	141008	nd	9.2	1.4
w28	277296	4031604	141008	nd	7.1	-0.8
w29	277420	4031556	141008	nd	7.8	0.0
w30	277576	4031524	141008	nd	7.7	-0.1
w31	277721	4031491	141008	0.24	7.7	-0.1
w32	277814	4031442	141008	nd	8.2	0.4
w33	279069	4031464	141008	0.48	8.4	0.6
w34	279183	4031469	141008	0.52	9.0	1.2
w35	279345	4031476	141008	nd	9.8	2.0
w36	279521	4031489	141008	0.61	11.4	3.6
w37	279700	4031535	141008	nd	9.3	1.5
w38	279855	4031567	141008	1.23	10.6	2.8
w39	280019	4031622	141008	1.0	10.8	3.0

nd non-detectable, *nan* not measured

A.2 Soil CO₂ flux and soil temperature in 2015 and 2016 at the summit area and the western flank of Asama volcano

Site	Easting [m]	Northing [m]	Date (YYMMDD)	CO ₂ flux [g m ⁻² day ⁻¹]	Temperature [°C]	δT [°C]
102901	277881	4031903	151029	160	6.1	-3.9
102902 (60)	277868	4031850	151029	270	12.2	2.2
102903 (A2)	277836	4031816	151029	49.4	10.9	0.9
102904 (400)	277807	4031761	151029	48.7	13.3	3.3
102905 (A4)	277756	4031752	151029	0.47	9.1	-0.9
102906 (A6)	277730	4031741	151029	15.6	9.4	-0.6
102907 (A26)	277967	4031907	151029	56.0	8.2	-1.8
102908 (A27)	277967	4031971	151029	144	8.9	-1.1
102909 (A32)	278023	4032008	151029	167	8.5	-1.5
102910 (A36)	278051	4032032	151029	135	8.7	-1.3
102911	278050	4032036	151029	194	9.6	-0.4
102912 (A49)	278087	4032058	151029	66.8	8.6	-1.4
102913 (90)	278168	4032069	151029	144	9.6	-0.4
102914	278164	4032067	151029	115	8.0	-2.0
102915 (A55)	278200	4032038	151029	328	12.4	2.4
102916 (361)	278271	4031983	151029	144	12.9	2.9
102917 (371)	278287	4031939	151029	103	10.5	0.5
102918 (A56)	278246	4031930	151029	258	8.8	-1.2
102919 (369)	278261	4031900	151029	253	8.9	-1.1
102920 (A57)	278270	4031862	151029	221	8.4	-1.6
102921 (337)	278164	4031810	151029	nd	8.4	-1.6
102922	278201	4031820	151029	nd	9.5	-0.5
102923 (A58)	278235	4031817	151029	2.68	10.2	0.2
102924	278259	4031823	151029	308	9.1	-0.9
102925	278246	4031825	151029	347	11.8	1.8
102926	278240	4031822	151029	109	13.2	3.2
102927	278274	4031826	151029	560	12.0	2.0
102928	278292	4031833	151029	132	8.3	-1.7
102929	278314	4031838	151029	193	9.5	-0.5
102930	278335	4031837	151029	nd	9.9	-0.1
102931	278331	4031795	151029	nd	9.9	-0.1
102932	278317	4031790	151029	66.3	9.4	-0.6
102933 (373)	278302	4031786	151029	160	9.1	-0.9
102934	278289	4031778	151029	210	8.7	-1.3
102935	278268	4031770	151029	519	10.6	0.6
102936	278241	4031764	151029	114	11.0	1.0
102937 (A59)	278213	4031739	151029	413	12.0	2.0
102938 (A63)	278203	4031694	151029	72.8	12.3	2.3
102939 (A62)	278160	4031652	151029	0.80	8.8	-1.2
102940 (314)	278164	4031599	151029	22.2	11.0	1.0
102941 (313)	278191	4031595	151029	555	10.4	0.4
102942 (312)	278214	4031591	151029	341	9.4	-0.6
102943 (311)	278231	4031584	151029	623	11.5	1.5
102944 (310)	278252	4031578	151029	470	12.1	2.1
102945	278279	4031570	151029	441	15.4	5.4
102946	278296	4031559	151029	325	18.8	8.8
102947	278311	4031551	151029	68.7	13.5	3.5
102948 (384)	278329	4031541	151029	24.9	10.9	0.9
102949	278343	4031528	151029	171	10.6	0.6
102950	278362	4031517	151029	14.7	10.7	0.7
102951	278385	4031506	151029	8.07	10.9	0.9
102952	278409	4031494	151029	4.19	11.3	1.3
102953	278447	4031474	151029	1.24	11.6	1.6
102954	278510	4031453	151029	1.87	11.7	1.7
M01	277031	4032020	160808	4.31	nan	nan
M02 (w24)	277101	4032130	160808	2.75	nan	nan
M03	277081	4032204	160808	0.67	nan	nan

Site	Easting [m]	Northing [m]	Date (YYMMDD)	CO ₂ flux [g m ⁻² day ⁻¹]	Temperature [°C]	δT [°C]
M04	277035	4032239	160808	nd	nan	nan
M05	276974	4032255	160808	nd	nan	nan
M06	276834	4032273	160808	4.30	nan	nan
M07	276704	4032260	160808	1.37	nan	nan
T01 (A11)	277508	4031758	160808	0.27	19.8	-0.2
T02 (A10)	277538	4031750	160808	0.28	20.9	0.9
T03 (A9)	277608	4031732	160808	18.5	19.4	-0.6
T04 (A8)	277665	4031724	160808	7.67	24.8	4.8
T05 (370)	277654	4031716	160808	8.86	24.9	4.9
T06 (A7)	277706	4031732	160808	47.5	20.2	0.2
T07 (A4)	277754	4031750	160808	14.4	nan	nan
T08 (400)	277806	4031763	160808	63.4	22.5	2.5
T09	277879	4031896	160808	19.4	20.5	0.5
T10 (A27)	277967	4031970	160808	238	20.8	0.8
T11 (A32)	278023	4032007	160808	429	20.2	0.2
T12 (T4)	278051	4032034	160808	141	22.6	2.6
T13 (A49)	278086	4032061	160808	127	20.9	0.9
T14 (90)	278168	4032067	160808	79.8	21.9	1.9
T15 (A55)	278200	4032040	160808	110	24.3	4.3
T16 (A56)	278246	4031929	160808	144	22.2	2.2
T17 (369)	278261	4031901	160808	77.9	22.4	2.4
T18 (A57)	278268	4031862	160808	298	21.7	1.7
T19 (A64)	278239	4031784	160808	367	24.2	4.2
T20 (377)	278266	4031712	160808	922	23.5	3.5
T21 (376)	278263	4031676	160808	360	22.5	2.5
T22 (310)	278250	4031577	160808	6640	24.2	4.2
T23 (311)	278230	4031584	160808	2460	22.7	2.7
T24 (312)	278212	4031594	160808	926	21.8	1.8

nd non-detectable, nan not measured

A.3 Soil CO₂ flux and soil temperature in 2016 at jigokudani fumarolic field

Site	Easting [m]	Northing [m]	Date (YYMMDD)	CO ₂ flux [g m ⁻² day ⁻¹]	Temperature [°C]
S01	275425	4031261	160809	27.0	21.6
S02	275420	4031297	160809	37.4	22.0
S03	275421	4031310	160809	17.1	18.7
S04	275421	4031325	160809	16.2	22.2
S05	275411	4031343	160809	23.3	19.4
S06	275432	4031178	160809	2.18.E+04	22.7
S07	275442	4031173	160809	64.2	20.1
S08	275449	4031158	160809	42.1	20.6
S09	275452	4031142	160809	1694	23.7
S10	275450	4031138	160809	231	20.3
S11	275436	4031135	160809	315	20.1
S12	275422	4031103	160809	81.9	17.8
S13	275376	4030997	160809	202	24.5
K01	275420	4031205	160801	10.3	14.7
K02	275415	4031203	160801	6.27	13.9
K03	275413	4031202	160801	19.6	14.7
K04	275412	4031200	160801	18.5	15.1
K05	275395	4031205	160801	94.5	16.7
K06	275400	4031199	160801	16.3	17.7
K07	275396	4031196	160801	64.7	17.6
K08	275402	4031182	160801	57.0	16.5
K09	275402	4031174	160801	2368	16.6
K10	275400	4031173	160801	18.6	15.3
K11	275406	4031190	160801	964	19.1
K12	275400	4031176	160801	1828	19.0
K13	275422	4031164	160801	7215	16.3
K14	275427	4031143	160801	11.7	16.6

Site	Easting [m]	Northing [m]	Date (YYMMDD)	CO ₂ flux [g m ⁻² day ⁻¹]	Temperature [°C]
K15	275418	4031160	160801	2796	16.9
K16	275415	4031159	160801	25.0	19.3
K17	275421	4031215	160801	90.2	17.0
K18	275433	4031210	160801	189	16.2
K19	275436	4031221	160801	13.7	16.4
K20	275411	4031240	160801	34.6	16.5
K21	275403	4031244	160801	2208	17.9
K22	275407	4031231	160801	119	16.7
K23	275423	4031187	160801	63.9	11.3
K24	275416	4031176	160801	1200	19.1
K25	275427	4031174	160801	1.92.E+04	14.5
K26	275435	4031172	160801	2844	19.2
K27	275422	4031152	160801	1.52.E+04	14.0
K28	275433	4031141	160801	2659	22.1
K29	275430	4031138	160801	249	14.5
K30	275425	4031144	160801	54.7	15.0
K31	275439	4031159	160801	85.0	14.3

Appendix B

Compilation of $\delta^{13}\text{C}(\text{CO}_2)$ data for volcanoes and geothermal fields

Volcano or area	Country or area	Type ^a	Sample ^b	Temperature [°C]			$\delta^{13}\text{C}(\text{CO}_2)$ [‰]			Reference
				Avg.	Min.	Max.	Avg.	Min.	Max.	
<i>Intraplate</i>										
Erebus	Antarctica	A	F	4.7	-1.7	11.8	-4.3	-6.7	-2.1	Wardell et al., 2003
La Palma	Canary Islands	A	B	—	—	—	-3.4	-3.7	-2.9	Padrón et al., 2015
Teide	Canary Islands	A	F	—	—	—	-3.4	-4.2	-2.3	Melián et al., 2012
Fogo Island	Cape Verde	A	F	—	—	—	-4.3	—	—	Dionis et al., 2015b
Changbaishan (Paektu)	N. Korea, China	A	B	51.8	11.1	75.0	-4.8	-7.9	-1.6	Wei et al., 2016
Piton de la Fournaise	Réunion	A	B	—	—	—	-5.7	-8.2	-4.1	Marty et al., 1993
Kīlauea, ERZ	USA	A	F	924	905	935	-7.8	-8.9	-6.9	Gerlach and Taylor, 1990
Kīlauea, Summit	USA	A	F	—	—	—	-3.2	-4.4	-2.8	Gerlach and Taylor, 1990
<i>Rift</i>										
Furnas	Azores	A	F	—	—	—	-4.1	—	—	Viveiros et al., 2010
Ardoukoba	Djibouti	A	F	1070	—	—	-4.0	-5.9	0.2	Allard, 1979
Hekla	Iceland	A	F	—	—	—	-4.1	-5.4	-2.2	Ilyinskaya et al., 2015
Pantelleria Island	Italy	A	B, M	—	—	—	-4.3	-5.6	-3.8	Jácome Paz et al., 2016
Pantelleria Island	Italy	A	F	99	98	99	-4.1	-5.2	-3.6	Favara et al., 2001; D'Alessandro et al., 2009; Tassi et al., 2012; Granieri et al., 2014
Ol Doinyo Lengai	Tanzania	A	F	287	261	312	-4.2	-7.4	-2.2	Koepnick et al., 1996; Lee et al., 2016
Askja, Viti crater	Iceland	G	F	28.7	26.8	30.5	-3.9	-4.2	-3.6	Barry et al., 2014
Eyvik	Iceland	G	G	73.5	—	—	-2.9	—	—	Barry et al., 2014
Flúðir	Iceland	G	G	—	—	—	-6.1	—	—	Barry et al., 2014
Hæðarendi	Iceland	G	G	—	—	—	-3.5	—	—	Barry et al., 2014
Hengill	Iceland	G	F	74.4	72.8	77.5	-3.8	-4.5	-3.1	Barry et al., 2014
Hveragerði	Iceland	G	F	100.7	—	—	-2.3	-2.4	-2.3	Barry et al., 2014
Hveravellir	Iceland	G	F	89.6	—	—	-5.1	—	—	Barry et al., 2014
Kerlingafjöll	Iceland	G	F	94.7	—	—	-4.1	—	—	Barry et al., 2014
Köldukvísilabotnar	Iceland	G	G	—	—	—	-3.1	-3.7	-2.5	Barry et al., 2014
Krafla	Iceland	G	F	90.0	76.5	96.7	-3.9	-4.8	-2.4	Barry et al., 2014
Krafla	Iceland	G	G	—	—	—	-3.2	-5.3	-1.4	Barry et al., 2014
Krísuvík	Iceland	G	F	88.6	77.5	99.6	-3.8	-4.2	-3.4	Barry et al., 2014
Kverkfjöll	Iceland	G	F	—	—	—	-2.2	-2.4	-2.0	Barry et al., 2014
Landmannalaugar	Iceland	G	F	98.6	—	—	-3.0	—	—	Barry et al., 2014
Laugar, Orkubú	Iceland	G	G	66.0	—	—	-3.8	—	—	Barry et al., 2014
Vestfjarðá	Iceland	G	G	66.0	—	—	-3.8	—	—	Barry et al., 2014

Volcano or area	Country or area	Type ^a	Sample ^b	Temperature [°C]			$\delta^{13}\text{C}(\text{CO}_2)$ [‰]			Reference
				Avg.	Min.	Max.	Avg.	Min.	Max.	
Little Geysir	Iceland	G	F	82.6	—	—	-2.7	-2.7	-2.7	Barry et al., 2014
Lýsuhóll	Iceland	G	G	—	—	—	-6.3	-6.6	-6.1	Barry et al., 2014
Námafjall	Iceland	G	F	—	—	—	-5.2	-5.3	-5.1	Barry et al., 2014
Nesjavellir	Iceland	G	F	89.0	—	—	-3.6	-4.7	-2.6	Barry et al., 2014
Nesjavellir	Iceland	G	G	240	—	—	0.5	0.4	0.5	Barry et al., 2014
Ormsstaðir	Iceland	G	G	86.9	—	—	-5.9	—	—	Barry et al., 2014
Reykhólar	Iceland	G	G	95.0	—	—	-5.5	—	—	Barry et al., 2014
Reykjanes	Iceland	G	F	100	—	—	-3.2	-3.4	-3.0	Barry et al., 2014
Selfoss	Iceland	G	G	70.0	—	—	-18.4	-18.8	-17.9	Barry et al., 2014
Seljavellir	Iceland	G	G	50.0	—	—	-3.4	-3.4	-3.4	Barry et al., 2014
Svartsengi	Iceland	G	G	240	—	—	-3.8	-4.2	-3.3	Barry et al., 2014
Þeystareykir	Iceland	G	F	89.9	—	—	2.9	—	—	Barry et al., 2014
Þjórsárdalslaug	Iceland	G	F	70.0	—	—	-10.8	-11.0	-10.5	Barry et al., 2014
Vonarskarð	Iceland	G	F	97.7	—	—	1.5	1.4	1.6	Barry et al., 2014
Long Valley caldera	USA	I	B	—	—	—	-5.8	-7.6	-4.2	Hilton, 1996; Bergfeld et al., 2006
Mammoth Mountain	USA	I	B	85	57	92	-5.5	-8.4	-3.9	Sorey et al., 1998; Evans et al., 2002
Mammoth Mountain	USA	I	F	84	81	94	-4.9	-6.3	-4.5	Sorey et al., 1998
Yellowstone	USA	I	B, M	89	73	96	-3.1	-6.4	-1.1	Craig, 1953; Werner and Brantley, 2003
Yellowstone	USA	I	F	100.4	91.1	114.3	-3.3	-4.9	-2.3	Werner and Brantley, 2003; Lowenstern et al., 2015
<i>Subduction</i>										
Copahue-Caviahue	Argentina, Chile	A	B, G	67	27	93	-7.9	-8.8	-7.3	Agusto et al., 2013
Copahue-Caviahue	Argentina, Chile	A	F	106	92	160	-7.4	-8.2	-6.8	Agusto et al., 2013
Planchón-Peteroa	Argentina, Chile	A	B	36.0	24.1	46.2	-12.6	-13.2	-12.1	Tassi et al., 2016
Planchón-Peteroa	Argentina, Chile	A	F	84.7	43.2	89.4	-7.6	-11.9	-2.0	Tassi et al., 2016
Lonquimay Nevados de Chillán	Chile	A	G	54.1	—	—	-14.7	—	—	Ray et al., 2009
Chillán	Chile	A	F	89.1	—	—	-6.9	-7.8	-6.0	Ray et al., 2009
Tupungatito	Chile	A	B	35.2	—	—	-0.3	—	—	Benavente et al., 2013
Tupungatito	Chile	A	F	82.9	80.8	83.6	-6.8	-8.2	-5.3	Benavente et al., 2013
Villarrica	Chile	A	B	75.1	72.2	78.0	-14.5	-17.1	-11.9	Ray et al., 2009
Cumbal	Colombia	A	F	168	120	257	-5.6	-6.7	-4.9	Sano and Williams, 1996; Lewicki et al., 2000
Galeras	Colombia	A	B	30	—	—	-9.0	-9.2	-8.7	Sano et al., 1997
Galeras	Colombia	A	F	—	—	222	-7.0	-7.6	-5.7	Sano and Williams, 1996; Sano et al., 1997
Machin	Colombia	A	F	96	—	—	-9.5	—	—	Sano and Williams, 1996
Puracé	Colombia	A	B	57	36	74	-10.3	-11.5	-8.5	Sturchio et al., 1993
Puracé	Colombia	A	F	86	—	—	-8.5	—	—	Sturchio et al., 1993
Arenal	Costa Rica	A	B	—	—	—	-3.3	-3.4	-3.2	Shaw et al., 2003
Chocosuela-Platanar	Costa Rica	A	B	55.0	46.0	59.5	-2.9	-4.6	-1.9	Shaw et al., 2003
Irazú	Costa Rica	A	F	88.5	—	—	-2.3	—	—	Shaw et al., 2003
Miravalles	Costa Rica	A	B, G	199	88.6	238	-1.9	-3.5	-1.2	Shaw et al., 2003

Volcano or area	Country or area	Type ^a	Sample ^b	Temperature [°C]			$\delta^{13}\text{C}(\text{CO}_2)$ [‰]			Reference
				Avg.	Min.	Max.	Avg.	Min.	Max.	
Poás	Costa Rica	A	F	108	76	220	-3.8	-6.8	-1.3	Sano and Williams, 1996; Shaw et al., 2003; Hilton et al., 2010; Fischer et al., 2015
Rincón de la Vieja	Costa Rica	A	B	86.0	65.3	99.0	-1.0	-3.1	-0.1	Shaw et al., 2003
Turrialba	Costa Rica	A	F	89	84	90	-3.8	-4.4	-2.7	Shaw et al., 2003; Hilton et al., 2010
Micotrin-Trois Pitons	Dominica	A	F	61.5	44.2	76.7	-3.0	-3.5	-1.7	van Soest et al., 1998; Pedroni et al., 1999
Morne aux Diable	Dominica	A	M	—	—	—	-4.0	—	—	Pedroni et al., 1999
Morne Diablotin	Dominica	A	B	20.9	—	—	-4.3	—	—	van Soest et al., 1998
Morne Patates	Dominica	A	B	40.4	—	—	-3.3	—	—	van Soest et al., 1998
Morne Patates	Dominica	A	F	92.6	—	—	-2.0	-2.2	-1.8	van Soest et al., 1998; Pedroni et al., 1999
Coatepeque	El Salvador	A	F	95.2	—	—	-5.7	—	—	Salazar et al., 2004
Izalco	El Salvador	A	F	73.8	—	—	-22.9	—	—	Salazar et al., 2004
Santa Ana	El Salvador	A	F	123.5	—	—	-2.0	—	—	Salazar et al., 2004
Santorini caldera	Greece	A	B	33	31	36	-0.7	-0.9	0.0	Tassi et al., 2013
Santorini caldera	Greece	A	F	85	78	93	-0.3	-0.8	-0.1	Tassi et al., 2013
St. Catherine	Grenada	A	B	54.1	—	—	-3.6	-4.8	-2.6	van Soest et al., 1998; Pedroni et al., 1999
St. Catherine	Grenada	A	F	—	—	—	-2.6	-2.6	-2.5	Pedroni et al., 1999
Chaîne de Bouillante	Guadeloupe	A	B	—	—	—	-2.4	—	—	Pedroni et al., 1999
Soufrière de Guadeloupe	Guadeloupe	A	F	74.8	55.5	94.0	-3.0	-3.2	-2.9	van Soest et al., 1998; Pedroni et al., 1999
Pacaya	Guatemala	A	F	965.0	—	—	-6.9	—	—	Sano and Williams, 1996
Ambang	Indonesia	A	F	97.6	—	—	-4.9	-5.2	-4.5	Jaffe et al., 2004
Awu	Indonesia	A	B	—	—	—	-0.4	—	—	Jaffe et al., 2004
Awu	Indonesia	A	F	96.6	—	—	-1.6	-2.0	-1.3	Jaffe et al., 2004
Egon	Indonesia	A	F	111	98	124	-1.8	-2.0	-1.5	Varekamp et al., 1992
Lewotolo	Indonesia	A	F	308	96	490	-3.9	-5.7	-2.9	Varekamp et al., 1992
Lokon-Empung	Indonesia	A	F	96.1	—	—	-3.6	—	—	Jaffe et al., 2004
Mahawu	Indonesia	A	B	81.5	61.9	101.1	-3.3	-3.5	-3.0	Jaffe et al., 2004
Merapi	Indonesia	A	F	725	500	901	-4.0	-4.5	-3.4	Allard, 1980; Varekamp et al., 1992
Ruang	Indonesia	A	F	119	98	140	-3.2	-3.3	-3.1	Varekamp et al., 1992
Sirung	Indonesia	A	F	95	—	—	-1.7	-1.7	-1.7	Jaffe et al., 2004
Soputan	Indonesia	A	F	82.2	72.9	86.9	-14.5	-20.1	-3.5	Varekamp et al., 1992
Wurlali	Indonesia	A	F	153	135	170	-3.4	-3.4	-3.3	Jaffe et al., 2004
Amiata	Italy	A	F	27	17	52	-2.4	-4.5	1.2	Varekamp et al., 1992
Etna	Italy	A	B, M	21.3	18.7	28.0	-3.9	-25.0	-0.1	Tassi et al., 2012
										Allard et al., 1991, 1997

Volcano or area	Country or area	Type ^a	Sample ^b	Temperature [°C]			$\delta^{13}\text{C}(\text{CO}_2)$ [‰]			Reference
				Avg.	Min.	Max.	Avg.	Min.	Max.	
Etna	Italy	A	F	—	—	—	-1.8	-4.0	2.3	Allard et al., 1991, 1997; Martelli et al., 2008; Liotta et al., 2010; Chiodini et al., 2011; Paonita et al., 2012; Rizzo et al., 2014, 2015
Larderello	Italy	A	F	98	95	101	-3.1	-3.7	-2.5	Tassi et al., 2012
Manziana	Italy	A	F	24	12	38	-1.6	-4.1	0.5	Rogie et al., 2000; Tassi et al., 2012
Panarea Island	Italy	A	B	82	46	130	-1.2	-1.5	-0.9	Tassi et al., 2012
Solfatara of Pozzuoli	Italy	A	F	163	162	163	-1.7	-2.3	-0.9	Castrillo et al., 2004; Chiodini et al., 2011; Tassi et al., 2012
Stromboli	Italy	A	F	86.6	59.0	98.0	-0.3	-2.5	2.1	Carapezza and Federico, 2000; Finizola et al., 2003; Rizzo et al., 2009
Vesuvio	Italy	A	F	93	92	93	0.6	0.5	0.7	Tassi et al., 2012
Vulcano Island	Italy	A	F	337	40	670	-1.6	-3.4	0.7	Baubron et al., 1990; Capasso et al., 1997; Chiodini et al., 2011
Vulcano Island	Italy	A	G, S	76	58	101	-1.8	-3.2	-0.4	Baubron et al., 1990
Hakone	Japan	A	F	98	96	101	-3.1	-3.7	-2.5	Sano and Williams, 1996
Izu-Oshima	Japan	A	G	—	—	—	-1.7	-3.0	-1.2	Sano et al., 1995
Kirishima	Japan	A	B	58	30	85	-5.6	-5.6	-5.5	Sato et al., 1999
Kirishima	Japan	A	F	99	94	110	-5.4	-7.3	-3.9	Sano and Marty, 1995; Sato et al., 1999
Komagatake	Japan	A	B	75	—	—	-5.3	—	—	Ono et al., 1993
Kuju	Japan	A	F	278	120	351	-8.1	-8.9	-7.8	Sakai and Matsubaya, 1977; Saito et al., 2002
Kusatsu-Shirane	Japan	A	B	62	50	77	-1.8	-3.8	5.6	Sano et al., 1994
Kusatsu-Shirane	Japan	A	F	69	23	102	-3.0	-3.3	-2.8	Sano et al., 1994
Kussharo	Japan	A	B	44	—	—	-18.8	—	—	Ono et al., 1993
Maruyama	Japan	A	B	60	—	—	-15.5	—	—	Ono et al., 1993
Meakan	Japan	A	B	55	—	—	-7.9	—	—	Rouilleau et al., 2015
Meakan	Japan	A	F	167	94.5	240	-9.1	-9.8	-8.5	Rouilleau et al., 2015
Niseko	Japan	A	B	68	—	—	-5.9	—	—	Ono et al., 1993
Iwojima	Japan	A	B	100	99	100	0.2	-0.7	1.9	Notsu et al., 2005
Iwojima	Japan	A	F	99	91	106	1.2	-1.5	4.0	Sumino et al., 2004; Notsu et al., 2005
Ontake	Japan	A	B	22.1	12.3	41.0	-6.7	-9.7	-3.9	Ono et al., 1993; Sano et al., 1998;
Sakurajima	Japan	A	B	20	—	—	-13.7	—	—	Takahata et al., 2003; Kagoshima et al., 2016
Satsuma-Iwojima	Japan	A	F	665	101	860	-4.1	-5.5	-2.6	Rouilleau et al., 2013
Taisetsu	Japan	A	B	60	—	—	-8.9	—	—	Sakai and Matsubaya, 1977; Saito et al., 2002; Sato et al., 2002; Shimoike et al., 2002
										Ono et al., 1993

Volcano or area	Country or area	Type ^a	Sample ^b	Temperature [°C]			$\delta^{13}\text{C}(\text{CO}_2)$ [‰]			Reference
				Avg.	Min.	Max.	Avg.	Min.	Max.	
Tarumae	Japan	A	F	540	487	593	-6.4	-6.4	-6.3	Rouilleau et al., 2015
Tokachi	Japan	A	F	171	97	245	-5.3	-5.3	-5.2	Rouilleau et al., 2015
Unzen	Japan	A	B	59	23	100	-6.1	-9.6	-4.7	Kita et al., 1993; Ohsawa et al., 2002
Unzen	Japan	A	F	346	61.3	818	-6.0	-11.5	-4.1	Kita et al., 1993; Sano and Williams, 1996; Ohsawa et al., 2002; Ohba et al., 2008; Shinohara et al., 2008
Usu	Japan	A	F	568	—	—	-4.4	-4.7	-4.1	Allard, 1981
Kudryavy (Moyorodake)	Japan, Russia	A	F	540	160	920	-6.1	-7.6	-4.5	Taran et al., 1995; Fischer et al., 1998
Peléé	Martinique	A	B	20.5	—	—	-6.6	—	—	van Soest et al., 1998
Ceboruco	México	A	F	83	—	—	-4.1	—	—	Taran et al., 2002b
Colima	México	A	B	32	—	—	-4.9	—	—	Taran et al., 2002a Sano and Williams, 1996; Taran et al., 2002a
Colima	México	A	F	642	340	840	-6.3	-7.1	-5.2	1996; Taran et al., 2002a
El Chichón	México	A	B	43	26	76	-3.3	-5.5	-1.9	Mazot et al., 2011
El Chichón	México	A	F	98	97	98	-4.9	-8.1	-2.5	Mazot et al., 2011
Popocatépetl	México	A	B	—	—	—	-9.2	-9.9	-8.5	Inguaggiato et al., 2005
Popocatépetl	México	A	F	—	—	—	-6.5	—	—	Varley and Armienta, 2001
Sierra la Primavera	México	A	F	260	—	—	-3.9	—	—	Taran et al., 2002b
Soufrière Hills	Montserrat	A	B	—	—	—	0.3	0.0	0.5	Pedroni et al., 1999
Soufrière Hills	Montserrat	A	F	89.3	52.3	113.7	-3.2	-3.8	-2.4	van Soest et al., 1998
Ketetahi	New Zealand	A	F	106	95	136	-7.3	-8.2	-6.5	Giggenbach, 1995
Ngauruhoe	New Zealand	A	F	435	349	520	-10.4	-11.2	-9.5	Giggenbach, 1995
Raoul Island	New Zealand	A	F	99	—	—	-0.6	—	—	Giggenbach, 1995
Whale Island	New Zealand	A	B, S	99	—	—	-6.3	-7.1	-5.5	Giggenbach, 1995
White Island	New Zealand	A	B	99	—	—	-4.2	—	—	Giggenbach, 1995
White Island	New Zealand	A	F	334	104	665	-2.6	-4.2	-1.7	Giggenbach, 1990; Giggenbach, 1995 Sano and Williams, 1996; Salazar et al., 2001; Shaw et al., 2003
Cerro Negro	Nicaragua	A	F	286	97.7	386	-2.6	-3.2	-1.8	2001; Shaw et al., 2003
Masaya	Nicaragua	A	B	71.0	70.3	71.4	-2.4	-2.5	-2.1	Shaw et al., 2003
Masaya	Nicaragua	A	F	72.5	—	—	-1.5	—	—	Shaw et al., 2003
Mombacho	Nicaragua	A	F	110.4	—	—	-3.4	-3.6	-3.1	Shaw et al., 2003
Mombacho	Nicaragua	A	M	98	—	—	-2.7	—	—	Shaw et al., 2003
Momotombo	Nicaragua	A	F	679	490	748	-2.8	-3.1	-2.6	Allard, 1980a; Shaw et al., 2003
Momotombo	Nicaragua	A	G	300	—	—	-1.7	-2.6	-1.1	Shaw et al., 2003
San Cristóbal	Nicaragua	A	F	95.6	—	—	-3.0	-3.0	-2.9	Shaw et al., 2003
Telica	Nicaragua	A	B	78.5	—	—	-3.2	-3.3	-3.1	Shaw et al., 2003
Rabaul	Papua New Guinea	A	F	99	99	99	-2.7	-2.8	-2.6	Sano and Williams, 1996
Avachinsky	Russia	A	F	287	101	473	-5.7	-6.1	-5.2	Taran et al., 1997
Ebeko	Russia	A	F	107	96	120	-10.4	-11.6	-9.6	Taran et al., 1992
Kizimen	Russia	A	F	240	—	—	-14.4	—	—	Taran et al., 1992
Klyuchevskoy	Russia	A	F	1070	—	—	-11.6	—	—	Taran et al., 1991
Koryaksky	Russia	A	F	214	213	215	-12.0	-12.2	-11.8	Taran et al., 1992, 1997
Kuntomintar	Russia	A	F	162	—	—	-10.6	—	—	Taran et al., 1992

Volcano or area	Country or area	Type ^a	Sample ^b	Temperature [°C]			$\delta^{13}\text{C}(\text{CO}_2)$ [‰]			Reference
				Avg.	Min.	Max.	Avg.	Min.	Max.	
Mutnovsky	Russia	A	F	295	272	360	-9.9	-11.8	-8.5	Taran et al., 1992
Rasshua	Russia	A	F	155	—	—	-8.6	—	—	Taran et al., 1992
Shiveluch	Russia	A	F	216	—	—	-9.9	—	—	Taran et al., 1992
Nevis Peak	Saint Kitts and Nevis	A	B	—	—	—	-8.4	—	—	Pedroni et al., 1999
Nevis Peak	Saint Kitts and Nevis	A	F	91.9	82.7	101.0	-3.5	-3.9	-3.0	van Soest et al., 1998
Qualibou	Saint Lucia	A	B	—	—	—	-9.6	-10.2	-8.9	Pedroni et al., 1999
Qualibou	Saint Lucia	A	F	65.6	51.5	77.7	-6.3	-6.8	-5.8	1998; Pedroni et al., 1999
Soufrière St. Vincent	Saint Vincent and the Grenadines	A	F	88.0	—	—	-6.2	-6.6	-6.0	van Soest et al., 1998; Pedroni et al., 1999
Tatun	Taiwan	A	F	—	—	—	-4.2	-6.3	-3.0	Lan et al., 2007; Wen et al., 2016
Kanaga	USA	A	F	—	—	—	-4.4	—	—	Fischer and Lopez, 2016
Lassen	USA	A	B	8	—	—	-9.1	—	—	Rose and Davisson, 1996
Ukinrek Marrs	USA	A	B	—	—	—	-6.0	-6.4	-5.6	Evans et al., 2009
Zunil	Guatemala	G	F	94.0	—	—	-2.9	—	—	Sano and Williams, 1996
Adriatic	Italy	G	B	24	16	43	1.0	-18.3	26.6	Tassi et al., 2012
Apennine	Italy	G	B	19	15	35	17.2	-29.2	35.6	Tassi et al., 2012
Torre Alfina	Italy	G	G	—	—	—	1.3	—	—	Carapezza et al., 2015
Tyrrhenian	Italy	G	B	22	10	57	-2.0	-9.2	3.7	Tassi et al., 2012
Val D'Agri	Italy	G	B	17	15	20	-13.1	-16.4	-7.6	Tassi et al., 2012
Arima	Japan	G	B	25	—	—	-6.8	—	—	Ono et al., 1993
Kamasaki	Japan	G	B	40	—	—	-8.2	—	—	Ono et al., 1993
Kitayuzawa	Japan	G	B	89	—	—	-19.5	—	—	Ono et al., 1993
Misasa	Japan	G	B	49	—	—	-12.1	—	—	Ono et al., 1993
Nariai	Japan	G	B	24	—	—	-4.1	—	—	Ono et al., 1993
Nigorikawa	Japan	G	B	57	—	—	-4.8	—	—	Ono et al., 1993
Otoshibe	Japan	G	B	95	—	—	-5.3	—	—	Ono et al., 1993
Raiden	Japan	G	B	47	—	—	-27.4	—	—	Ono et al., 1993
Takarazuka	Japan	G	B	30	—	—	-9.4	—	—	Ono et al., 1993
Tateshina	Japan	G	B	24	—	—	-2.3	—	—	Ono et al., 1993
Tonbara	Japan	G	B	15	—	—	-10.7	—	—	Ono et al., 1993
Uminokuchi	Japan	G	B	33	—	—	-12.9	—	—	Ono et al., 1993
Yunokawa	Japan	G	B	60	—	—	-5.1	—	—	Ono et al., 1993
Atiamuri	New Zealand	G	F	670	—	—	-9.0	—	—	Giggenbach, 1995
Bay of Plenty	New Zealand	G	F	62	46	98	-5.2	-11.6	-1.2	Giggenbach, 1995
Broadlands	New Zealand	G	G, M	1060	98	1410	-7.6	-10.8	-6.9	Lyon and Hulston, 1984; Giggenbach, 1995
Horohoro	New Zealand	G	F	54	—	—	-6.1	—	—	Giggenbach, 1995
Kawerau	New Zealand	G	G	920	250	1210	-6.9	-8.0	-5.9	Giggenbach, 1995, 1997
Mangakino	New Zealand	G	F	750	—	—	-7.0	—	—	Giggenbach, 1995
Mokai	New Zealand	G	F	99	—	—	-5.3	—	—	Giggenbach, 1995
Mokai	New Zealand	G	G	1184	320	1760	-4.8	-5.7	-4.0	Giggenbach, 1995, 1997
Ngatamariki	New Zealand	G	G, M	257	28.9	1260	-6.8	-7.0	-6.6	Giggenbach, 1995, 1997; Hanson et al., 2014

Volcano or area	Country or area	Type ^a	Sample ^b	Temperature [°C]			$\delta^{13}\text{C}(\text{CO}_2)$ [‰]			Reference
				Avg.	Min.	Max.	Avg.	Min.	Max.	
Ngawha	New Zealand	G	G, M	120	17	237	-8.7	-9.7	-7.9	Lyon and Hulston, 1984; Giggenbach, 1997
Ohaaki	New Zealand	G	G	300	—	—	-7.8	—	—	Giggenbach, 1997
Orakei Korako	New Zealand	G	F	97	94	99	-3.1	-4.0	-2.2	Giggenbach, 1995
Orakei Korako	New Zealand	G	M	99	—	—	-2.5	—	—	Giggenbach, 1995
Reporoa	New Zealand	G	B, M	81	50	97	-8.3	-10.6	-7.0	Giggenbach, 1995
Rotokawa	New Zealand	G	F	100	—	—	-7.8	—	—	Giggenbach, 1995
Rotokawa	New Zealand	G	G	1168	330	1500	-7.8	-7.9	-7.5	Giggenbach, 1995, 1997
Rotorua	New Zealand	G	B, G	144	57	230	-5.0	-5.3	-4.6	Giggenbach, 1995, 1997
Rotorua	New Zealand	G	F	95	92	98	-5.9	-7.0	-4.9	Giggenbach, 1995
Te Kopia	New Zealand	G	F	99	—	—	-4.7	—	—	Giggenbach, 1995
Te Kopia	New Zealand	G	M	98	—	—	-3.0	—	—	Giggenbach, 1995
Tikitere	New Zealand	G	F	86	74	100	-7.1	-7.9	-6.5	Lyon and Hulston, 1984; Giggenbach, 1995
Tokaanu	New Zealand	G	F	59	19	99	-4.6	—	—	Giggenbach, 1995
Tokaanu	New Zealand	G	M	74	73	74	-7.8	-10.8	-4.8	Giggenbach, 1995
Waikite	New Zealand	G	B	—	—	—	-6.6	—	—	Giggenbach, 1995
Waikite	New Zealand	G	F	99	—	—	-7.6	—	—	Giggenbach, 1995
Waimangu	New Zealand	G	F	97	91	99	-3.5	-3.6	-3.1	Giggenbach, 1995
Waiotapu	New Zealand	G	B	76	—	—	-8.3	—	—	Giggenbach, 1995
Waiotapu	New Zealand	G	F	88	56	100	-6.9	-7.4	-6.1	Giggenbach, 1995
Wairakei	New Zealand	G	F	132	98	192	-5.1	-6.9	-3.7	Giggenbach, 1995
Wairakei	New Zealand	G	G	995	260	1350	-4.9	-6.2	-3.2	Lyon and Hulston, 1984; Giggenbach, 1995, 1997
Lake Antoine	Grenada	I	B	32.3	32.0	32.5	-6.3	-6.6	-6.0	van Soest et al., 1998; Pedroni et al., 1999
Albani Hills	Italy	I	F	—	—	—	-1.4	-3.5	0.9	Chiodini and Frondini, 2001
Latera	Italy	I	F	24.0	15.0	31.6	1.5	0.9	2.0	Chiodini et al., 2007a; Tassi et al., 2012
Vulture	Italy	I	B	—	—	—	-4.4	-6.2	-3.2	Caracausi et al., 2015
Hakkoda	Japan	I	F	—	—	—	-3.4	-3.8	-2.7	Hernández Perez et al., 2003
Lamentin	Martinique	I	B, M	—	—	—	-7.1	-7.8	-6.2	Pedroni et al., 1999
Morne Jacob	Martinique	I	G	—	—	—	-6.4	-6.4	-6.3	Pedroni et al., 1999
Pitons du Carbet	Martinique	I	B	—	—	—	-8.9	-9.4	-8.7	Pedroni et al., 1999
Acoculco caldera	México	I	B	19.7	12.2	25.4	-3.7	-4.6	-2.9	Peiffer et al., 2014
Unknown	Saint Lucia	I	B	—	—	—	-6.8	-6.9	-6.7	Pedroni et al., 1999
Grand Bonhomme	Saint Vincent and the Grenadines	I	B	—	—	—	-2.2	—	—	Pedroni et al., 1999

^aA: Active volcano; G: Geothermal field; I: Inactive volcano

^bB: Bubbling gas; F: Fumarole; G: Gas from geothermal well; M: Mofette; S: Submarine fumarole

Alphabetical order in Country or area

— not available

